Catalytic Combustion of Methane with Nanostructured Barium Hexaaluminate-Based Materials

by

Juan Andrey Zarur Jury

M.S. Chemical Engineering Practice
Massachusetts Institute of Technology, 1995

B. Sc. Chemical Engineering
Universidad Nacional Autonoma de México, 1992

Submitted to the Department of Chemical Engineering
in Partial Fulfillment of the Requirements for the Degree of

Doctor of Philosophy in Chemical Engineering

at the

MASSACHUSETTS INSTITUTE OF TECHNOLOGY

February 2000

Author:_____
Department of Chemical Engineering
October 27, 1999

Certified by:_____
Prof. Jackie Y. Ying
Associate Professor of Chemical Engineering
Thesis Supervisor

Accepted by:_____
Prof. Robert E. Cohen
St. Laurent Professor of Chemical Engineering
Chairman, Departmental Committee on Graduate Studies

Catalytic Combustion of Methane with Nanostructured Barium Hexaaluminate-based Materials

by

Juan Andrey Zarur Jury

M.S. Chemical Engineering Practice
Massachusetts Institute of Technology, 1995

B.S. Chemical Engineering
Universidad Nacional Autonoma de Mexico, 1993

Submitted to the Department of Chemical Engineering
On October 27, 1999 in Partial Fulfillment of the
Requirements for the Degree of Doctor of Philosophy in
Chemical Engineering

ABSTRACT

Catalytic combustion of methane has been widely studied as an alternative to gas-phase homogeneous combustion. It allows combustion to occur at high levels of excess air, leading to more complete reaction and reduced hydrocarbon emissions. It further enables combustion to proceed at lower temperatures, significantly reducing the NO_x production. Noble metal systems, such as platinum and palladium, have been studied as combustion catalysts. However, noble metal clusters tend to sinter or vaporize at the high combustion temperatures. Recently, complex oxides have been examined for methane combustion due to their enhanced thermal resistance. Barium hexaaluminate (BHA) was chosen for this research, since its unique crystalline structure has the potential to suppress grain growth at high temperatures. A novel reverse microemulsion-mediated sol-gel processing technique was developed to synthesize non-agglomerated BHA nanoparticles with high surface areas and thermal stability. The reverse microemulsion also provided a unique medium to achieve highly dispersed active species on BHA nanoparticles to enhance the catalytic performance for methane combustion.

Reverse microemulsions of water/iso-octane and water/cyclohexane were successfully stabilized with a non-ionic surfactant system consisting of polyethoxylated and linear alcohols. The water/iso-octane system was found to be ideal for the sol-gel mediated synthesis, since it required only a small amount of surfactants for stabilization. Quasi-elastic light scattering and small-angle neutron scattering showed that at low water contents, the reverse microemulsions consisted of slightly polydisperse discrete aqueous domains with a core-shell structure. Systems with higher water contents could be best described with a bicontinuous structure with intermixed water and oil domains. The water/iso-octane system was found to possess excellent stability under the conditions required for reverse microemulsion-mediated sol-gel processing of BHA materials.

The composition of the reverse microemulsion governed the morphology of the aqueous domains, which in turn determined the shape and aggregation of the BHA particles derived. Non-agglomerated nanospheres were recovered from reverse microemulsions with water volume fractions of 0.05-0.15. At higher water contents, percolation between aqueous domains in the system became significant, yielding BHA particles with filament-like morphologies. The water:alkoxide ratio in the sol-gel process determined the relative rates of hydrolysis and polycondensation reactions. At a relatively high water:alkoxide ratio of ≥100 times the stoichiometric value, the stability of the reverse microemulsion was preserved throughout the aging process. Well-defined, high surface area BHA nanoparticles were successfully recovered from the medium by freeze drying. Residual surfactants and volatiles were best removed by supercritical drying. The resulting materials were crystallized at a relatively low temperature of 1050°C due to their superb chemical homogeneity. Surface areas of >160 m^2/g and ultrafine grain sizes of ≤30 nm were retained by these BHA nanoparticles after calcination at 1300°C.

Active transition metal and rare earth oxides could be deposited with ultrahigh dispersion on BHA nanoparticles during their aging in the reverse microemulsion medium. BHA nanoparticles coated with MnO_2 and CeO_2 clusters showed light-off (defined as 10% conversion of an air stream containing 1 vol% CH_4) at remarkably low temperatures of ~400°C, rivaling noble metal systems. These novel materials sustained their activity for extended periods at temperatures in excess of 1000°C, demonstrating a thermal stability superior to other existing combustion catalysts.

The performance of BHA-based materials was evaluated in an atmospheric burner operated under realistic industrial conditions. Catalyst systems were washcoated onto monoliths of different compositions and microstructures. Nickel foams and fiber-reinforced honeycombs demonstrated excellent thermal shock resistance; the latter were preferred for high-temperature operations since they would give rise to negligible pressure drops. In our catalytic combustor design, nanocrystalline PdO/CeO_2-BHA was used as the low-temperature ignition catalyst to initiate the reaction by 250°C. A mid-temperature catalyst, such as MnO_2-BHA or CeO_2-BHA nanocomposite, was utilized to promote reaction in the range of 600-1000°C. A flame-supporting catalyst, consisting of pure nanostructured BHA was employed to stabilize the flame at temperatures up to 1300°C. Using this multi-stage catalyst design, flames of ultra-lean methane:oxygen ratios ($0.2 \leq \phi \leq 0.5$) were ignited and sustained for extended periods over multiple heating-cooling-restarting cycles. This system successfully eliminated NO_x production with no unburned hydrocarbon emissions in an effective catalytic methane combustion process.

Acknowledgments

First and foremost, I would like to thank Prof. Jackie Ying for her guidance, support and friendship. Her enthusiasm for my research and her loyalty were pivotal in my work. I would also like to thank the members of my thesis committee: Prof. Jack B. Howard, Prof. Kenneth A. Smith, and Prof. Jefferson W. Tester for their advice and constructive criticism over the course of this thesis. Additionally, I would like to acknowledge Prof. Janos M. Beer, Prof. William H. Green, Prof. Daniel Blankschtein, Prof. T. Alan Hatton, and Prof. Bernhardt Wuensch for helpful discussions.

In my five years as a member of the Nanostructured Materials Research Laboratory, I have had the opportunity to collaborate with very talented people. I would like to especially acknowledge my classmates Mark Fokema, Larry Panchula, Chen-Chi Wang and Michael Wong for their continuous support and friendship. Several undergraduate researchers contributed to the development of this thesis, including Anne Heibel, Henry Hwu, George Lin, Steve Lefkowitz, Beatrice Wang, and Neville Mehenti. Without their hard work, enthusiasm, and creativity, this work could not have been completed. I would also like to thank those graduate students who helped build the NMRL from the ground up, and got me started on the right track. They are Dr. Kenneth Bryden, Dr. Darren Castro, Dr. Doron Levin, and Dr. Lei Zhang. I would also like to acknowledge Justin McCue, Neeraj Sangar, Michael Lei, and John Lettow for their technical help in various projects. All the other members of the NMRL have contributed in one way or another to the development of this research, and for this, I thank them profoundly. They are Edward Ahn, Ruma Chakravorty, Patricia Cheung, Alice Choi, Dr. Deijian Huang, Esther Jeng, Yu-Ming Lin, Dr. Christian Mehnert, Suniti Moudgil, Duane Myers, Dr. Atsushi Nakahira, Reginald Rogers, Wolfgang Rupp, Mehul Shah, Yee San Su, Dr. Tao Sun, Jason Sweeney, Steven Weiss, and Dr. Jinsuo Xu.

The staff at M.I.T. is one of its greatest assets. I would like to thank Michael Frongillo for his guidance in electron microscopy. I would also like to acknowledge Linda Mousseau and Ellen Weene for taking care of the administrative tasks of the group, and Arline Benford for her support and friendship. I thank Janet Fischer and Elaine Aufiero for their help with the thesis preparation process. Financial support from Quantum Energy Technologies, the Packard Foundation, and ABB Alstom Power is appreciated.

I would like to thank my good friends, Gary Adamkiewicz, Mark Angelino, Alejandro Cano, Seth Rodgers and Rajesh Venkataramani for their unconditional support and loyalty.

My parents, Sonia and Antonio, and my brother Jorge, have always supported me and showed me their unending care. Thank you very much. My deepest gratitude goes to my wife Christianne. Her love, patience and care were the motivation and inspiration that allowed me to finish this journey. Thank you God for allowing me to take one more step in life.

This thesis is dedicated to my grandparents, Maria, Alfredo, and Yamel, and in loving memory of my grandfather Neif.

Table of Contents

List of Figures

List of Tables

List of Symbols

Chapter 2

Q = Neutron scattering vector
ϕ_w = Water volume fraction
ϕ_o = Oil volume fraction
ϕ_s = Surfactant volume fraction
ϕ_a = Alcohol volume fraction
d_h = Hydrodynamic diameter
k_B = Boltzmann's constant
T = Temperature (K)
η = Absolute viscosity (Poise)
Γ = Decay constant of a correlation function
λ Wavelength of incident radiation (Å)
θ = Scattering angle
D_o = Diffusion coefficient at infinite dilution
D_{app} = Diffusion coefficient
ϕ_H = Hydrodynamic volume fraction
ρ = Number density
R_H = Hydrodynamic radius
I_o = Absolute scattering intensity (cm^{-1})
q = Scattering length ($Å^{-1}$)
ξ = Correlation length (nm)
d = Pseudo-periodic repeat distance (nm)

Chapter 3

E_a = Activation energy (kJ/mol)
T_m = Temperature of maximum deflection (K)
R = Universal gas constant
φ = Ramping rate (°C/minute)

Chapter 4

a = Unit cell lattice parameter (Å)
c = Unit cell lattice parameter (Å)

Chapter 5

ϕ = Equivalent molar ratio

Chapter 1. Background and Research Motivation

1.1 Combustion of Hydrocarbons

Combustion of carbon-containing fuels is used extensively today in industry as a means of generating electric energy. Roughly 70% of the total electric power generated in the United States comes from the combustion of coal (54.9%), natural gas (9.4%), and other hydrocarbons (3.9%) [1]. Environmental regulations, recently put into effect both in the United States and the international community, significantly restrict the output of hazardous products from the combustion processes. These include greenhouse gases, acid rain-causing compounds, and ozone-depleting agents [2-4]. Furthermore, as a result of the United Nations Framework Convention on Climate Change held in Kyoto in December 1997, the majority of the industrialized nations agreed to a reduction of at least 5% in the overall emissions of greenhouse gases for the next 10 years [5]. Greenhouse gases, as defined by this Convention, include carbon dioxide (CO_2), methane (CH_4), nitrous oxide (N_2O), hydrofluorocarbons (HFCs), perfluorocarbons (PFCs) and sulfur hexafluoride (SF_6).

Combustion of methane is an important alternative to combustion of coal or long-chain hydrocarbons in power generation and other processes, since it has the potential to reduce the emission of greenhouse gases. Methane generates twice the amount of energy per unit mass of CO_2 emitted than coal due to its high hydrogen-to-carbon ratio (Figure 1.1). However, methane requires a higher flame temperature for stable combustion than other hydrocarbons, due in part to the absence of carbon-carbon bonds in the molecule, which makes it relatively unreactive.

The elevated temperatures required for methane combustion (>1400°C) can cause significant production of nitrogen oxide species (NO_x). Formation of NO_x under these conditions occurs through two different mechanisms [6]. The first is direct oxidation of the nitrogen in air (thermal NO_x) [7]. The second mechanism involves reaction of methyl radicals with nitrogen, leading to HCN species, which can be further oxidized to NO_x (prompt NO_x) [8]. Exposure to high levels of NO_x may have immediate impact on human health, such as cyanosis and pulmonary edema. Prolonged exposure to NO_x above the natural ambient levels may lead to bronchitis, pneumonia and alterations to the

immune system [9]. Additionally, NO_x contributes to the formation of smog by reacting with unburned hydrocarbons and volatile organic compounds to form ozone, and also leads to acid precipitation [10].

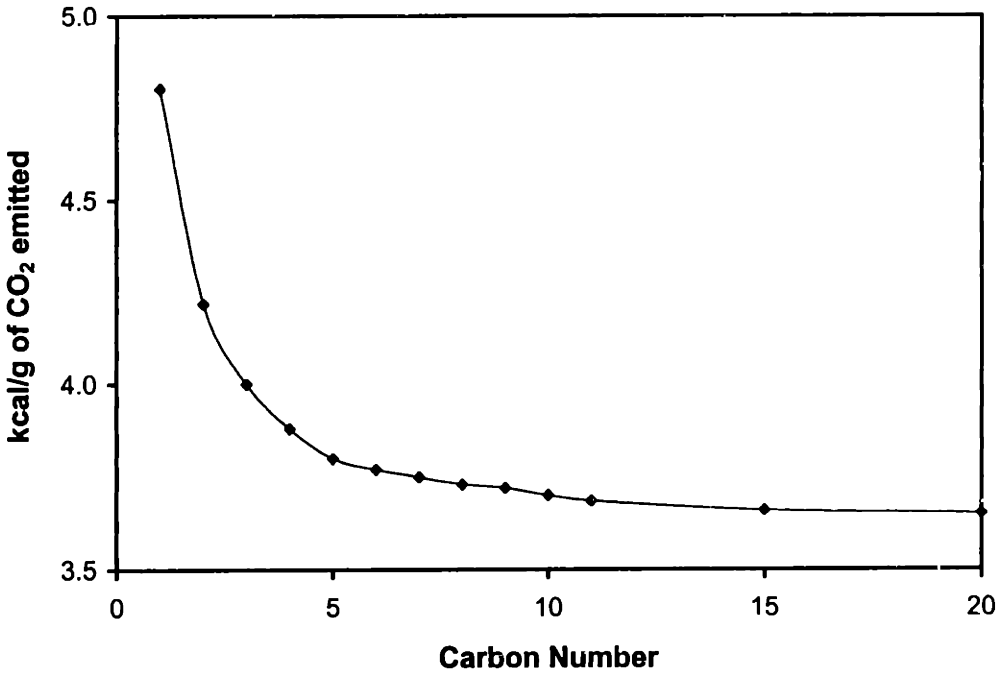

Figure 1.1. Calculated energy output per gram of CO_2 emitted in the combustion of various hydrocarbons.

In addition to NO_x emissions, a substantial amount of unburned or partially oxidized hydrocarbons may be emitted during the initial start-up stages of a methane or natural gas combustor. These compounds can contribute to the formation of smog and have significant greenhouse effects [5].

1.2 Catalytic Combustion

Catalytic combustion of methane and natural gas has been studied as an alternative to gas-phase homogeneous combustion [11]. The use of a suitable catalyst can lead to oxidation of the fuel without a flame, and/or reduce the temperature at which a stable flame is produced and maintained [12], thus minimizing the production of NO_x. The use of a catalyst also allows for combustion to occur at high levels of excess air, leading to a more complete combustion and reduced hydrocarbon emissions [12]. In catalytic combustion, radicals that promote the gas-phase homogeneous combustion are produced on the catalyst surface and subsequently desorbed. These radicals are

presumed to stabilize the flame at temperatures lower than that of a homogeneous adiabatic flame [13]. A reactor that uses this type of catalyst system is known as a catalytically stabilized thermal combustor (CSTC). The volumetric heat output of a CSTC, defined as the heat produced per unit volume of the combustion chamber, is comparable to that of a conventional homogeneous flame combustor [14].

1.3 Design Requirements for Combustion Catalysts

Prasad *et al.* [15] have examined the requirements of combustion catalysts; an ideal combustion catalyst should possess the following properties:

1. Stable ignition of the combustion mixture should occur at the lowest possible temperature and the leanest fuel-to-air ratio.
2. The catalyst should be active at low temperatures to maintain complete combustion at the lowest inlet temperatures.
3. The catalyst and support should have high thermal and hydrothermal resistance and stability for prolonged operations at temperatures above 1300°C.
4. The catalyst support should maintain a high surface area, a low pressure drop and a high thermal shock resistance.

Overall, the proposed catalytic system needs to accommodate two types of reactions. The first reaction is the flameless combustion of hydrocarbon species on the catalyst surface; typically, this reaction occurs at temperatures below 800°C [14]. As the temperature is increased to above 800°C, gas-phase homogeneous combustion becomes the dominant reaction [13,16]. The role of the catalyst under these conditions is to provide the gas-phase radicals necessary to stabilize the flame.

1.4 Catalyst Selection for Combustion

1.4.1 Noble Metal Systems

Traditionally, noble metals such as platinum and palladium have been used as combustion catalysts. These materials have been employed extensively in other oxidation reactions, therefore, their application in catalytic combustion followed naturally. Noble metal catalysts have been studied in a variety of configurations, ranging from simple films or heated wires [17], to clusters supported on high surface area washcoats [18,19].

Films and wire meshes have very low specific surface areas, so the cost of a functional catalyst may be prohibitively high. Noble metal clusters dispersed on high surface area oxide washcoats tend to sinter or vaporize at temperatures above 750°C, so they cannot be employed in the presence of a flame. Nevertheless, they may still be used in catalytic combustion as ignition catalysts. Their role would be to initiate oxidation reactions at the lowest possible temperature, effectively heating the reaction stream to allow light-off of the more thermally robust but less active materials used as the flame-supporting catalysts. The latter stabilize the flame, and shield the noble metal systems from high flame temperatures. Highly dispersed platinum and palladium oxide supported on high surface area γ-Al_2O_3 have shown light-off (defined as the temperature at which 10% CH_4 conversion is observed) of an air stream containing 1 vol% CH_4 flowing at 60,000 h^{-1} at temperatures as low as 400°C and 250°C, respectively [20].

1.4.2 Metal Oxide Catalysts

Transition metal oxides such as Co_3O_4, Mn_2O_3, TiO_2, Fe_2O_3 and NiO [15,21-26], and base metal oxides such as magnesium and strontium oxides [27-29], have been studied as alternatives for noble metal systems for catalytic combustion [16]. The main advantage of metal oxide catalysts is their higher thermal stability compared to noble metal systems. Additionally, metal oxides have lower raw material costs than noble metals. The main disadvantages of metal oxides are their lower specific activity and higher ignition temperature. Cobalt and manganese oxides have shown the highest activity for methane combustion of the simple transition metal oxides, while magnesium oxide has the highest activity of the base metal oxides. Light-off of an air stream containing 1 vol% CH_4 was observed at 450-470°C for Co_3O_4 and Mn_3O_4, and at ~600°C for MgO [16].

Although transition metal oxides exhibit better thermal stability than noble metal systems, they cannot be operated at flame temperatures in excess of 1300°C due to the rapid grain growth and loss of surface area that would occur under those conditions. Conversion of Co_3O_4 to CoO, which has negligible specific activity for methane combustion, occurs at 900-950°C; while Mn_3O_4 sinters rapidly, losing all active surface area above 800°C [15].

In contrast, nanocrystalline MgO of enhanced thermal resistance can be synthesized through thermal evaporation and gas-phase oxidation of Mg [27]. The resulting nanostructured particles can retain 10-15 m^2/g even at 1400°C. However, these materials have low specific activity, and their synthesis procedure involves high capital and processing costs.

1.4.3 Complex Oxide Systems

More recently, complex oxides such as barium and lanthanum hexaaluminates, perovskites, and aluminosilicates have been evaluated as candidates for support washcoats, or active washcoats and catalytic particles [16]. The complex crystal structure of some of these oxides allows them to sustain relatively high surface areas at elevated temperatures due to the highly anisotropic crystal properties that would suppress grain growth. Additionally, the composition of hexaaluminates, perovskites and alumino-silicates can be modified to accommodate a variety of structural and surface dopants that may lead to enhanced catalytic properties.

The barium hexaaluminate (BHA) system is of special interest for catalytic combustion applications. This material has been demonstrated to maintain relatively high surface areas (~10-15 m^2/g) after calcination at 1600 °C [30]. The excellent thermal stability is believed to arise from the complex hexagonal structure of barium hexaaluminate (Figure 1.2). The structure includes two intermixed unit cells commonly known as barium hexaaluminate Phase I [31] and Phase II [32], which correspond to a barium-deficient and a barium-rich system, respectively. Both phases belong to a $P6_3/mmc$ crystallographic group, whereby spinnel-like structures are arranged along a screw-axis in the *c* direction. This unusual arrangement results in flat hexagonal crystallites with highly suppressed growth along the *c*-axis [33]. Upon crystallization, BHA particles appear to be stable and do not undergo significant grain growth. However, materials produced by conventional synthesis techniques require extended calcination at temperatures as high as 1300°C to achieve crystallization [34]. Such heat treatment typically causes significant pore collapse and reduction of surface area to 10-15 m^2/g.

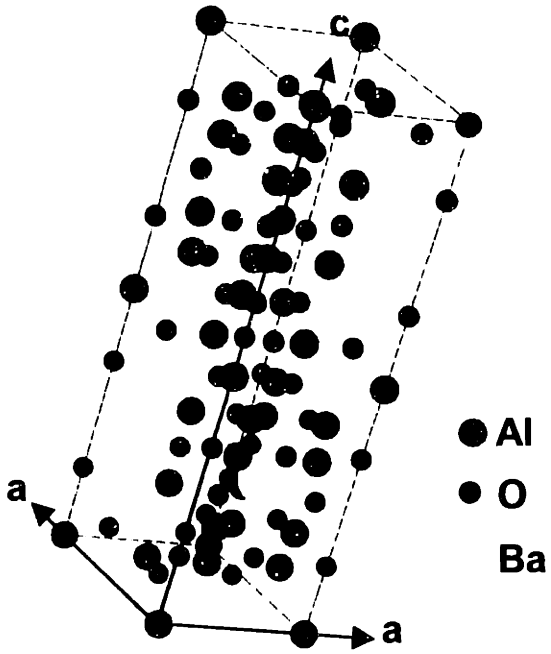

Figure 1.2. Idealized structure of barium hexaaluminate unit cell projected along the (111) reflection.

The low-temperature catalytic activity of BHA can be increased through the introduction of transition metal dopants, such as Mn, La and Ni [35]. Pure and doped BHA materials have been investigated as potential catalyst systems, showing excellent thermal resistance and high catalytic activity at temperatures above 550°C [36]. These materials have also been investigated as high-temperature supports for noble metal [19] and metal oxide [37] systems.

1.5 Research Motivation

Currently, there are no catalyst systems that can be employed in industrial catalytic combustion applications. Catalysts with high specific activity that are able to light-off at low temperatures are not stable in continued operation at flame conditions. On the other hand, stable catalysts that can withstand long-term operation at high temperatures and hydrothermal conditions are not active enough to light-off at temperatures that would make them economically viable. We have proposed to use nanostructure processing to synthesize novel catalyst systems that would allow for light-off at temperatures below 400°C, and sustain continuous stable operation at ultra-lean

flame conditions for extended periods. Specifically, we have concentrated our efforts on the synthesis of pure and modified nanostructured complex oxides, such as BHA.

Nanostructured materials offer unique size-dependent properties [38-40], a large surface-to-volume ratio [41-43], and unusual chemical/electronic synergistic effects from ultrahigh component dispersion [44,45]. Our strategy was to develop a synthesis approach that would generate non-agglomerated nanostructured materials with controlled particle morphology to attain superb surface area and sintering resistance. We further sought to achieve molecular-level chemical homogeneity in complex oxides, so as to induce crystallization of the desired crystalline phase at lower temperatures to effectively suppress grain growth. Finally, to increase the catalytic activity (especially at low temperatures), we would utilize nanocomposite catalyst design to establish synergistic effects between the noble metals, rare earth oxides or transition metal oxides, and the complex oxide supports.

In addition to materials processing, other issues need to be addressed to design an effective catalytic combustion system. First, it is critical to understand the role of catalyst in the stabilization of flame fronts. Secondly, it is important to elucidate the mechanistic differences for the activation of methane over metal oxide surfaces versus traditional noble metal catalysts. Finally, working catalyst prototypes, applicable to industrial CSTC design, need to be constructed and tested under realistic operating conditions.

In this thesis, a reverse microemulsion-mediated synthesis has been developed to generate nanostructured materials with ultrahigh surface areas and enhanced catalytic properties and stability. Specifically, BHA systems modified with active noble metals, rare earth oxides and transition metal oxides have been derived for catalytic combustion. The catalyst composition was optimized based on light-off temperature and hydrothermal stability. Kinetic analysis of the selected catalysts has been conducted under various methane concentrations and temperatures to elucidate the mechanistic differences between metal oxide and noble metal systems. Lastly, a working prototype of a CSTC has been designed and constructed to test the optimized catalyst systems under industrial operating conditions for methane combustion.

1.6 References

[1] "Statistical Yearbook." Edison Electric Institute, 1994.

[2] "Clean Air Act Amendments (CAAA), Title I." Environmental Protection Agency, 1990.

[3] "Clean Air Act Amendments (CAAA), Title IV." Environmental Protection Agency, 1990.

[4] "Global Warming Coalition." 1993.

[5] "Kyoto Protocol to the United Nations Framework Convention on Climate Change." United Nations Organization, 1997.

[6] K. C. Taylor, *Catal. Rev.-Sci. Eng.* **35**, 457 (1993).

[7] C. P. Fenimore, *Combust. Flame* **26**, 249 (1976).

[8] Y. B. Zeldovich, *Acta Physicochem. URSS* **21**, 577 (1946).

[9] J. N. Armor, *Appl. Catal. B: Env.* **1**, 221 (1992).

[10] C. J. Pereira, M. D. Amiridis, *in* "Reduction of Nitrogen Oxide Emissions," (U. S. Ozkan, S. K. Agarwal, G. Marcelin, Eds.), vol. 587, p. 1. American Chemical Society, Washington, D.C., 1995.

[11] J. E. Germain, "Catalytic Conversion of Hydrocarbons." Academic Press, London, 1969.

[12] A. Linan, F. A. Williams, "Fundamental Aspects of Combustion." Engineering Science Series, Oxford Press, New York, 1993.

[13] J. H. Lunsford, *Langmuir* **5**, 12 (1989).

[14] L. D. Pfefferle, W. C. Pfefferle, *Catal. Rev.-Sci. Eng.* **29**, 219 (1987).

[15] R. Prasad, L. A. Kennedy, E. Ruckenstein, *Catal. Rev.-Sci. Eng.* **26**, 1 (1984).

[16] M. F. M. Zwinkels, S. G. Jaras, P. G. Menon, *Catal. Rev.-Sci. Eng.* **35**, 319 (1993).

[17] D. A. Goetsch, L. D. Schmidt, *Science* **271**, 1560 (1996).

[18] A. Schwartz, L. L. Holbrook, H. Wise, *J. Catal.* **21**, 190 (1971).

[19] J. G. McCarty, *Catal. Today* **26**, 283 (1995).

[20] J. T. McCue, J. Y. Ying, Unpublished Results, M.I.T., 1999.

[21] K. C. Stein, *Ind. Eng. Chem.* **52**, 671 (1960).

[22] O. V. Krylov, "Catalysis by Nonmetals." Academic Press, New York, 1970.

[23] J. G. McCarty, H. Wise, *Catal. Today* **8**, 231 (1990).

[24] Y. Morooka, A. Ozaki, *J. Catal.* **5**, 116 (1966).

[25] Y. Morooka, Y. Morikawa, A. Ozaki, *J. Catal.* **7**, 23 (1967).

[26] M. A. Quinan, H. Wise, J. G. McCarty, "Basic Research on Natural Gas Combustion Phenomena - Catalytic Combustion," GRI-89/0141. SRI International, Pittsburgh, PA, 1989.

[27] I. Matsuura, Y. Hashimoto, O. Takayasu, K. Nitta, Y. Yoshida, *Appl. Catal.* **74**, 273 (1991).

[28] M. Berg, S. Jaras, *Appl. Catal. A: Gen.* **114**, 227 (1994).

[29] M. Berg, S. Jaras, *Catal. Today* **26**, 223 (1995).

[30] H. Arai, M. Machida, *Appl. Catal. A: Gen.* **138**, 161 (1996).

[31] N. Iyi, Z. Inoue, S. Takekawa, S. Kimura, *J. Sol. St. Chem.* **52**, 66 (1984).

[32] N. Iyi, Z. Inoue, S. Takekawa, S. Kimura, *J. Sol. St. Chem.* **60**, 41 (1985).

[33] J.-G. Park, A. N. Cormack, *J. Sol. St. Chem.* **121**, 278 (1996).

[34] Y. Mizushima, M. Hori, *J. Mater. Res.* **9**, 2272 (1994).

[35] M. Machida, K. Eguchi, H. Arai, *J. Catal.* **120**, 377 (1989).

[36] M. Machida, K. Eguchi, H. Arai, *Chem. Lett.*, 267 (1987).

[37] M. Machida, A. Sato, T. Kijima, H. Inoue, K. Eguchi, H. Arai, *Catal. Today* **26**, 239 (1995).

[38] R. W. Cahn, *Nature* **348**, 389 (1990).

[39] M. Nirmal, *et al.*, *Nature* **383**, 802 (1996).

[40] A. P. Alivisatos, *Science* **271**, 933 (1996).

[41] J. Karch, R. Birringer, H. Gleiter, *Nature* **330**, 556 (1987).

[42] H. Gleiter, *Progr. Mater. Sci.* **33**, 223 (1989).

[43] R. W. Siegel, *Ann. Rev. Mater. Sci.* **21**, 559 (1991).

[44] J. Y. Ying, A. Tschöpe, *Chem. Eng. J.* **2**, 225 (1996).

[45] J. Y. Ying, A. Tschöpe, D. Levin, *Nanostr. Mater.* **6**, 237 (1995).

Chapter 2. Synthesis and Structure of Reverse Microemulsions

2.1 Introduction

Microemulsions are thermodynamically stable systems consisting of a hydrophilic phase and a hydrophobic phase, stabilized with the use of surfactants. Regular microemulsions consist of nanometer-sized hydrocarbon domains (termed micelles) surrounded by amphiphilic molecules, stabilized in a continuous aqueous phase. In contrast, reverse microemulsions consist of aqueous domains (termed reverse micelles) dispersed in a continuous oil phase. Reverse microemulsions are of special interest since a variety of reactants can be introduced into the nanometer-sized aqueous domains for reaction confined within the reverse micelles, leading to materials with controlled size and shape [1,2]. In the past few years, significant research has been conducted in the reverse microemulsion-mediated synthesis of organic systems (e.g. polymeric nanoparticles [3-7]) and inorganic systems (e.g. quantum dots [8-13], metallic nanoparticles [14-17] and ultrafine ceramic particles [15,18-24]).

Synthesis of inorganic nanoparticles within reverse microemulsions has the potential to yield non-agglomerated materials with unique compositional control. In the sol-gel processing of complex oxides, whereby the different metal alkoxide precursors can have substantially different hydrolysis rates [25], a reverse microemulsion medium may provide a means to attain materials with enhanced chemical homogeneity by confining the hydrolysis and polycondensation reactions to nanometer-sized reverse micellar domains. In this approach, we can select the appropriate alkoxide precursors and adjust their concentrations, such that their diffusion rates through the oil phase are matched, allowing them to undergo hydrolysis simultaneously upon reaching the aqueous domains. In this thesis, a reverse microemulsion medium was employed for the synthesis of barium hexaaluminate (BHA) catalysts of interest to methane combustion applications. The improved compositional uniformity attainable with this novel method could yield non-agglomerated nanoparticles that would undergo crystallization at lower temperatures, thereby minimizing grain growth and maximizing specific surface area. The reverse microemulsion medium was also flexible towards surface deposition of active species on BHA nanoparticles to achieve nanocomposite systems with excellent catalytic activity.

Ionic surfactants, such as Aerosol OT, sulfonated hydrocarbons and succinates are typically used in reverse microemulsion-mediated synthesis of organic and inorganic particles. However, the anions or cations associated with the ionic surfactants may potentially contaminate the material of interest. For example, we have found that the synthesis of γ-Al_2O_3 nanoparticles in reverse micellar systems stabilized by sodium dodecyl sulfate led to materials with ~2 at% sulfur [26]. Sulfates species confer strong surface acidity to catalysts [27], which may be undesirable for certain reactions.

Non-ionic surfactants have been recently studied for the synthesis of high-purity materials [23,28,29]; polyethoxylated alcohols have been examined with particular interest. While some studies have been conducted on the phase behavior of microemulsions stabilized by pure hexaethoxylated nonynol or pentaethoxylated hexanol [30-33], little information is available on systems stabilized by commercially available surfactant mixtures. This chapter describes the synthesis of water/iso-octane and water/cyclohexane reverse microemulsions of interest to the mediated sol-gel processing of barium hexaaluminate-based materials. The systems were stabilized by commercially available polyethoxylated alcohols. Medium-chain linear alcohols (e.g. 1-pentanol) were employed as co-solvents in these systems to help balance the surfactants' affinity to water and oil.

During sol-gel processing, metal alkoxide precursors are hydrolyzed to yield hydroxides or oxy-hydroxides and short-chained alcohols in an exothermic reaction:

$$M(OC_nH_{2n+1})_x + xH_2O \longrightarrow M(OH)_x + xC_nH_{2n+1}OH \qquad (2.1)$$

The metal hydroxides subsequently undergo polycondensation, whereby oxygen bridges are formed between metal atoms, and water is generated [34]:

$$M(OH)_x + M'(OH)_y \longrightarrow (HO)_{x-1}\text{-}M\text{-}O\text{-}M'\text{-}(OH)_{y-1} + H_2O \qquad (2.2)$$

Thus, the phase stability of reverse microemulsions in the presence of short-chained alcohols and at different temperatures is important towards achieving well-defined nanoparticles in the mediated sol-gel processing. This chapter presents the phase behavior, micellar structure and stability of water/iso-octane and water/cyclohexane systems for the controlled synthesis of BHA nanoparticles.

2.2 Experimental

Reverse microemulsions were prepared with iso-octane (2,2,4-trimethylpentane, 99.9%, Aldrich) or cyclohexane (99.9%, Aldrich) as the oil phase. The Neodol 91-6 surfactant (Shell Chemical) used consisted of polyethoxylated alcohols with an average of 6 units of ethylene oxide per mole of alcohol, and an average hydrocarbon chain length of 10. It was stirred with 1-pentanol (99.9%, Aldrich) to give a 67%-33% surfactant/co-solvent mixture by weight. The hydrophilic-lipophilic balance (HLB) of this mixture was calculated to be 11.82 according to the method proposed by Davies [35]. The surfactant mixture was added to the two-phase water/oil mixture until a clear, one-phase system was obtained. The reverse microemulsions were set aside to verify that phase separation would not occur after stirring was stopped; additional surfactant mixture was added if necessary to achieve a stable one-phase system.

Thermal stability experiments were conducted with a circulating water bath. Reverse microemulsions containing the minimum amount of surfactant required for their stabilization were heated until a cloud point was observed. Extra surfactant was then added with stirring until a transparent system was re-established. Experiments were also performed to determine the stability of reverse microemulsions in the presence of short-chained alcohols. Iso-propanol (99.9%, Mallinkrodt) was introduced to a reverse microemulsion until a cloud point was noted. Extra surfactant was then added to re-establish the transparency of the system.

Quasi-elastic (dynamic) light scattering (QELS) experiments were conducted on the reverse microemulsions at 25°C using a Lexel 95 Argon-ion laser and a Brookhaven high-precision photomultiplier at 90°. Data were acquired using a Brookhaven 9000AT correlator. The periods for acquisition of the autocorrelation function were 0.1 μs to 0.5 s. Particle size distribution was obtained from non-negatively constrained least-squares (NNCLS) analysis of the data [36]. Viscosity measurements were conducted using Glimont capillary flow viscometers at constant temperature. Electrical conductivity measurements were performed with a Copenhagen Radiometer conductivity cell CDC14 (1-cm^{-1} cell constant) connected to a Copenhagen Radiometer CDM80 conductivity meter.

Small-angle neutron scattering (SANS) experiments were performed on the 30-m SANS instrument on neutron guide NG3 at the Center for Neutron Research of NIST. The instrument utilizes a mechanical velocity selector as monochromator, a circular pinhole collimation, and a two-dimensional position-sensitive detector (65 x 65 cm^2) for data collection over a range of angles simultaneously. Data were taken with 6-Å neutrons and sample-to-detector distances of 2 m and 13 m, which covered a range of scattering vectors Q (0.04-3.0 nm^{-1}). The data were corrected for background, empty-cell scattering and sample transmission, as described elsewhere [37]. Reverse microemulsion samples for SANS analysis were prepared by substituting protonated water with heavy water in the synthesis described earlier. Conversely, for the SANS studies of regular microemulsions, the protonated hydrocarbons were substituted by their deuterated isotopes. Microemulsion samples for SANS contrast matching experiments were prepared by substituting the hydrocarbons by deuterated species, and by adding protonated water to D_2O to obtain the same scattering length density for both phases. Deuterated compounds were obtained from Cambridge Isotope Laboratories, Inc. (Andover, MA) and used without further purification.

2.3 Results and Discussion

2.3.1 Phase Behavior

We found that Neodol 91-6/1-pentanol surfactant mixture could be used to stabilize microemulsions over a wide range of water:oil ratios. Figure 2.1 illustrates the ternary phase diagrams for the water/iso-octane/surfactant and water/cyclohexane/surfactant systems. These diagrams indicate that the amount of surfactant mixture required to stabilize the microemulsions was lower for the water/iso-octane system than for the water/cyclohexane system. We are particularly interested in the reverse microemulsions containing water volume fractions (ϕ_w) of 0.05-0.15, since this ϕ_w range was found to be optimal for the synthesis of complex oxides through reverse microemulsion-mediated sol-gel processing [23]. At ϕ_w=0.1, the surfactant volume fractions (ϕ_s) required to stabilize the reverse microemulsion are 0.13 and 0.20 for the iso-octane-based and cyclohexane-based systems, respectively. At a higher water content

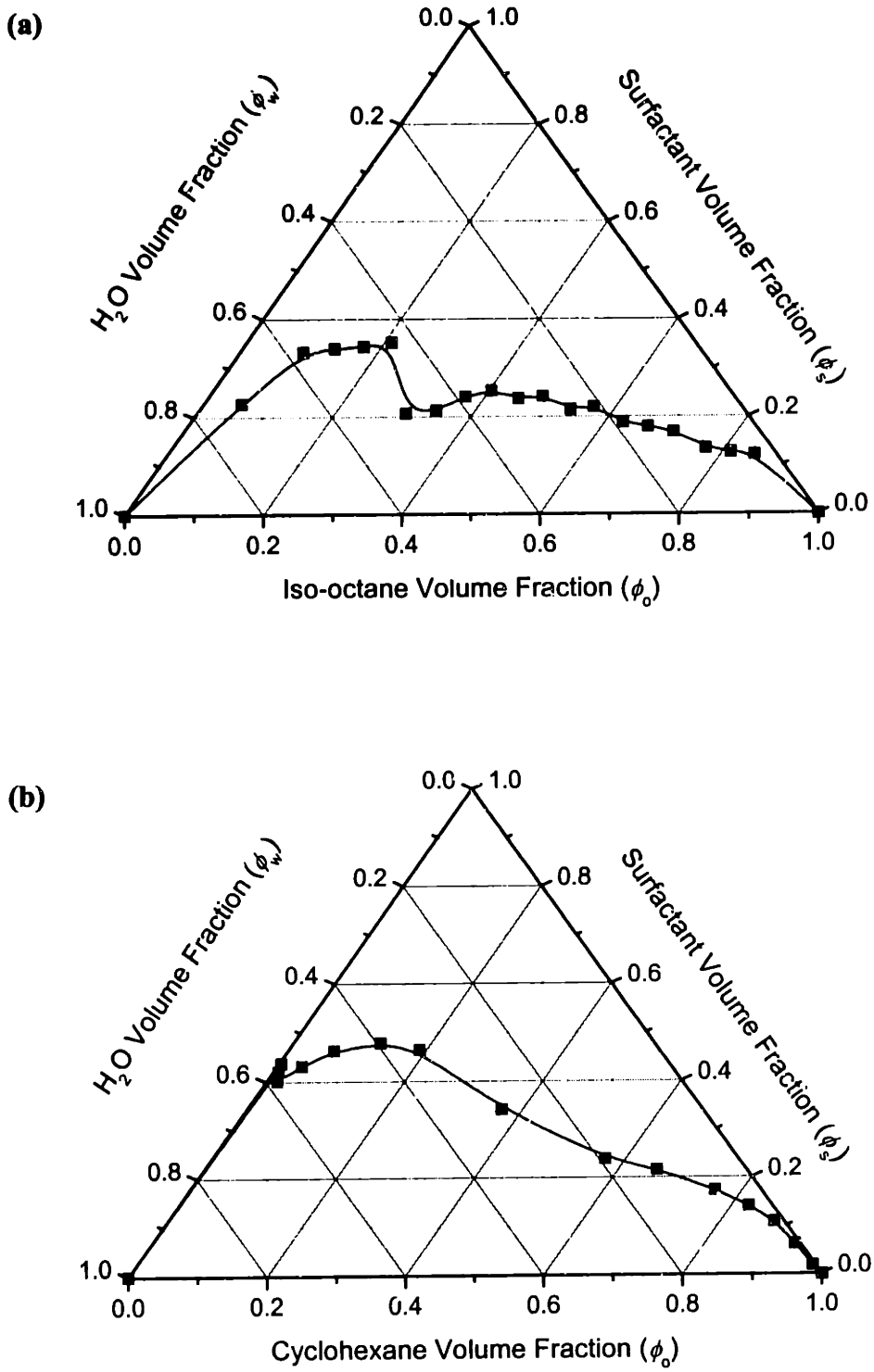

Figure 2.1. Pseudo-ternary phase diagrams for (a) the water/iso-octane/surfactant system and (b) the water/cyclohexane/surfactant system. The surfactant mixture consisted of 66.7 wt% Neodol 91-6 and 33.3 wt% 1-pentanol.

of ϕ_w=0.3, ϕ_s values of 0.23 and 0.38 were required to stabilize the iso-octane-based and cyclohexane-based systems, respectively. The difference in the surfactant requirements for the two systems could be attributed in part to the difference in compatibility between the surfactants' hydrophobic tails and the respective oil phase. The saturated linear hydrocarbon tails of the surfactants should be more soluble in iso-octane than in cyclohexane. This would lead to a reduced interfacial area between the oil phase and the amphiphilic film for the former, resulting in a lower surfactant requirement.

For the water/iso-octane system, the required surfactant volume fraction (ϕ_s) increased gradually with water content and reached a local maximum at ϕ_w~0.35. After this point, the surfactant fraction decreased slightly from ϕ_s=0.25 at ϕ_w=0.35 to ϕ_s=0.21 at ϕ_w=0.49. The required surfactant fraction then increased abruptly, reaching a maximum value of 0.35 at ϕ_w~0.55.

The phase diagram of the water/cyclohexane/surfactant system was significantly different from that of the water/iso-octane/surfactant system. A much larger amount of surfactant was required to stabilize the water/cyclohexane system, especially at low oil volume fractions of ≤0.4. Additionally, unlike the iso-octane system, the ternary phase diagram for the cyclohexane system did not show the abrupt changes in ϕ_s, which were indicative of phase transitions. There were, however, two inflection points in the phase diagram of the cyclohexane system, which might correspond to phase transitions.

To investigate if the features observed in the ternary phase diagrams corresponded to transitions between different microemulsion phases, electrical conductivity, light scattering and neutron scattering experiments were performed on selected compositions in the sections to follow.

2.3.2 Electrical Conductivity

Electrical conductivity illustrates the degree of percolation or the bicontinuous nature of a microemulsion system. At low water volume fractions where discrete reverse micelles were dispersed within a continuous oil phase, the system would have a conductivity similar to that of the oil phase. Conversely, at high water contents where regular micelles were dispersed in a continuous aqueous phase, the system would display a conductivity similar to that of the water used (~160 μs/cm). For microemulsions

containing similar values of ϕ_w and ϕ_o, the conductivity might be intermediate to those of pure water and pure oil. In our case, both iso-octane and cyclohexane have negligible electrical conductivity. Therefore, significant deviation from zero conductivity would imply a certain degree of connectivity between the aqueous domains in the system.

Figure 2.2 shows a plot of electrical conductivity of the water/iso-octane system as a function of ϕ_w. For $\phi_w \leq 0.06$, the conductivity of the system was negligible, suggesting that the water droplets were discrete and have little interaction with each other. Conductivity rose as ϕ_w increased from 0.06 to 0.80, indicating that interaction between the aqueous domains became increasingly important. For $\phi_w \geq 0.8$, conductivity of the system was found to be similar to that of water, suggesting that the system consisted of a continuous aqueous phase with discrete oil droplets.

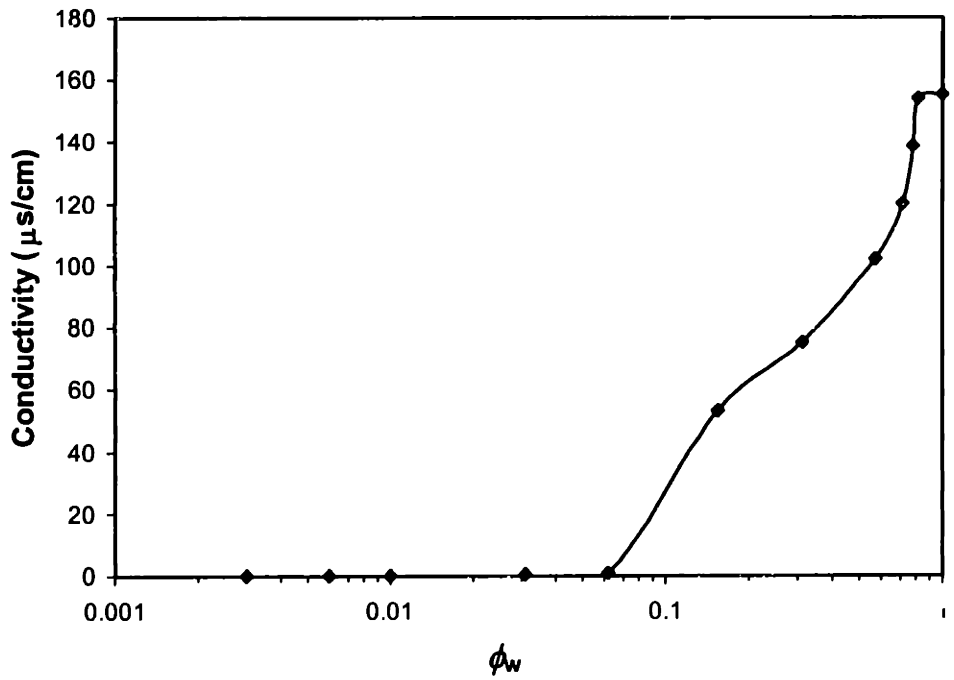

Figure 2.2. Electrical conductivity of water/iso-octane systems as a function of ϕ_w.

For the water/cyclohexane system, zero conductivity was noted for $\phi_w \leq 0.10$ (Figure 2.3). Conductivity increased steadily between $\phi_w \sim 0.10$ and $\phi_w \sim 0.60$, suggesting a bicontinuous system. Systems of $\phi_w \geq 0.6$ showed a conductivity value close to that of water, indicating the presence of a continuous aqueous phase with discrete oil droplets.

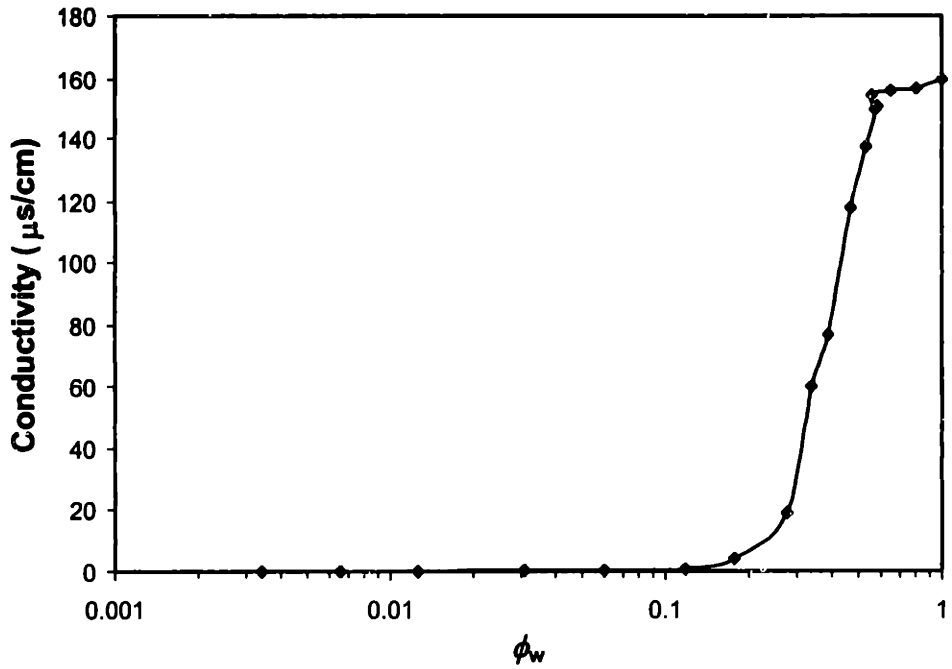

Figure 2.3. Electrical conductivity of water/cyclohexane systems as a function of ϕ_w.

2.3.3 Quasi-Elastic Light Scattering Analysis

Particle size determination by QELS is most reliable at dilute concentrations where the Stokes-Einstein relation can be applied [36]:

$$d_H = \frac{k_B T}{3\pi\eta D_0} \tag{2.3}$$

where d_H is the effective hydrodynamic diameter of the scattering particle, k_B is Boltzmann's constant, T is the absolute temperature, η is the viscosity of the microemulsion, and D_0 is the diffusion coefficient obtained from the decay constant of the scattering distribution,

$$D_0 = \frac{\Gamma}{k^2} \tag{2.4}$$

where Γ is the decay constant of the normalized correlation function, and k is defined as,

$$k = \frac{4n\pi}{\lambda}\sin\frac{\theta}{2} \tag{2.5}$$

In equation (2.5), n is the refractive index of the fluid, λ is the wavelength of the incident light, and θ is the scattering angle.

This analysis is reliable and readily applicable to monodisperse, or slightly polydisperse, non-interacting scattering centers [38]. Particle size analysis by QELS is not meaningful (i) when a strong interaction is present between particles, or (ii) for bicontinuous or lamellar structures. For solutions of finite dilution, the apparent diffusion coefficient measured by QELS can be related to the Stokes-Einstein diffusion coefficient by considering only two-body interactions according to:

$$D_{app} = D_0\{1 + \phi_H[S + H]\} \tag{2.4}$$

where S and H account for the thermodynamic and hydrodynamic interactions between particles, respectively [39]. ϕ_H is the hydrodynamic volume fraction defined as:

$$\phi_H = \frac{4\pi}{3}\bar{\rho}R_H^3 \tag{2.5}$$

where $\bar{\rho}$ is the bulk number density of droplets in the microemulsion, and R_H is the hydrodynamic radius [40].

Previous researchers have observed that the hydrodynamic radius obtained from the application of the Stokes-Einstein equation to QELS data agreed well with values obtained from the neutron scattering data analysis for $\phi_H \leq 0.3$ in water/dodecane reverse microemulsions [40]. For the water/iso-octane system, we found that the hydrodynamic radius of the reverse micelles increased almost linearly with water content from 2.9 nm at ϕ_w=0.003 to 7.3 nm at ϕ_w=0.15 (Figure 2.4, Table 2.1). A significant decrease in the hydrodynamic radius was observed between ϕ_w=0.15 and ϕ_w=0.40. This might be due to an increased level of interaction between aqueous particles (as suggested by electrical conductivity data in Figure 2.2), which could lead to a higher apparent diffusion coefficient, effectively reducing the hydrodynamic radius obtained from the Stokes-Einstein equation. Non-negatively constrained least-squares (NNCLS) analysis of the autocorrelation function showed that the particle distribution agreed well with slightly polydisperse spherical particles for systems of $\phi_w \leq 0.15$. Figures 2.5(a) and (b) illustrate the particle size distribution and residuals of the NNCLS analysis, respectively, for a system of ϕ_w=0.15. The residuals from the statistical fitting of autocorrelation scattering function for systems of $0.005 \leq \phi_w \leq 0.15$ were randomly distributed, indicating that no

systematic error was present in the fitting operation. In contrast, NNCLS analysis did not produce satisfactory fitting of autocorrelation data for systems of ϕ_w>0.15.

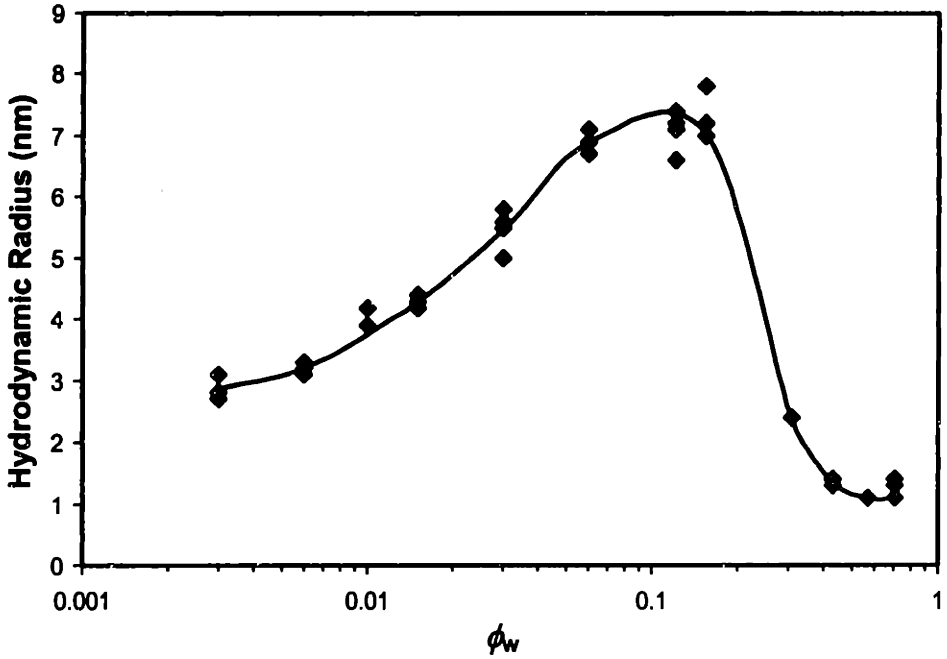

Figure 2.4. QELS hydrodynamic radius for water/iso-octane systems as a function of ϕ_w.

Table 2.1. Hydrodynamic radius and polydispersity from Stokes-Einstein analysis, and average radius from NNCLS analysis of QELS correlation data for water/iso-octane systems.

ϕ_w	Stokes-Einstein Hydrodynamic Radius (nm)	Polydispersity	NNCLS Average Radius (nm)
0.003	2.9	0.37	2.4
0.005	3.1	0.21	2.9
0.010	4.0	0.23	3.9
0.015	4.3	0.18	4.0
0.030	5.5	0.23	5.3
0.060	6.9	0.32	6.7
0.12	7.0	0.31	7.0
0.15	7.3	0.12	7.2

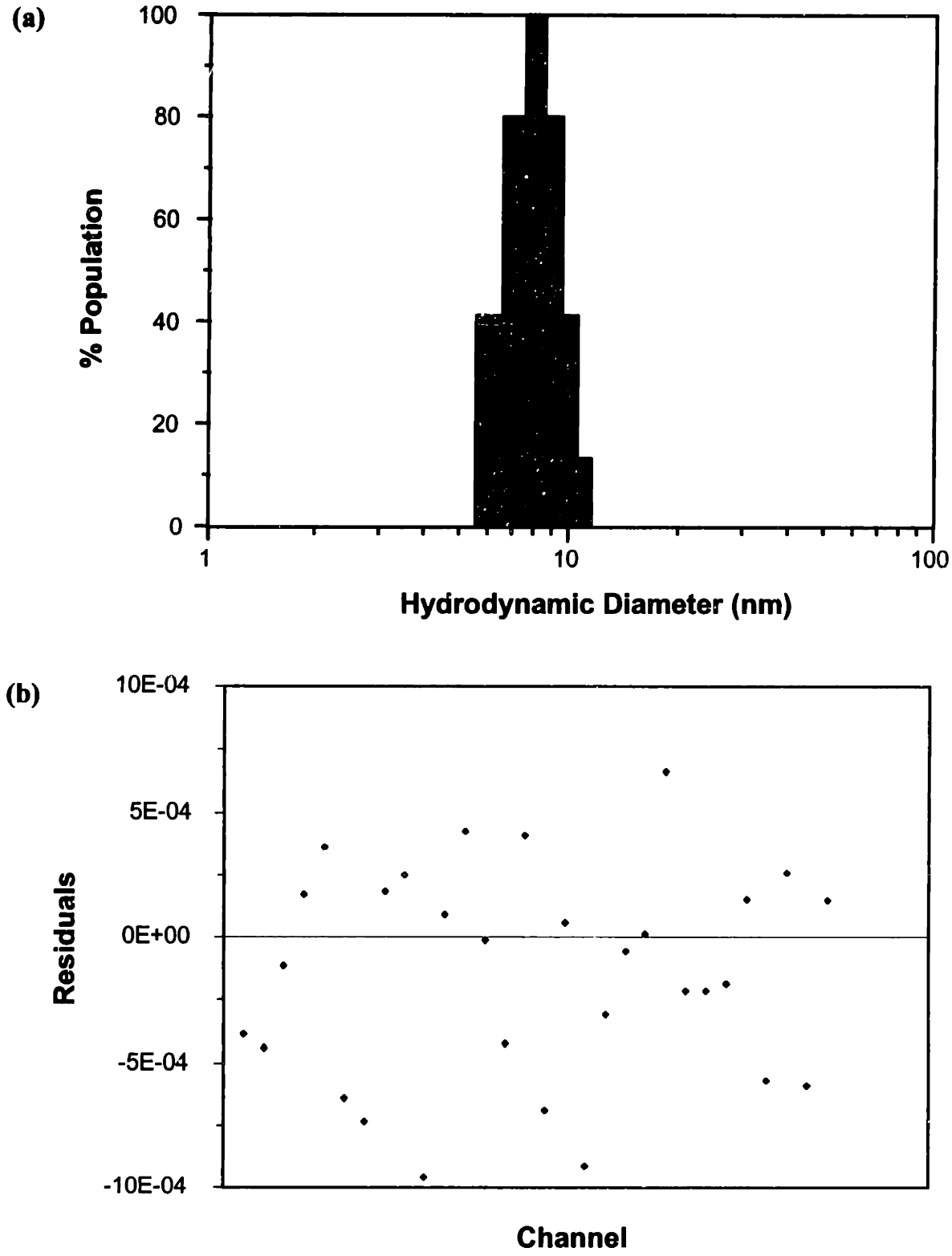

Figure 2.5. (a) NNCLS particle size distribution and (b) residual analysis for a water/iso-octane system of ϕ_w=0.15.

For example, a bimodal particle size distribution was noted for the system of ϕ_w=0.25, centering at <2 nm and ~100 nm (Figure 2.6(a)). Analysis of the residuals showed a sinusoidal pattern (Figure 2.6(b)), indicating that a systematic error was present in the fitting operation. These results indicated that accurate particle size analysis could not be performed with QELS for systems of ϕ_w>0.15, which might be attributed to the high levels of interaction between aqueous particles. These findings agreed well with the significant electrical conductivity values noted for systems of ϕ_w>0.15 (Figure 2.2). In the water-rich region of the phase diagram (ϕ_w>0.55), a low level of interaction between discrete oil droplets could be expected in a continuous aqueous phase. However, meaningful QELS data could not be collected for oil particle size distribution in the water-rich region due to weak scattering and significant fluctuations in the baseline.

Relatively smaller particle sizes were attained for the water/cyclohexane system (Figure 2.7, Table 2.2) than for the water/iso-octane system. At ϕ_w=0.03, a hydrodynamic radius of ~2.8 nm was determined for the water/cyclohexane system; a slightly polydisperse NNCLS radius distribution around 2.9 nm with random residual scatter was obtained. Analysis of QELS data was meaningful up to ϕ_w=0.10, where a hydrodynamic radius of ~4.5 nm and a NNCLS radius distribution around 4.6 nm were calculated. Significant fluctuations in the baseline and multimodal scattering autocorrelation functions prevented the meaningful statistical analysis of data for systems of ϕ_w>0.10. This agreed well with the conductivity measurements for the water/cyclohexane systems, which suggested significant percolation effects at ϕ_w>0.10.

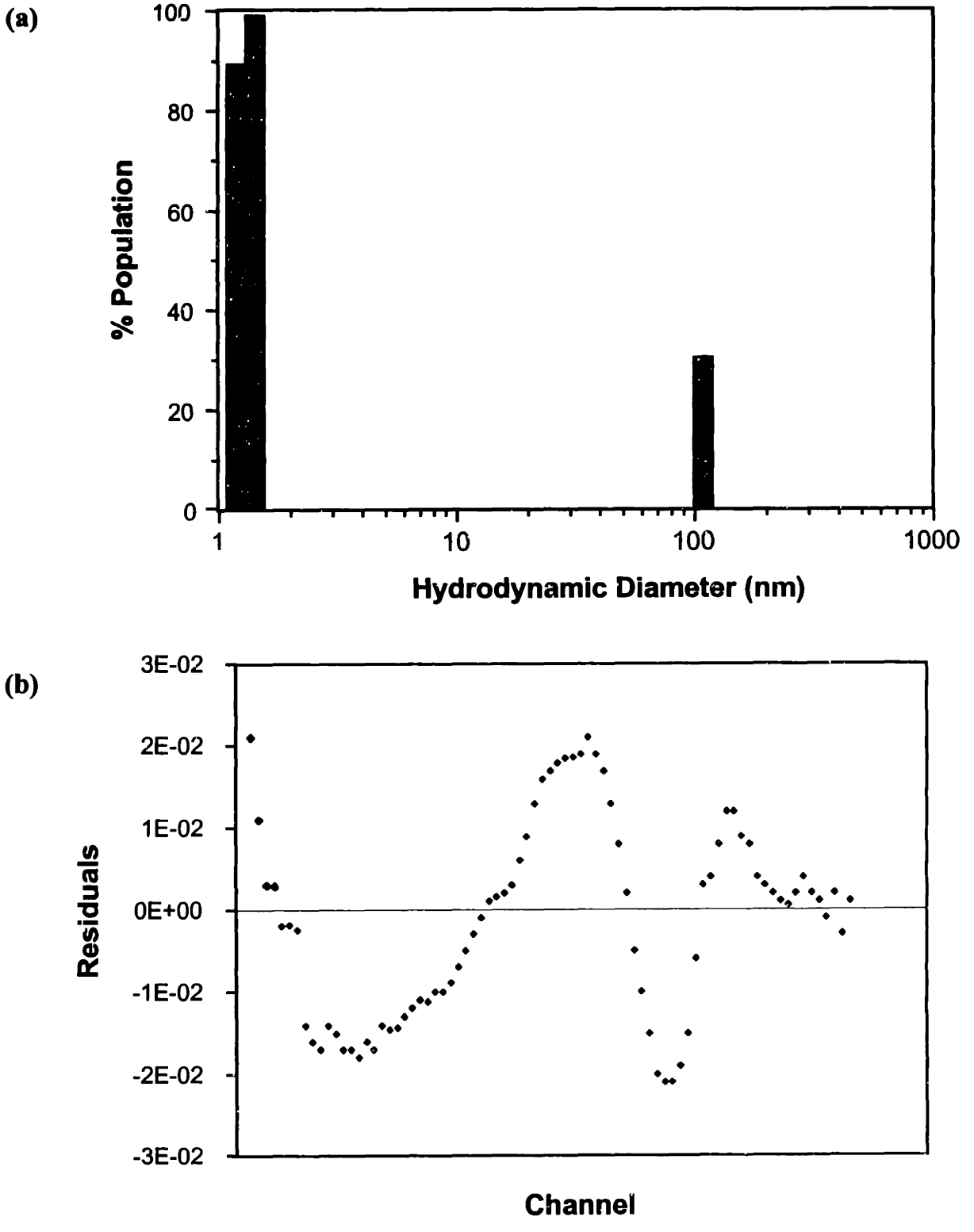

Figure 2.6. (a) NNCLS particle size distribution and (b) residual analysis for a water/iso-octane system of ϕ_w=0.25.

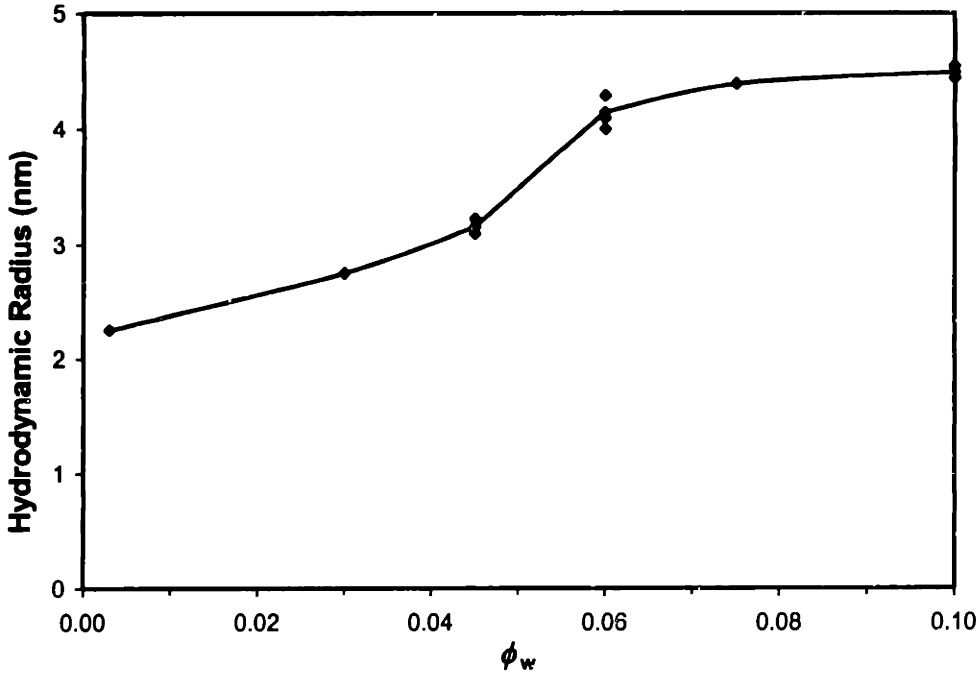

Figure 2.7. QELS hydrodynamic radius for water/cyclohexane systems as a function of ϕ_w.

Table 2.2. Hydrodynamic radius and polydispersity from Stokes-Einstein analysis, and average radius from NNCLS analysis of QELS correlation data for water/cyclohexane systems.

ϕ_w	Stokes-Einstein Hydrodynamic Radius (nm)	Polydispersity	NNCLS Average Radius (nm)
0.003	2.3	0.26	2.3
0.012	2.4	0.32	2.4
0.030	2.8	0.31	2.9
0.045	3.2	0.30	3.2
0.060	4.2	0.36	4.6
0.075	4.4	0.28	4.4
0.10	4.5	0.34	4.6

2.3.4 Small-Angle Neutron Scattering Analysis

QELS provided valuable particle size data on the oil-rich systems, including the $0.05 \leq \phi_w \leq 0.15$ range that was of great interest for reverse microemulsion-mediated synthesis of nanoparticulate materials. However, limited information was obtained from

QELS for systems with intermediate or high water contents. To elucidate the particle size as well as the aggregation state of the aqueous and oil phases for a wide range of microemulsion compositions, SANS experiments were conducted on the water/iso-octane and water/cyclohexane systems.

Figure 2.8 plots the absolute scattering intensity (I_o) as a function of scattering length (q) for D_2O/iso-octane systems of $0.01 \leq \phi_w \leq 0.12$. The data were fitted using a model for polydisperse spherical particles with a core-shell structure [41]. The form factor of the spherical core was calculated assuming a hard sphere model with the Percus-Yevick approximation [42], and was normalized by the average particle volume [43]. The scattering length density (SLD) of the inner aqueous core ($\sim 6 \times 10^{-6}$ Å^{-2}) matched well with that of pure D_2O (6.4×10^{-6} Å^{-2}). The shell appeared to be composed of partially hydrated surfactant molecules, since its SLD (-1×10^{-7} Å^{-2}) was slightly larger than that expected for the linear hydrocarbon tails and the ethylene oxide head groups ($\sim -3 \times 10^{-7}$ Å^{-2}), suggesting the presence of a small concentration of D_2O. The SLD of the solvent (-5×10^{-7} Å^{-2}) obtained from modeling matched well with that of protonated iso-octane (-5.2×10^{-7} Å^{-2}). The thickness of the shell remained relatively constant for systems of $0.01 \leq \phi_w \leq 0.12$, while the core radius increased almost linearly with water content. The total particle radius (core radius + shell thickness) from SANS modeling (Table 2.3) matched well with the hydrodynamic radius obtained from QELS (Table 2.1) for systems of low water contents.

Contrast matching experiments at low water contents were performed to investigate the distribution of amphiphiles in the reverse microemulsions. As expected, the core diameter remained unchanged for systems prepared with protonated or deuterated iso-octane. Protonated samples have shells of ~3 nm in thickness, independent of water content, while deuterated samples have thinner shells of ~1.8 nm. This suggested that roughly half of the surfactant tail interpenetrated the oil phase.

The scattering function of the system of $\phi_w = 0.15$ could not be fitted using a core-shell model or a bicontinuous model, suggesting that this sample was composed of a mixture of both phases (Figure 2.9(b)). For $0.18 \leq \phi_w \leq 0.57$, the scattering functions could be fitted with the Teubner-Strey model [44,45] for bicontinuous systems (Figure 2.10).

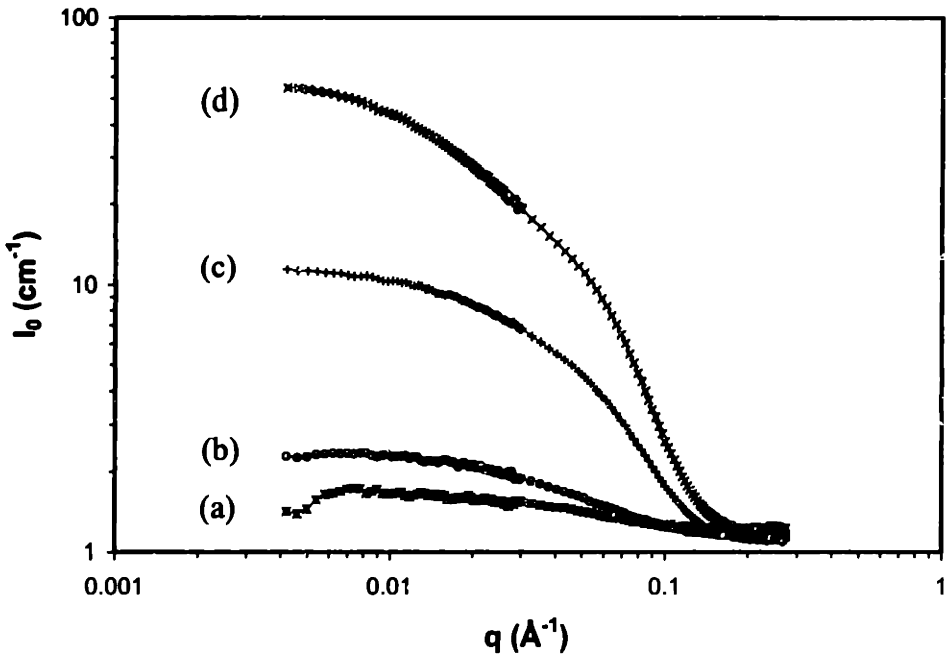

Figure 2.8. Absolute SANS intensity as a function of scattering length for D_2O/iso-octane systems of (a) ϕ_w=0.01, (b) ϕ_w=0.03, (c) ϕ_w=0.06, and (d) ϕ_w=0.12.

Table 2.3. Electrical conductivity, and core radius, shell thickness and polydispersity of aqueous domains obtained from core-shell model fitting of SANS data for D_2O/iso-octane systems with low water contents.

ϕ_w	Electrical Conductivity (μS/cm)	Core Radius (nm)	Shell Thickness (nm)	Polydispersity
0.01	0.2	2.2	3.4	0.6
0.03	0.3	2.6	3.0	0.5
0.06	0.8	3.0	2.9	0.5
0.12	15	4.1	3.1	0.4

This model yields a correlation length ξ, which is a measure of the channel size of the dispersed phase, and a quasi-periodic repeat distance d, which is analogous to the interplanar distance of a periodic system. Contrast matching experiments on systems with intermediate water contents indicated that the correlation length ξ obtained from the Teubner-Strey model corresponded to the characteristic size of the aqueous domains only (without the surfactant film), since similar values of ξ and d were obtained for contrast-matched and regular samples. The correlation length parameters obtained from

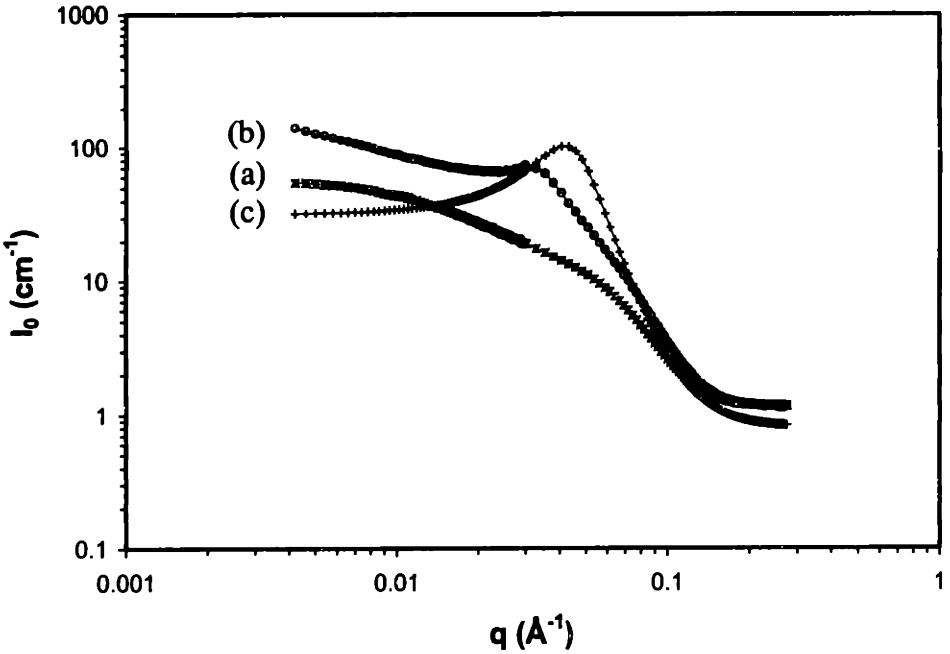

Figure 2.9. Absolute SANS intensity as a function of scattering length for D_2O/iso-octane systems of (a) ϕ_w=0.12, (b) ϕ_w=0.15, and (c) ϕ_w=0.18.

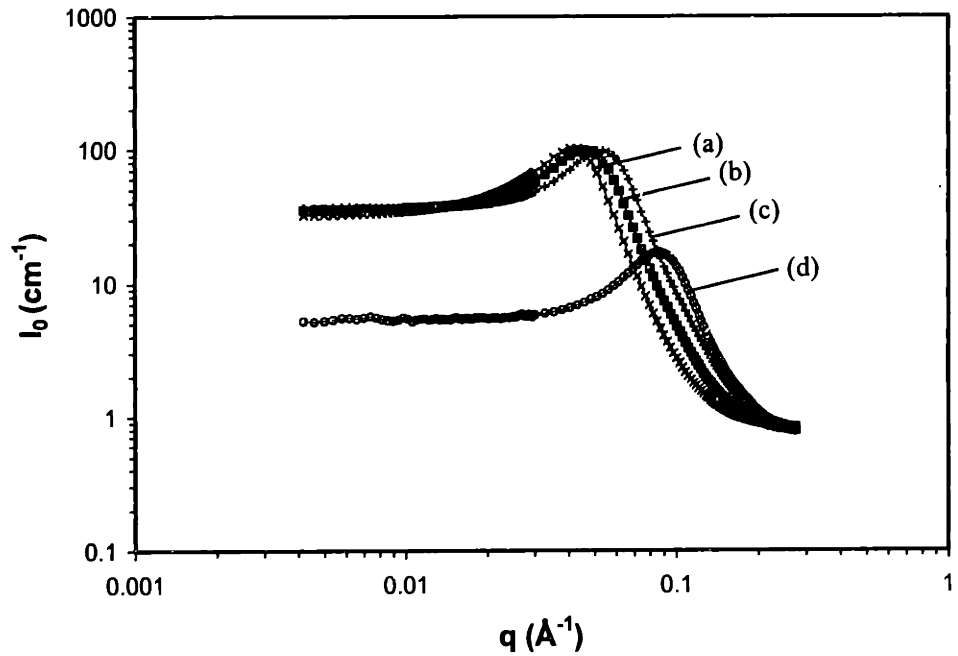

Figure 2.10. Absolute SANS intensity as a function of scattering length for D_2O/iso-octane systems of (a) ϕ_w=0.18 (×), (b) ϕ_w=0.31 (■), (c) ϕ_w=0.45 (+), and (d) ϕ_w=0.57 (○).

fitting the SANS data (Table 2.4) did not correspond well to the Stokes-Einstein hydrodynamic radii from QELS. This was because the hydrodynamic radii obtained from analysis of QELS data were not meaningful for systems of ϕ_w>0.15, since the Stokes-Einstein assumptions of negligible particle-particle interaction and infinite dilution did not apply to these cases.

Table 2.4. Electrical conductivity, and correlation length and quasi-periodic repeat distance of aqueous domains obtained from Teubner-Strey model fitting of SANS data for D_2O/iso-octane systems of $0.18 \leq \phi_w \leq 0.57$.

ϕ_w	Electrical Conductivity (μS/cm)	Correlation Length (ξ) (nm)	Repeat Distance (d) (nm)
0.18	60	8.4	14.4
0.31	80	6.2	12.5
0.45	90	5.4	10.9
0.57	110	3.8	6.8

Systems with high water contents were examined in attempt to elucidate the structure of the oil domains in regular microemulsions. SANS data of the iso-C_8D_{18}/H_2O systems of $\phi_w \geq 0.71$ (corresponding to $\phi_o \leq 0.06$) showed very low scattering intensities; consequently, satisfactory statistical fits could not be obtained for these scattering functions.

The SANS results were in good agreement with the conductivity measurements. The bicontinuous structure proposed for water/iso-octane systems of $0.18 \leq \phi_w \leq 0.57$ corresponded to a high degree of particle interaction, as indicated by the increases in electrical conductivity (Figure 2.2). The SANS results were also in agreement with the phase behavior of the system (Figure 2.1(a)). At low water contents, ϕ_s increased with ϕ_w in the phase diagram; this was consistent with the additional requirement of amphiphilic molecules for stabilization of systems with increasing number density and particle size of discrete aqueous domains. ϕ_s continued to increase gradually with ϕ_w when a bicontinuous structure was formed, since the interfacial area between the aqueous and oil phases would increase with the phase change. A significant increase in surfactant concentration occurred at $\phi_w \sim 0.5$. This matched well with a significant decrease in the

correlation length from the Teubner-Strey model in that region (Table 2.4), which might be attributed to a phase inversion of the system, resulting in an increased interfacial area. Table 2.5 shows the theoretical interfacial area and surfactant requirements calculated based on an estimated molecular cross-sectional area of 40 Å^2 for the surfactant system. The interfacial area for the bicontinuous phase was approximated by a network of cylindrical channels. We noted that the theoretical and actual surfactant requirements agreed well for systems of $0.01 \leq \phi_w \leq 0.57$.

Table 2.5. Theoretical interfacial area, and comparison between theoretical and actual surfactant requirements for water/iso-octane systems with different water contents.

ϕ_w	Interfacial Area (m^2/cm^3)	Theoretical Surfactant Requirements* (ϕ_s^0)	Actual Surfactant Requirements (ϕ_s)
0.01	28	0.04	0.09
0.03	58	0.08	0.12
0.06	88	0.12	0.13
0.12	100	0.14	0.16
0.31	128	0.18	0.23
0.45	143	0.29	0.34
0.57	257	0.36	0.33

*Based on parameters obtained from polydisperse core-shell or Teubner-Strey model fitting of SANS data.

Figure 2.11 and Table 2.6 show the SANS data for the water/cyclohexane system, which were significantly different from those for the water/iso-octane system. The core-shell model, which was applicable for the water/iso-octane systems of $\phi_w \leq 0.12$ could only be used to describe the water/cyclohexane systems of $\phi_w \leq 0.01$. For water/cyclohexane systems of $0.012 \leq \phi_w \leq 0.57$, the bicontinuous model gave the best fit to the scattering data. In contrast to the SANS data, the conductivity measurements showed negligible connectivity between aqueous aggregates for systems of $\phi_w \leq 0.1$ (Figure 2.3). This phenomenon might be explained by the postulate that the aqueous phase for systems of $0.012 \leq \phi_w \leq 0.1$ might have formed a network of cylinder-like structures, which possessed no long-range periodicity and was not fully interconnected. Indeed, analysis of the SANS data showed that at low water contents (e.g. $\phi_w = 0.012$), the correlation length

calculated with the Teubner-Strey model was very small (1.9 nm), and the quasi-periodic repeat distance was relatively large (10.1 nm). In contrast, at intermediate water contents (e.g. ϕ_w=0.27), the correlation length was found to be significantly larger (5.1 nm) with a repeat distance that remained largely unchanged (9.7 nm).

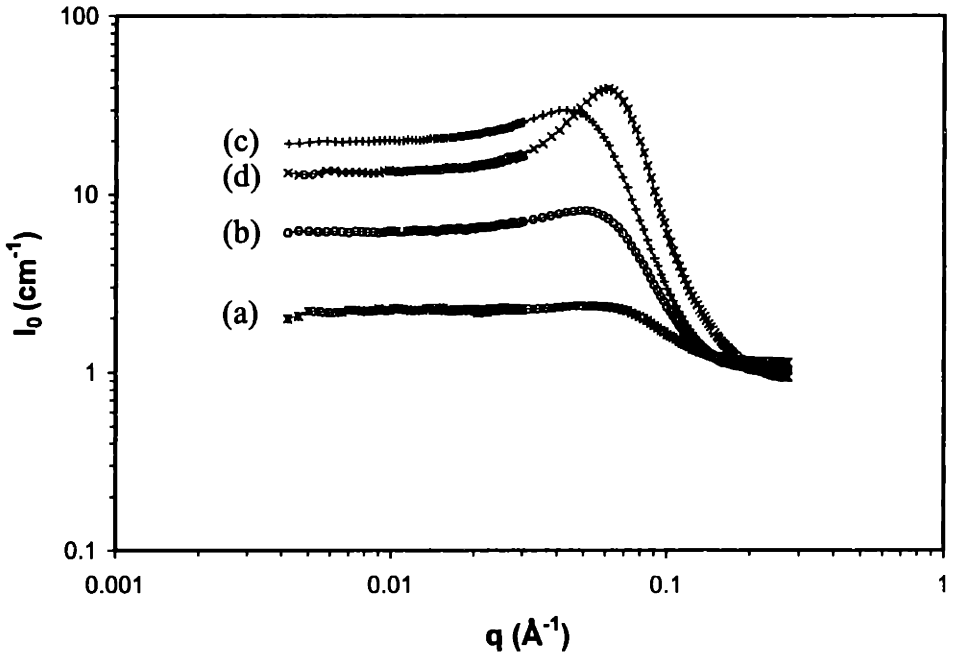

Figure 2.11. Absolute SANS intensity as a function of scattering length for D_2O/cyclohexane systems of (a) ϕ_w=0.012, (b) ϕ_w=0.11, (c) ϕ_w=0.33, and (d) ϕ_w=0.57.

Table 2.6. Electrical conductivity, and correlation length and quasi-periodic repeat distance of aqueous domains obtained from Teubner-Strey model fitting of SANS data for D_2O/cyclohexane systems of $0.012 \leq \phi_w \leq 0.57$.

ϕ_w	Electrical Conductivity (μS/cm)	Correlation Length (ξ) (nm)	Repeat Length (d) (nm)
0.012	0.1	1.9	10.1
0.03	0.2	2.2	9.1
0.06	0.3	3.2	10.8
0.11	0.8	4.3	13.0
0.27	19	5.1	9.7
0.33	60	3.7	6.7
0.57	149	3.1	6.7

As for the water/iso-octane systems with high water contents ($\phi_w \geq 0.71$), theoretical fits of SANS data obtained for the water/cyclohexane systems of $\phi_w \geq 0.69$ were not statistically significant due to the low intensity of the scattering data. The results from the contrast matching experiments on samples with intermediate water contents ($0.012 \leq \phi_w \leq 0.57$) for the water/cyclohexane system were analogous to those obtained for the water/iso-octane system ($0.18 \leq \phi_w \leq 0.57$). Similar values of ξ and d were noted for contrast-matched and regular samples, indicating that the correlation length ξ attained from the Teubner-Strey model corresponded to the characteristic size of the aqueous domains only (i.e. without the surfactant film).

2.3.5 Thermal Stability

In reverse microemulsion-mediated sol-gel synthesis of nanoparticles, heat was expected to be generated by the exothermic hydrolysis reactions of metal alkoxide precursors. Depending on the initial precursor concentration and the water:alkoxide ratio used in the reaction, the temperature of the system might increase by 10°C, which could lead to undesired phase separation of the reverse microemulsion. Figure 2.12 shows a plot of the excess surfactant required for stabilizing water/iso-octane systems with initial water volume fractions of 0.12 and 0.20. The excess surfactant represented the additional volume of Neodol 91-6/1-pentanol mixture introduced to regain transparency of a system when subjected to the temperature noted. Figure 2.12 illustrates that the reverse microemulsions of ϕ_w=0.12 and ϕ_w=0.20 did not require excess surfactant for phase stabilization at the temperature range of interest for mediated sol-gel synthesis (25-35°C). In fact, cloud points corresponding to phase separation did not occur until ~61°C and ~53°C for systems of ϕ_w=0.12 and ϕ_w=0.20, respectively, indicating the excellent thermal stability of these reverse microemulsions. Even at a temperature of ~75°C, these systems could be stabilized by doubling the surfactant amount introduced. Measurements were not conducted above 85°C due to the significant evaporation of iso-octane at such a high temperature.

Although we did not observe any macroscopic phase disruption of our system at temperatures below 50°C, other researchers have identified several phase transitions that could occur upon heating a reverse microemulsion. For example, a system composed of

20 wt% D_2O, 39 wt% n-decane and 41 wt% penta-ethoxylated decanol surfactant would transform from a reverse micellar phase at 25°C to a lamellar phase at ~32°C [46]. A further increase in temperature to ~39°C would give rise to a cubic liquid-crystalline phase, often referred to as the 'sponge phase'. Finally, macroscopic phase separation would occur at 41-42°C. However, no reports have been found in the literature of such temperature-induced phase transitions in H_2O/hydrocarbon systems with ethoxylated alcohols as surfactants and medium-chained alcohols as co-solvents.

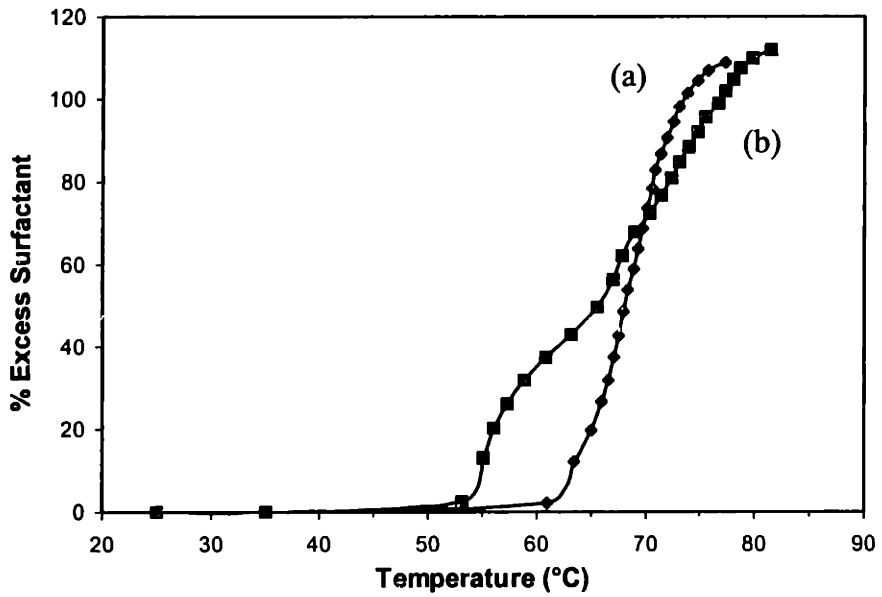

Figure 2.12. Thermal stability of water/iso-octane systems of (a) ϕ_w=0.12 and (b) ϕ_w=0.20, expressed in terms of excess surfactant needed to stabilize the reverse microemulsions at a given temperature.

2.3.6 Stability in the Presence of Short-Chained Alcohols

Short-chained alcohols were produced from hydrolysis of metal alkoxides in the aqueous domains of a reverse microemulsion during mediated sol-gel synthesis. The presence of these compounds might destabilize the reverse microemulsion through possible interactions between the alcohols and the hydrophilic portion of the surfactants. We have investigated the effect of iso-propanol on the phase stability of systems with different water contents. Figure 2.13 shows the excess surfactant required to stabilize the reverse microemulsions as a function of iso-propanol added. The amount of alcohol added was expressed in terms of the iso-propanol:water volume ratio (ϕ_a/ϕ_w).

We noted that the destabilizing effect of iso-propanol depended on the composition of the system. At a low water content of ϕ_w=0.03 (Figure 2.13(a)), the addition of iso-propanol had little effect on the stability of the system. At $0.01 \leq \phi_a/\phi_w \leq 0.50$, white streaks were observed in the system, but the original transparency of the reverse microemulsion was regained by adding <1% excess surfactant. For a system of ϕ_w=0.12 (Figure 2.13(b)), white streaks were again observed as iso-propanol was added to the reverse microemulsion; at $0.03 \leq \phi_a/\phi_w \leq 0.50$, ~10% excess surfactant had to be introduced to recover the initial transparency of the system. For a system of ϕ_w=0.31 (Figure 2.13(c)), 20% excess surfactant was required to stabilize iso-propanol additions at ϕ_a/ϕ_w levels of 0.20-0.50. This study illustrated that for the systems of interest to mediated sol-gel synthesis ($0.05 \leq \phi_w \leq 0.15$), phase stability of our reverse microemulsions could be maintained in the presence of short-chained alcohols through the use of a slightly higher level of surfactants (<20% excess surfactants).

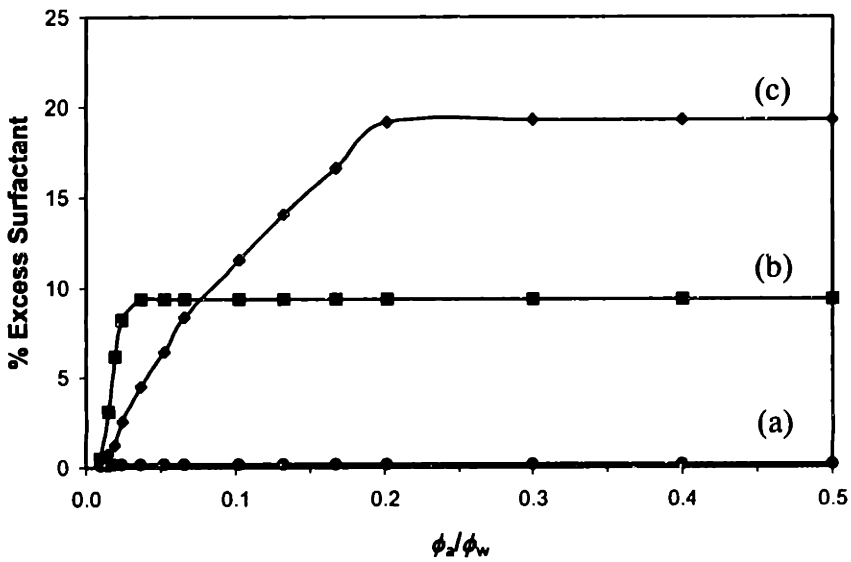

Figure 2.13. Stability of water/iso-octane systems of (a) ϕ_w=0.03, (b) ϕ_w=0.12, and (c) ϕ_w=0.31 in the presence of iso-propanol, expressed in terms of excess surfactant needed to stabilize the reverse microemulsions at a given ϕ_a/ϕ_w ratio.

2.4 Summary

Water/iso-octane and water/cyclohexane reverse microemulsions were successfully synthesized with a Neodol 91-6/1-pentanol surfactant mixture. Significant

differences were noted in the phase behavior of these two systems. The water/iso-octane system required significantly less surfactants for stabilization than the water/cyclohexane system, possibly due to the greater compatibility between iso-octane and the hydrophobic tails of the surfactant.

The reverse microemulsions with low water contents were characterized by discrete aqueous domains and zero conductivity. Increased connectivity or percolation between the aqueous domains was reflected by an increase in electrical conductivity with ϕ_w above 0.06 for the water/iso-octane system, reaching a value close to that of deionized water at ϕ_w~0.80. Conductivity increased gradually with ϕ_w above 0.10 for the water/cyclohexane system, reaching a plateau at ϕ_w~0.60. The gradual rise in electrical conductivity suggested that a bicontinuous structure existed in systems with intermediate water volume fractions.

Quasi-elastic light scattering experiments were performed to obtain the hydrodynamic particle size of the reverse microemulsions. Results from this study were only meaningful at low water contents ($\phi_w \leq 0.15$ for the water/iso-octane system and $\phi_w \leq 0.10$ for the water/cyclohexane system), where a model of slightly polydisperse, non-interacting spherical particles matched well with the scattering autocorrelation function of the samples.

Small-angle neutron scattering experiments illustrated that the water/iso-octane systems of $\phi_w \leq 0.12$ were best described by a polydisperse core-shell model. The core was comprised of D_2O, and the shell was formed by partially hydrated surfactant molecules. The core diameter increased with water content, while the shell thickness remained fairly constant. Contrast matching experiments suggested that the surfactant tails had a certain degree of interpenetration with the solvent phase. At intermediate water contents ($0.18 \leq \phi_w \leq 0.57$), the system was best described by the Teubner-Strey model for a bicontinuous medium. The correlation length and quasi-periodic repeat distance of the system decreased with increasing water content. Compared to the water/iso-octane system, the water/cyclohexane system adopted a bicontinuous structure at a much lower ϕ_w, showing a core-shell structure only at very low water contents ($\phi_w \leq 0.01$).

The water/iso-octane systems were thermally stable up to at least 50°C. Depending on the water content in the system, different amount of surfactant needed to be added to retain phase stability above 50°C. These systems could also be stabilized in the presence of iso-propanol by introducing small amounts of additional surfactants. The excellent stability exhibited by the water/iso-octane system in the presence of the non-ionic surfactant mixture is critical towards reverse microemulsion-mediated sol-gel processing, whereby short-chain alcohols would be produced in the exothermic hydrolysis reaction of metal alkoxide precursors.

2.5 References

[1] M. P. Pileni, *J. Phys. Chem.* **97**, 6961 (1993).

[2] M. A. Lopez-Quintanela, J. Rivas, *J. Coll. Int. Sci.* **158**, 446 (1993).

[3] F. Candau, Z. Zekhini, J. P. Durand, *J. Coll. Int. Sci.* **114**, 398 (1986).

[4] F. Candau, Y. Y. Leong, R. M. Fitch, *J. Polym. Sci. A: Polym. Chem.* **23**, 193 (1985).

[5] G. Voortmans, C. Jackers, F. Deschryver, *British Polym. J.* **21**, 161 (1989).

[6] P. J. Atkinson, M. J. Grimson, R. K. Heenan, A. M. Howe, B. H. Robinson, *J. Chem. Soc., Chem. Comm.* **23**, 1807 (1989).

[7] P. Luthi, P. L. Luisi, *J. Am. Chem. Soc.* **106**, 7285 (1984).

[8] C. Petit, M. P. Pileni, *J. Phys. Chem.* **92**, 2282 (1988).

[9] C. Petit, P. Lixon, M. P. Pileni, *J. Phys. Chem.* **94**, 1598 (1990).

[10] L. Motte, C. Petit, L. Boulanger, P. Lixon, M. P. Pileni, *Langmuir* **8**, 1049 (1992).

[11] P. Llanos, J. K. Thomas, *Chem. Phys. Lett.* **125**, 299 (1986).

[12] M. L. Steigerwald, A. P. Alivisatos, J. M. Gibson, T. D. Harris, R. Kortan, A. J. Muller, *J. Am. Chem. Soc.* **110**, 3046 (1988).

[13] J. Cizeron, M. P. Pileni, *J. Phys. Chem.* **99**, 17410 (1995).

[14] J. H. Fandler, *Chem. Rev.* **87**, 877 (1987).

[15] M. Kisida, T. Fujita, K. Umakoshi, J. Ishiyama, H. Nagata, K. Wakabayashi, *J. Chem. Soc., Chem. Comm.* **7**, 763 (1995).

[16] K. Kurihara, J. Kizling, P. Stenius, J. H. Fendler, *J. Am. Chem. Soc.* **105**, 2574 (1983).

[17] C. Petit, P. Lixon, M. P. Pileni, *J. Phys. Chem.* **97**, 12974 (1993).

[18] V. Chhabra, M. Lal, A. N. Maitra, P. Ayyub, *Coll. Polym. Sci.* **273**, 939 (1995).

[19] V. Chhabra, P. Ayyub, S. Chattopadhyay, A. N. Maitra, *Mater. Lett.* **26**, 21 (1996).

[20] T. Kawai, A. Fujino, K. K. No, *Coll. Surf. A: Phyisicochem. Eng. Aspects* **109**, 245 (1996).

[21] Y. Moriya, N. Nishiguchi, M. Kawakami, R. Hino, *J. Ceram. Soc. Jpn., Int. Ed.* **103**, 565 (1995).

[22] T. Narita, K. Nakagawa, K. Kawasaki, Y. Ozaki, *J. Ceram. Soc. Jpn., Int. Ed.* **104**, 623 (1996).

[23] A. J. Zarur, H. H. Hwu, J. Y. Ying, *Langmuir*, in press.

[24] M. Roth, R. Hempelmann, *J. Mater. Chem.* **9**, 493 (1999).

[25] D. C. Bradley, R. C. Mehrotra, D. P. Gaur, "Metal Alkoxides." Academic Press, New York, 1978.

[26] A. J. Zarur, J. Y. Ying, Unpublished Results, M.I.T., 1999.

[27] C. N. Satterfield, "Heterogeneous Catalysis in Industrial Practice." McGraw-Hill, New York, 1991.

[28] A. J. Zarur, J. Y. Ying, *Nature*, in press.

[29] A. J. Zarur, H. H. Hwu, J. Y. Ying, submitted to *J. Catal.*

[30] P. K. Kilpatrick, C. A. Gorman, H. T. Davis, L. E. Scriven, W. G. Miller, *J. Phys. Chem.* **90**, 5292 (1986).

[31] C. Minero, E. Pelizzetti, *J. Disper. Sci. Tech.* **16**, 1 (1995).

[32] M. Kahlweit, G. Busse, J. Jen, *J. Phys. Chem.* **95**, 5580 (1991).

[33] R. Strey, M. Jonstromer, *J. Phys. Chem.* **96**, 4537 (1992).

[34] C. J. Brinker, "Sol-Gel Science." Academic Press, Boston, 1990.

[35] J. T. Davies, "Hydrophilic-Lipophilic Balance Calculation by Group Additivity." Butterworths, London, 1957.

[36] E. F. Grabowski, I. D. Morrison, *in* "Measurement of Suspended Particles by Quasi-Elastic Light Scattering," (B. E. Dahneke, Ed.), p. 199. Wiley-Interscience, New York, 1984.

[37] C. J. Glinka, J. G. Barker, B. Hammouda, S. Krueger, J. J. Moyer, W. J. Orts, *J. Appl. Cryst.* **31**, 430 (1998).

[38] D. E. Koppel, *J. Chem. Phys.* **57**, 4814 (1972).

[39] H. M. Fijnaut, *J. Chem. Phys.* **79**, 2461 (1981).

[40] N. J. Chang, J. F. Billman, R. A. Licklider, E. W. Kaler, *in* "Micellar Solutions and Microemulsions," (S.-H. Chen, R. Rajagopalan, Eds.), p. 269. Springer-Verlag, New York, 1990.

[41] S. Kline, Electronic Reference, NIST, 1998.

[42] N. W. Ashcroft, J. Lekner, *Phys. Rev.* **145**, 83 (1966).

[43] P. Bartlett, R. H. Ottewill, *J. Chem. Phys.* **96**, 3306 (1992).

[44] M. Teubner, R. Strey, *J. Chem. Phys.* **87**, 3195 (1987).

[45] K.-V. Schubert, R. Strey, S. R. Kline, E. W. Kaler, *J. Chem. Phys.* **101**, 5343 (1994).

[46] J. Stejskal, P. Kratochvil, *Makr. Chem.* **182**, 2435 (1987).

Chapter 3. Reverse Microemulsion-Mediated Synthesis and Structural Evolution of Barium Hexaaluminate Nanoparticles

3.1 Introduction

This chapter discusses the synthesis and characterization of nanostructured barium hexaaluminate (BHA) materials derived via reverse microemulsion-mediated sol-gel processing. Catalytic studies indicate that the high activity of BHA catalyst can be attributed to its high surface area available at the elevated reaction temperatures [1]. The pore structure of the oxide is found to be an important parameter in catalytic combustion as well. We have observed that microporous catalysts with pores $\leq$ 2 nm appear to be less active than mesoporous catalysts (with > 2-nm pores), perhaps due to mass transfer limitations at the high flow velocities (> 50 cm/s) needed for flame stabilization.

The research motivation of this study is to develop an approach for synthesis of complex oxides with ultrahigh surface areas for high-temperature catalytic applications. Through nanostructure processing, we seek to create BHA particles with thermal stability and catalytic activity superior to conventional materials. The strategy is to generate non-agglomerated materials with controlled nanoparticle morphology to attain superb surface area and sintering resistance. This research further seeks to achieve molecular-level chemical homogeneity in complex oxides, so as to induce crystallization of the desired crystalline phase at lower temperatures to effectively suppress BHA grain growth.

Synthesis of catalytic, ceramic, electronic and biochemical systems in reverse microemulsions has been explored recently in several studies [2-6]. This synthetic approach allows particles to be obtained with well-defined geometry and size since processing of materials is confined to the aqueous reverse micelles. With reverse microemulsion-mediated synthesis, nanoparticles can be derived from precursor hydrolysis within aqueous domains of 0.5-10 nm [7]. In this chapter, we have examined the flexibility of this novel synthesis and the importance of subsequent processing to derive BHA materials with ultrahigh surface areas. Our research showed that it was possible to obtain discrete BHA nanoparticles with superior chemical homogeneity by controlling the synthesis parameters. Furthermore, by using novel powder recovery and drying techniques, we were able to enhance the thermal resistance of the nanoparticles, so

that surface areas higher than 100 m^2/g could be maintained at 1300°C. The resulting nanostructured BHA systems were of great interest as catalysts and supports for methane combustion (see Chapters 4 and 5) [8], and other high-temperature catalytic applications.

3.2 Experimental

3.2.1 Synthesis of Reverse Microemulsions

Ionic surfactants, such as AOT (sodium bis(2-ethylhexyl)sulfosuccinate), are typically used in preparing reverse microemulsions for particle synthesis. In our case, cations that may contaminate the BHA system have to be avoided. We have therefore examined a variety of non-ionic surfactants in the derivation of reverse microemulsions (see Chapter 2) [9]. Using polyethoxylated alcohols as surfactants and medium-chained linear alcohols as co-solvents, reverse microemulsions were achieved over a wide range of water contents. This provided a greater flexibility in synthesis control and yield compared to the AOT-containing systems, which formed lamellar structures instead of bicontinuous micellar suspensions at water contents >8 vol%.

The synthesis scheme of nanostructured BHA is illustrated in Figure 3.1. Iso-octane (2,2,4-trimethylpentane, 99.9%, Aldrich) was used as-received for the continuous oil phase of the reverse microemulsions. Deionized water was added to iso-octane to form mixtures containing water volume fractions (ϕ_w) of 0.001-0.57. The surfactant mixture was composed of (i) 66.7 wt% Neodol 91-6 (Shell Chemical), which consisted of polyethoxylated alcohols with an average of 6 units of ethylene oxide per mole of alcohol, and an average hydrocarbon chain length of 10, and (ii) 33.3 wt% 1-pentanol (99.9%, Aldrich). It was added to the water/iso-octane mixture and stirred at room temperature until a clear, stable reverse microemulsion was obtained. The phase behavior and structural analysis of the reverse microemulsions prepared using two different oil phases, including iso-octane, was examined in detail in Chapter 2 of this thesis.

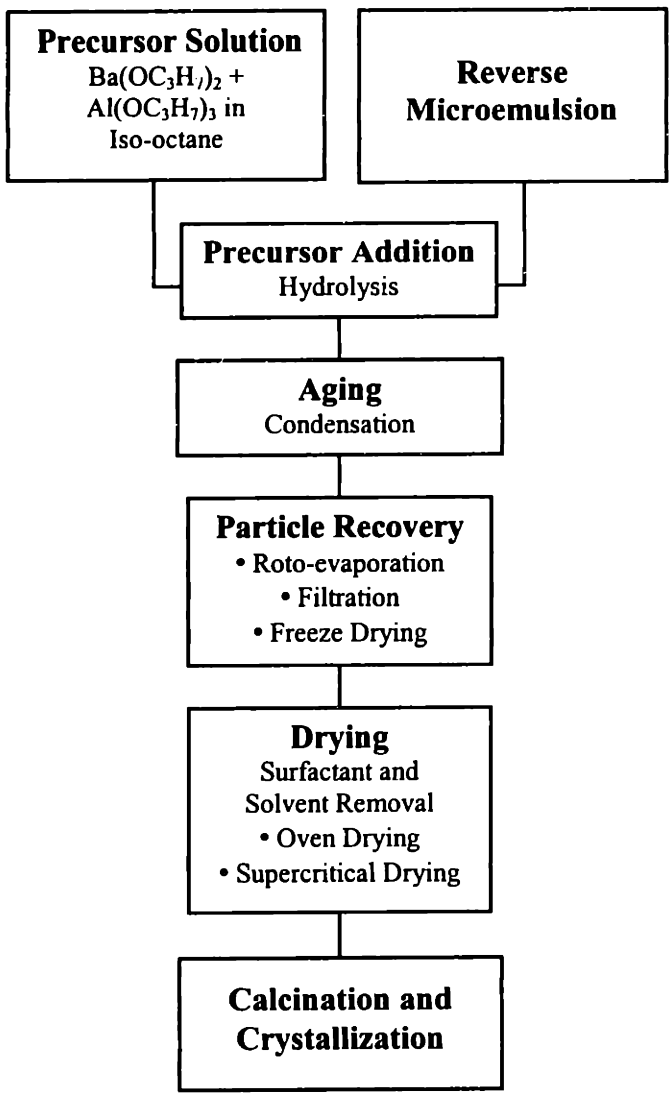

Figure 3.1. Reverse microemulsion-mediated sol-gel processing of BHA nanoparticles.

3.2.2 Hydrolysis of Alkoxide Precursors

Barium iso-propoxide was prepared by refluxing metallic barium (99.9%, Aldrich) in iso-propanol (99.9%, Mallinckrodt) at 70°C for 12 hours. Aluminum iso-propoxide (99%, Aldrich) was dissolved in iso-propanol by refluxing at 80°C for 24 hours; the final alkoxide concentration in iso-propanol was varied between 1 and 10 wt%. The precursor solution was obtained by adding the solutions of barium and aluminum iso-propoxides in an 1:12 molar ratio to previously degassed iso-octane. No sign of hydrolysis was observed when iso-octane was mixed with the alkoxide solutions,

indicating that the water content in the precursor solution was negligible. The precursor solution was then introduced to the reverse microemulsion without exposure to air by use of a cannula. The water:alkoxide molar ratio was varied from 1 to 1000 times the stoichiometric value (0.2529 g of H_2O/g of mixed alkoxides precursor).

The hydrolysis reaction occurred slowly at room temperature, as reflected by the gradual reduction in transparency of the reaction mixture. The mixture was aged at 25°C with stirring for 1-48 hours. The reverse microemulsions with low water contents (ϕ_w=0.001-0.03) underwent phase separations during aging, and a very fine powder was precipitated to the bottom of the flask. The systems with high water contents ($\phi_w \geq 0.06$) remained stable even after prolonged aging.

BHA control samples were also prepared by conventional sol-gel processing. A similar water:alkoxide ratio was used to produce these samples as in the reverse microemulsion-mediated synthesis. The sol-gel derived BHA samples were also aged at 25°C for 1-48 hours.

3.2.3 Particle Recovery and Processing

After aging, the particles were recovered from the reverse microemulsions using various different techniques. One technique induced phase separation of the reverse microemulsion via cooling to -5°C. Upon phase separation, the lighter phase containing iso-octane and a fraction of the surfactants was removed by aspiration and recycled for future use. The heavier phase containing water, iso-propanol, the remaining surfactants and the BHA powders was subjected to filtration with 0.1-μm vacuum quartz frits or filter paper. The filter cake was washed several times with dry iso-propanol to remove residual surfactants. Filtration was not effective at collecting ultrafine particles, particularly those generated from reaction mixtures of high water:alkoxide ratios. Centrifugation and roto-evaporation were also employed to recover the BHA powders from the reverse microemulsions. However, these two techniques failed to recover the particles without causing severe agglomeration.

Freeze drying was developed as an alternative particle recovery approach to the conventional techniques mentioned earlier. In this case, the aged system was sprayed or atomized into a cryogenically cooled vessel, which was then actively evacuated as it was

slowly warmed up to ambient temperature. This allowed effective removal of iso-propanol, iso-octane and water via sublimation, leaving behind BHA particles and residues of heavy surfactants. The BHA particles were recovered and washed with acetone or iso-propanol, and freeze-dried again repeatedly until a dry powder was obtained. Alternatively, the product from one cycle of freeze drying was subjected to heat treatment at 500°C under flowing N_2.

Typically, dry powder was obtained from one cycle of freeze drying for materials prepared from reverse microemulsions with low water contents ($\phi_w \leq 0.03$), whereas two or more cycles were needed for samples synthesized from reverse microemulsions of higher water contents. The freeze-dried powder was washed with dry iso-propanol, and subjected to (i) oven drying at 120°C in air or (ii) supercritical drying at 300°C and 240 bar in flowing argon. The dried samples were next calcined at 500°C first under flowing nitrogen, then under flowing air, to carefully remove the residual surfactants, hydrocarbons and hydroxyl species. Lastly, the pure BHA materials were subjected to heat treatment at temperatures up to 1300°C (2°C/min ramp) under flowing air for 4 hours to obtain the desired crystalline $BaO{\cdot}6Al_2O_3$ phase.

3.2.4 Characterization

Transmission electron microscopy (TEM) and high-resolution transmission electron microscopy (HR-TEM) were performed on the BHA reaction mixture, dried powders, and calcined materials with JEOL 200CX and JEOL 2010EM, respectively. Energy dispersive X-ray (EDX) spectroscopy using JEOL 2010 was employed to evaluate compositional uniformity of the samples. The morphologies of the dried and calcined materials were examined using JEOL 6320 field-emission scanning electron microscopy (FESEM). The crystal structure of the powders was analyzed by X-ray diffraction (XRD) with Siemens D5000 θ-θ diffractometer, operated at 45 kV and 40 mA using Ni-filtered CuK_α radiation. Crystallite size was obtained from peak-broadening analysis of the (114) reflection of BHA ($2\theta = 35.8°$) using Scherrer's method, corrected for instrumental line broadening. Nitrogen adsorption analysis was performed on a Micromeritics ASAP 2000 gas adsorption analyzer. Surface areas and pore size distributions were determined using BET (Brunauer-Emmett-Teller) [10] and BJH

(Barrett-Joyner-Halenda) methods, respectively. Photoacoustic Fourier-transform infrared (PA-FTIR) spectroscopy was employed to examine the surface species on the calcined samples; FTIR spectra were collected at a scan speed of 5 kHz and a resolution of 4 cm^{-1} on a Bio-Rad FTS 60A spectrometer with a MTEC Model 200 Photoacoustic Detector. Thermal evolution of the powders calcined at 500°C was investigated by differential thermal analysis (DTA) on Perkin-Elmer DTA 7 system.

3.3 Results and Discussion

3.3.1 Effect of Microemulsion Composition

As discussed in Chapter 2, the liquid-crystalline phase of the microemulsion system is determined by its composition. Reverse microemulsions of low water contents ($\phi_w \leq 0.12$) were comprised of discrete reverse micelles with a spherical morphology. As the water content was increased, other liquid crystalline phases, such as interconnected cylinders and bicontinuous structures were developed. Inorganic particles synthesized within the reverse microemulsion medium possessed morphologies mimicking that of the aqueous domains in the system. The TEM particle size of powders calcined at 500°C and the BET surface area of materials calcined at 1300°C have been studied for BHA synthesized in reverse microemulsions of various water contents. Figure 3.2 shows that the smallest particle size and highest surface area were obtained by the sample derived in a reverse microemulsion with $\phi_w = 0.12$.

Reverse microemulsions with $\phi_w < 0.03$ underwent phase separation shortly after the addition of the precursor solution; the powders produced could not be stably suspended in the resulting mixture. Particles of ~5-nm diameter were agglomerated to form a gel-like structure (Figure 3.3(a)). Upon calcination at 500°C, surfactants were removed to expose the interparticle porosity in these materials, giving a fairly high surface area of 350 to 550 m^2/g, depending on the water:alkoxide ratio and aging time involved in the synthesis. These inorganic gels were found to be microporous with an average pore size of <20 Å. However, as with conventional sol-gel derived systems, they undergo micropore collapse readily upon calcination to 800°C, resulting in coarse-grained oxides with <20 m^2/g of surface area.

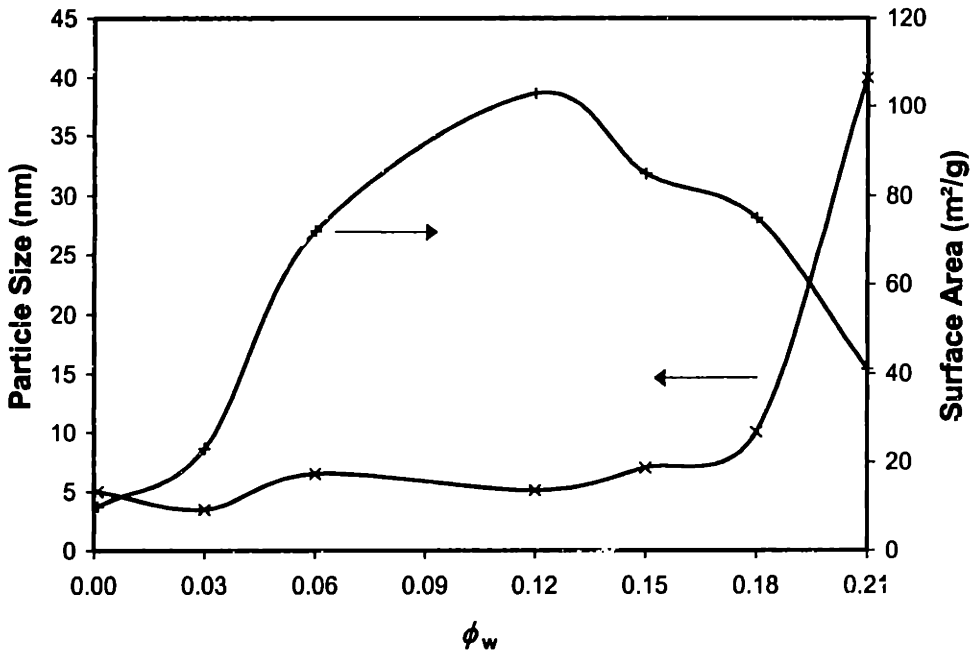

Figure 3.2. Average TEM particle size after calcination at 500°C and BET surface area after calcination at 1300°C for materials synthesized in reverse microemulsions of various water contents at a water:alkoxide ratio 100 times the stoichiometric value.

Discrete spherical inorganic particles of 4-8 nm could be obtained from a reverse microemulsion of $0.03 \leq \phi_w \leq 0.15$ (Figure 3.3(b)). The particle size agreed well with the core diameters of these reverse microemulsions (5-8 nm) obtained from fitting of the SANS data (Table 2.3). These nanoparticles could be crystallized directly to the desired BHA phase at a relatively low temperature of 1050°C, and they possessed an impressive surface area of 100-160 m^2/g even after calcination at 1300°C. The superb thermal stability of these nanoparticles might be attributed to the successful separation of the crystallization and grain growth processes at the high-temperature range. Conventional materials undergo crystallization to the desired BHA phase at 1250-1350°C; there is a tremendous driving force for grain growth at such high temperatures. The high crystallization temperatures were necessary due to the poor chemical homogeneity of the conventional sol-gel derived BHA, which resulted from the different reactivities of the Ba and Al precursors. By using the reverse microemulsion synthesis, the diffusion of the precursors through the oil phase replaced the alkoxide hydrolysis as the rate-limiting

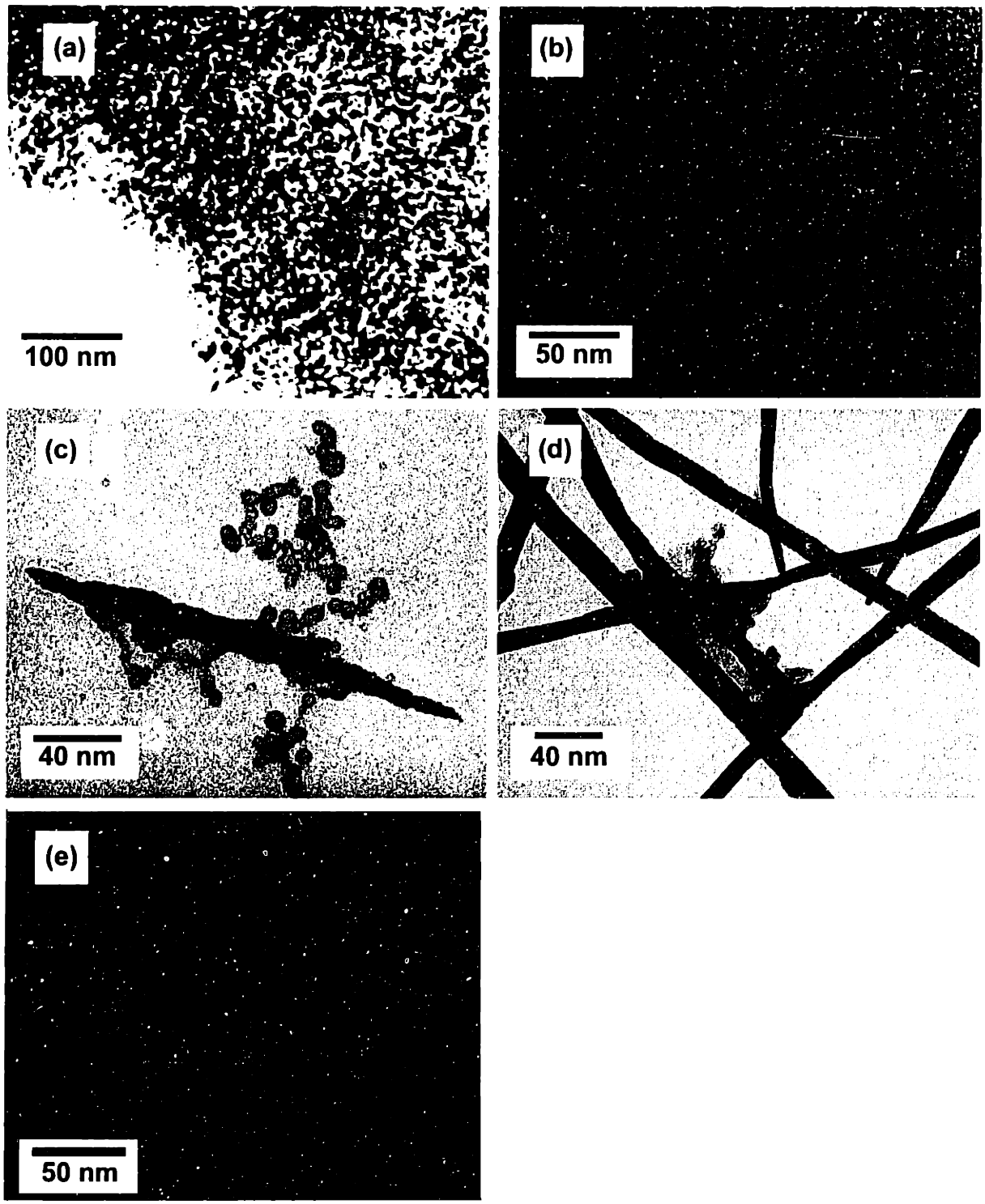

Figure 3.3. Transmission electron micrographs (200 kV) of 500°C-calcined BHA particles derived from reverse microemulsions with ϕ_w of (a) 0.01, (b) 0.12, (c) 0.21, (d) 0.34 and (e) 0.45.

process. Since the Ba and Al alkoxides have similar diffusivities in iso-octane, they were homogeneously reacted within the nanometer-sized aqueous domains of the reverse microemulsions. The superior chemical homogeneity of the nanoparticles derived via reverse microemulsion-mediated synthesis allowed crystallization to be achieved at a significantly lower temperature. After crystallization, grain growth at higher temperatures could be suppressed for BHA due to its complex crystal structure and anisotropic crystal growth [11].

In reverse microemulsions of $0.18 \leq \phi_w \leq 0.21$, significant percolation of the reverse micellar domains might occur, leading to a mixture of liquid-crystalline phases. The materials recovered from these systems showed spherical as well as elongated particle morphologies of sizes ranging between 5 and 15 nm (Figure 3.3(c)). After calcination at 500°C, these samples possessed a relatively low surface area of 150-250 m^2/g. However, crystallization to the desired BHA phase occurred by 1100-1150°C, so that a significant surface area of 60-100 m^2/g was retained after heat treatment at 1300°C. Analysis of the SANS data for these systems indicated that they consisted of a bicontinuous structure with a Teubner-Strey characteristic length of ~8.4 nm and a repeat distance of ~14.4 nm (Table 2.4).

At even higher water contents ($0.24 \leq \phi_w \leq 0.34$), the system was characterized by a bicontinuous phase, as confirmed by electrical conductivity measurements and analysis of the SANS data (Table 2.4). The recovered inorganic materials consisted of elongated, interconnected filaments of ~10 nm in diameter and up to several microns in length (Figure 3.3(d)). The diameter of the filaments matched quite well with the characteristic length of the microemulsion obtained from Teubner-Strey analysis of SANS data (6-8 nm). After calcination to 1300°C, the surface area of these samples was similar to that of conventional sol-gel derived materials.

Previous researchers have also observed formation of filament-like structures in reverse microemulsion-mediated synthesis of barium sulfate [12]. The formation of elongated crystalline particles was attributed to the strong interactions between the inorganic phase and the ionic head group of AOT surfactants. In our case, the interaction between the metal alkoxide precursors and the non-ionic surfactants was much weaker, and could not account for the formation of a secondary phase. The filament-like

materials in our system were likely produced by hydrolysis occurring in a three-dimensional liquid-crystalline structure.

Materials synthesized in microemulsions of $0.45 \leq \phi_w \leq 0.57$ showed a highly crosslinked foam-like structure, which consisted of individual interconnected struts forming open cell units (Figure 3.3(e)). The strut diameter and cell diameter matched well with the correlation length and repeat distance, respectively, obtained from the Teubner-Strey model of the corresponding microemulsions (Table 2.4). BHA foams synthesized in a microemulsion of $\phi_w=0.45$ had strut sizes of 3-6 nm and cell diameters of 10-15 nm, which were in good agreement with the SANS parameters of $\xi=5.4$ nm and $d=10.9$ nm, respectively. We believe the foam-like structure arose from sol-gel reactions within a highly interpenetrated bicontinuous medium. This is consistent with SANS data analysis, which indicated a significant decrease in ξ and d with increasing water content for water/iso-octane microemulsions of $\phi_w \geq 0.45$. The delicate foam-like structure would collapse after calcination at 800°C, giving rise to highly agglomerated materials.

3.3.2 Effect of Water:Alkoxide Ratio

The water:alkoxide ratio determines the relative rates of the hydrolysis and polycondensation reactions. The hydrolysis reaction,

$$M(OC_3H_7)_x + x\,H_2O \rightarrow M(OH)_x + x\,C_3H_7OH, \qquad (3.1)$$

is responsible for creating new seeds, and is favored by a high water:alkoxide ratio. In contrast, the polycondensation reaction,

$$M(OH)_x + M'(OH)_y \rightarrow (OH)_{x-1}M\text{-}O\text{-}M'(OH)_{y-1} + H_2O, \qquad (3.2)$$

gives rise to particle growth of the existing seed, and is promoted by a low water:alkoxide ratio.

The effect of water:alkoxide ratio on materials prepared in a reverse microemulsion of $\phi_w=0.12$ is illustrated by Figure 3.4. The various samples were aged for 24 hours, recovered via freeze drying, and subjected to supercritical drying and calcination at 500°C. With increasing water:alkoxide ratio, the BET surface area of the resulting materials was increased, while the TEM particle size was reduced. Materials prepared with a water:alkoxide ratio 1-10 times the stoichiometric value experienced heavy agglomeration, causing phase separation of the reverse microemulsion. The

recovered samples were similar in characteristics to the conventional sol-gel derived materials. In contrast, materials prepared at a water:alkoxide ratio greater than 10 times the stoichiometric value did not give rise to phase separation of the reverse microemulsion, which remained transparent even after prolonged aging. Depending on the microemulsion composition and the recovery and drying techniques, the powders might retain surface areas as high as 136 m^2/g after calcination at 1300°C (see Table 3.1). The samples synthesized with a water:alkoxide ratio 100 and 1000 times the stoichiometric value have particularly high surface areas when they were supercritically dried.

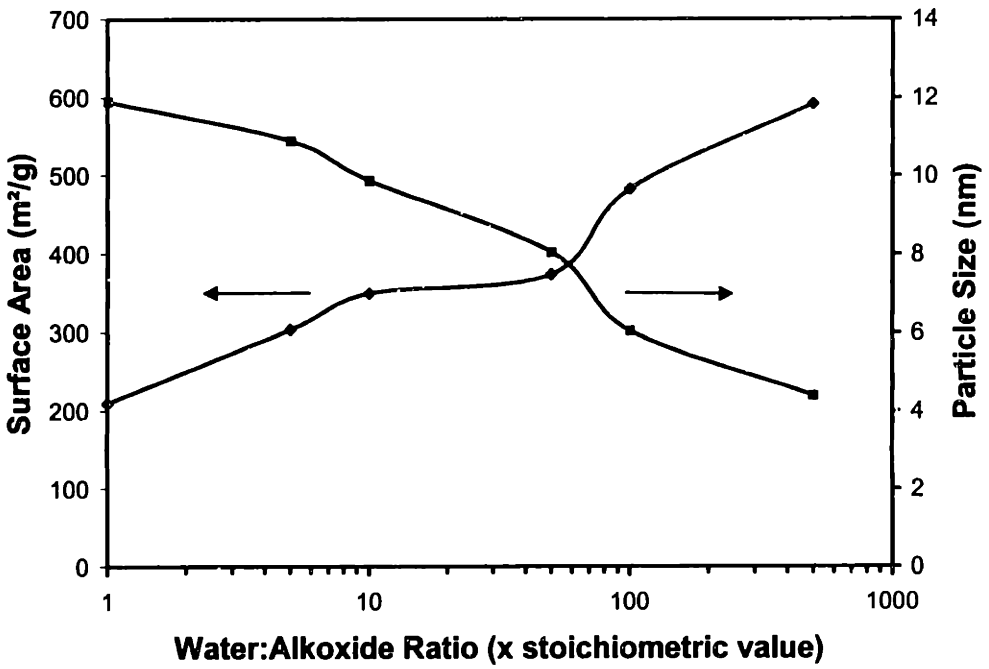

Figure 3.4. BET surface area and average TEM particle size of 500°C-calcined BHA materials synthesized in a reverse microemulsion of ϕ_w=0.12 at different water:alkoxide ratios.

Table 3.1. Surface area of various 1300°C-calcined BHA materials synthesized and processed under different conditions.

Water:Alkoxide Ratio (x stoich. value)	ϕ_w	Average BET Surface Area at 1300°C‡ (m^2/g)		
		Filtered & Oven Dried	Freeze Dried & Oven Dried	Freeze Dried & Supercritically Dried
100x	0 (Control*)	14 ± 1	21 ± 4	16 ± 2
10x	0.12	9 ± 1	15 ± 2	21 ± 2
100x	0.12	21 ± 2	59 ± 6	112 ± 16
1000x	0.12	25 ± 2	69 ± 6	136 ± 30
10x	25	11 ± 1	14 ± 2	24 ± 3
100x	25	19 ± 2	53 ± 7	78 ± 16
1000x	25	34 ± 2	69 ± 15	97 ± 8

*Conventional sol-gel processing.
‡Average surface area from five samples was reported for each material.

3.3.3 Effect of Aging Time

Aging time was found to affect the particle size and extent of polycondensation of the materials. As expected, particle growth could be minimized by short aging periods. However, appropriate aging was critical to ensure completion of the condensation reaction. Full condensation of the hydroxyl species would lead to oxide particles that could be less susceptible to agglomeration during subsequent powder processing.

Figure 3.5 illustrates the evolution of particle size as a function of aging time for two samples synthesized at different water:alkoxide ratios. The materials recovered after very short aging times (< 1 hour) consisted of heavily agglomerated gels. After calcination at 500°C, these gels possessed a surface area of 350-400 m^2/g with pore sizes of 30-40 Å and TEM primary particle sizes of 2-4 nm. They were crystallized to the desired BHA phase at 1250-1300°C, which led to severe grain growth and collapse of the fine pores. The surface area of the fully crystallized materials was 25-30 m^2/g, slightly higher than that of conventional sol-gel derived samples.

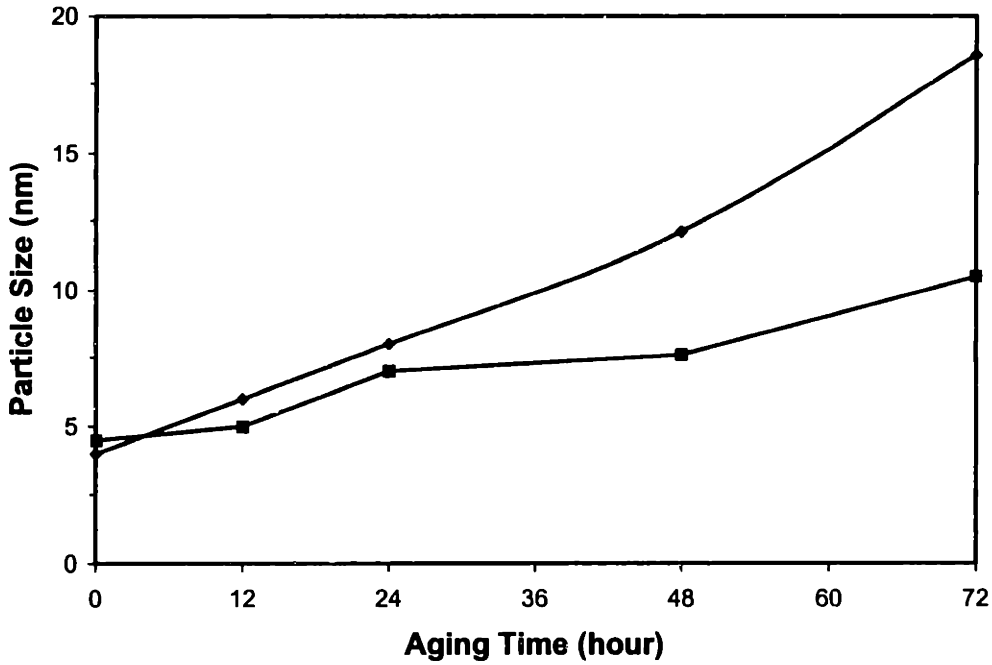

Figure 3.5. Average TEM particle size of freeze dried BHA materials as a function of aging time. The samples were synthesized with a water:alkoxide ratio of (a) 10 times and (b) 50 times the stoichiometric value in a reverse microemulsion of ϕ_w=0.12.

An aging period of 12-24 hours led to discrete particles of 5-8 nm in diameter. These materials agglomerated slightly during recovery and heat treatment at 500°C, yielding aggregates of 30-50 nm in dimension consisting of several small particles of 8-10 nm in diameter. They have a surface area of 200-250 m^2/g with mesopores averaging 10-12 nm in diameter. These materials were crystallized at 1100-1200°C directly from amorphous oxides, retaining a surface area of up to 60 m^2/g after calcination at 1300°C.

An aging period of 24-48 hours was found to produce fully condensed individual particles of 7-12 nm in size. These samples experienced negligible agglomeration during recovery and heat treatment (Figure 3.6). Direct crystallization to the BHA phase occurred at a low temperature of 1050-1100°C; no other crystalline phases were observed during the thermal evolution of these samples. The materials possessed surface areas of 250-500 m^2/g and 40-110 m^2/g after calcination at 500°C and 1300°C, respectively. They were mesoporous in nature, with a narrow pore size distribution centered at 10-20 nm.

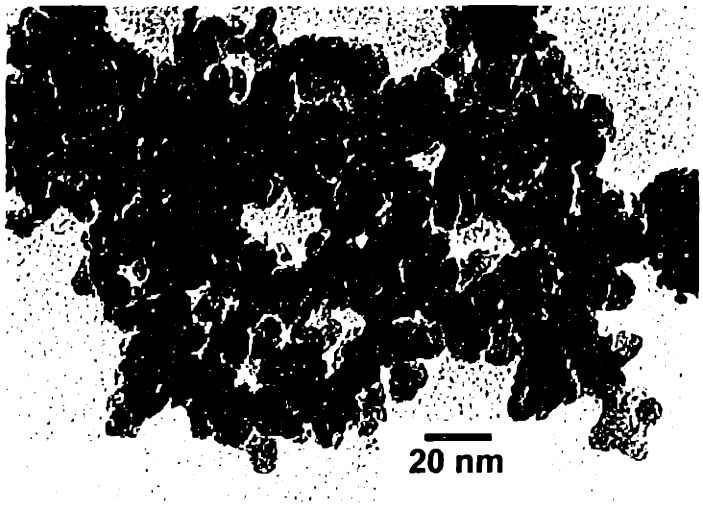

Figure 3.6. Transmission electron micrograph (200 kV) of BHA materials calcined at 800°C in air. The sample was synthesized in a reverse microemulsion of ϕ_w=0.12 at a water:alkoxide ratio 100 times the stoichiometric value, aged for 30 hours, recovered by freeze drying and oven dried.

Extended aging periods (≥ 72 hours) led to the formation of a secondary barium carbonate phase after calcination at 500°C (Figure 3.7(d)). The resulting material required extended calcination at a temperature as high as 1300°C to achieve decomposition of the barium carbonate phase and formation of the desired BHA phase. The elevated temperature required for crystallization promoted severe grain growth and sintering. Consequently, the sample possessed only 8-10 m^2/g of surface area after calcination at 1300°C. Thus, to provide complete condensation of the complex oxide without significant particle growth and secondary phase formation (see Figure 3.7), an optimal aging time of 24-30 hours should be employed.

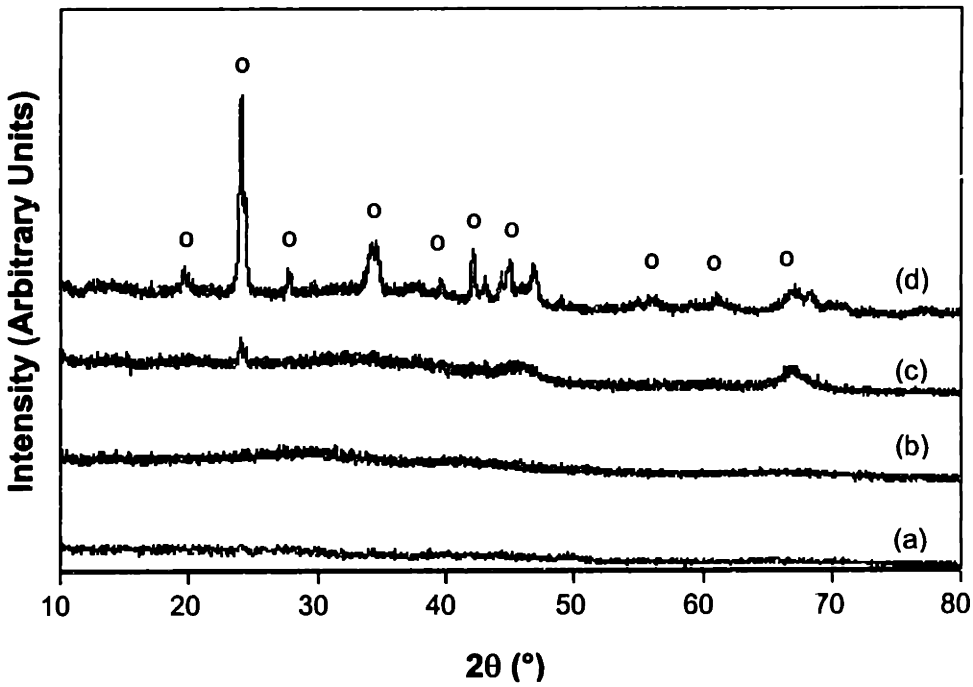

Figure 3.7. XRD patterns of 500°C-calcined samples prepared in a reverse microemulsion of ϕ_w=0.12 at a water:alkoxide ratio 100 times the stoichiometric value, and aged for (a) 12 hours, (b) 24 hours, (c) 48 hours, and (d) 72 hours. Barium carbonate ($BaCO_3$) peaks were denoted o.

3.3.4 Powder Recovery Techniques

We found that conventional techniques such as roto-evaporation, filtration or centrifugation were ineffective at recovering the materials prepared by reverse microemulsion-mediated sol-gel processing. Roto-evaporation resulted in heavy particle agglomeration due to the high temperatures needed to remove the surfactants. The nanometer-sized particles were difficult to collect by filtration or centrifugation. Filtration and centrifugation could be used if phase disruption of the reverse microemulsion was induced first by cooling to -5°C. The oil phase could be recycled, while the particles were filtered or centrifuged from the aqueous phase. This approach also led to some particle agglomeration, but not as severe as in roto-evaporation. The best materials obtained through filtration had a surface area of 25-34 m^2/g after calcination at 1300°C (see Table 3.1). Freeze drying was found to be the most effective technique for recovering materials with high yields, while preventing particle agglomeration. Freeze dried materials preserved their discrete, nanometer-sized particle morphology even after drying and calcination. Depending on the specific drying

technique (oven vs. supercritical drying), the materials recovered via freeze drying could retain an average surface area as high as 136 m^2/g after calcination at 1300°C (Table 3.1).

3.3.5 Drying Techniques

To remove the residual surfactants and volatiles in the recovered particles, samples were subjected to drying in an oven or under supercritical conditions. For freeze dried materials, oven drying and supercritical drying led to high average surface areas of 53-69 m^2/g and 78-136 m^2/g, respectively, after calcination at 1300°C (Table 3.1). The method of drying has an important effect on the particle size and morphology of the resulting materials, as reflected by the distribution of interparticle pore size in Figure 3.8.

Supercritical drying was particularly effective at preventing particle agglomeration and growth during the removal of organics. When combined with freeze drying, supercritical drying led to materials with the highest surface area, with a narrow distribution of pore sizes below 100 Å.

Table 3.1 illustrates that the highest average surface area (136 m^2/g) after calcination at 1300°C was achieved by a system synthesized with a water:alkoxide ratio 1000 times the stoichiometric value in a reverse microemulsion of ϕ_w=0.12, subjected to freeze drying and supercritical drying. Crystallization of this system occurred by 1050°C, and grain growth was minimal in further heat treatment. The successful suppression of grain growth and the discrete nanoparticle morphology of the BHA materials derived by this novel approach led to surface areas that were one order of magnitude higher than that retained by conventional sol-gel derived materials at 1300°C.

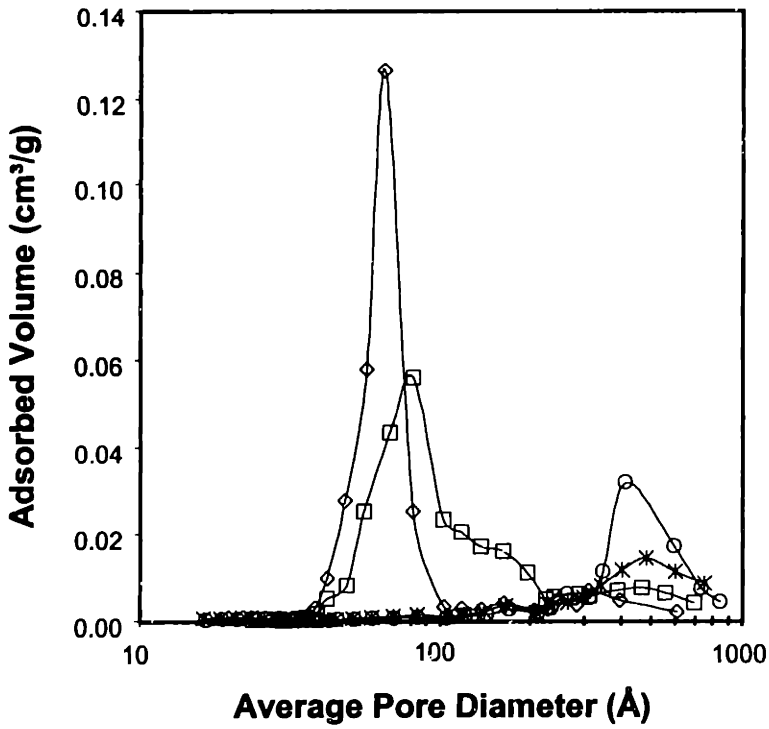

Figure 3.8. Pore size distributions of BHA samples prepared in a reverse microemulsion of ϕ_w=0.12 at a water:alkoxide ratio 100 times the stoichiometric value, calcined to 1300°C; the samples were (a) recovered by freeze drying and supercritically dried (◊), (b) recovered by freeze drying and oven dried (□), and (c) recovered by vacuum filtration and oven dried (○). (d) Pore size distribution of BHA sample prepared by conventional sol-gel processing, recovered by vacuum filtration, oven dried, and calcined to 1300°C (•).

3.3.6 Effect of Calcination Temperature

Structural evolution during heat treatment provides useful information on the microstructural stability of BHA systems, and valuable insights on the chemical homogeneity of the materials derived by reverse microemulsion-mediated synthesis. Detailed studies on the effect of calcination temperature were performed on samples synthesized in a reverse microemulsion of ϕ_w=0.12 at a water:alkoxide ratio 100 times the stoichiometric value. Figure 3.9 illustrates that increasing calcination temperature led to steady decrease in surface area. However, this system retained 112 m^2/g of average surface area even after calcination at 1300°C for 2 hours. The TEM particle size only increased slightly from 8 nm to 15 nm between 500°C and 1100°C. The most significant increase in particle size was noted at ~1100°C, whereby direct crystallization of amorphous oxides to the desired BHA phase occurred (as shown by XRD in Figure 3.10).

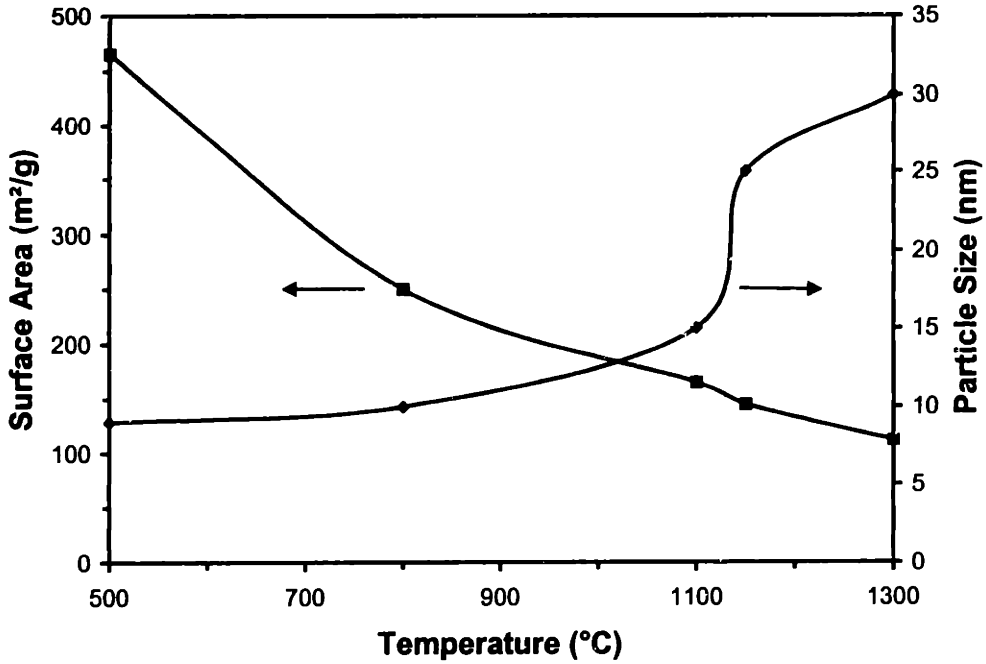

Figure 3.9. BET surface area and average TEM particle size as a function of calcination temperature for BHA materials synthesized in a reverse microemulsion of ϕ_w=0.12 at a water:alkoxide ratio 100 times the stoichiometric value, aged for 30 hours, recovered by freeze drying, and supercritically dried.

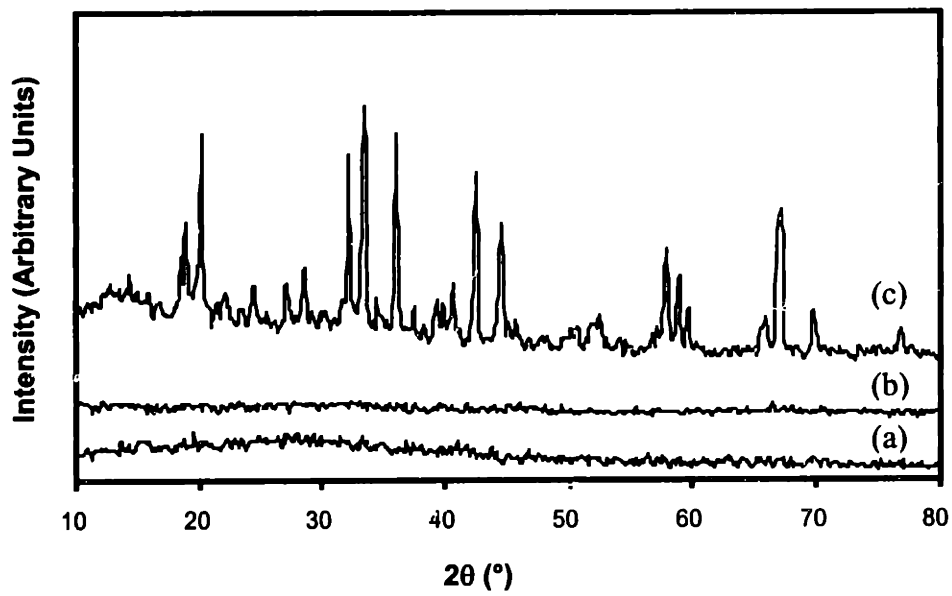

Figure 3.10. XRD patterns of samples aged for 24 hours in a reverse microemulsion of ϕ_w=0.12, and calcined at (a) 500°C, (b) 800°C, and (c) 1100°C. All peaks noted corresponded to $BaO{\cdot}6Al_2O_3$.

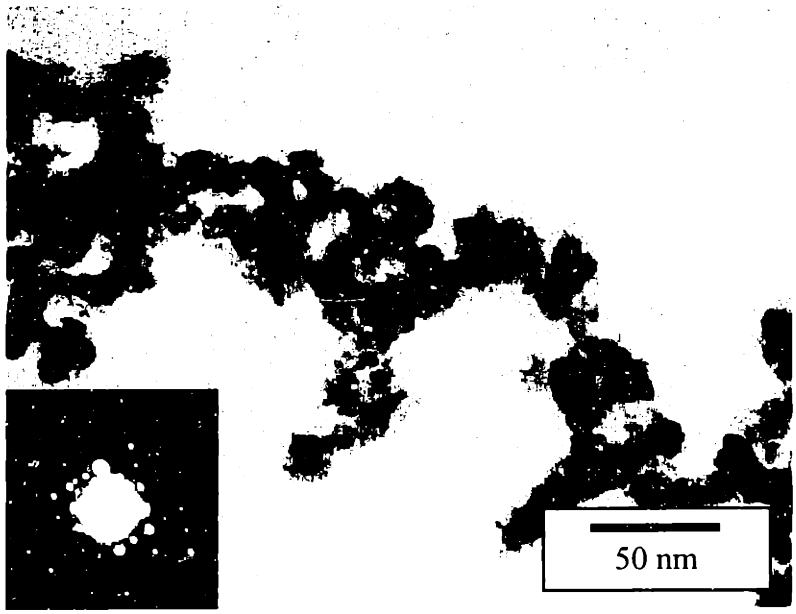

Figure 3.11. Transmission electron micrograph (200 kV) and electron diffraction pattern (inset) of reverse microemulsion derived BHA nanoparticles after calcination at 1300°C. The sample was synthesized in a reverse microemulsion of ϕ_w=0.12 at a water:alkoxide ratio 100 times the stoichiometric value, aged for 24 hours, recovered by freeze drying, and supercritically dried.

After crystallization, grain growth was suppressed even at high calcination temperatures, so that an ultrafine particle size of 30 nm was retained for this system at 1300°C (see Figure 3.11). The $BaO{\cdot}6Al_2O_3$ crystalline structure and chemical composition of these nanoparticles have been verified by XRD, electron diffraction (see inset of Figure 3.11), HR-TEM and elemental analysis studies. Structural evolution at the molecular level was investigated with PA-FTIR spectroscopy (Figure 3.12). The two broad low-frequency bands spanning 400-900 cm^{-1} arose from the phonon vibrations of metal oxides. An AlO-OH stretching band [13] was observed at ~1060 cm^{-1} (Figure 3.12(a)). This AlO-OH band disappeared upon calcination at 500°C, while two peaks emerged at 1370 and 1540 cm^{-1}, which might be attributed to overtone vibrations of metal oxides [14] (Figure 3.12(b)). The absorption at ~1640 cm^{-1} came from bending of molecular H_2O, and as expected, this mode was diminished with heat treatment. The broad band centered at 3400-3500 cm^{-1} was due to H_2O vibration; a substantial reduction of this hydrogen-bonded stretching band occurred between 1100 and 1300°C, reflecting the decrease in surface area at this temperature range. Corresponding to this heat

treatment was the formation of sharp peaks at 460, 500, 580, 770, 1005 and 1050 cm^{-1}, which might be assigned to the phonon vibrations of crystalline BHA.

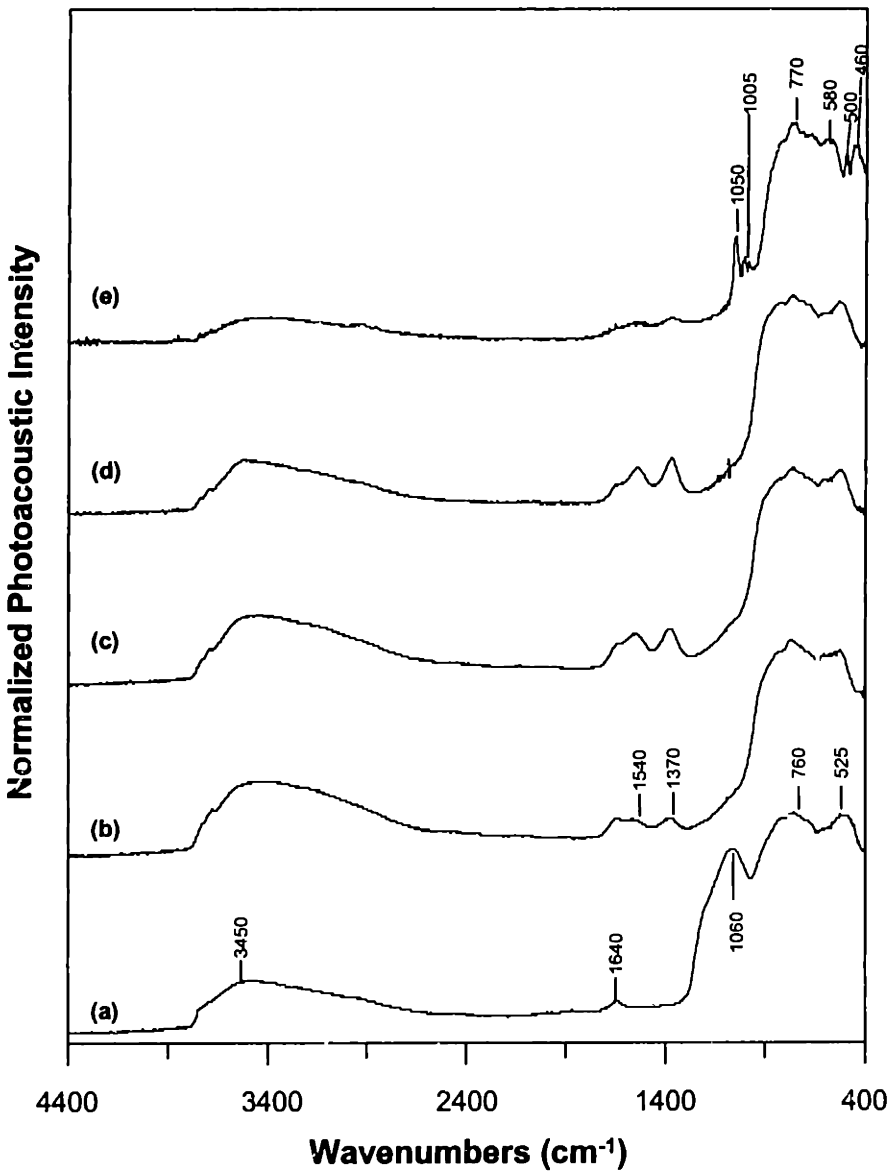

Figure 3.12. PA-FTIR spectra of samples aged for 24 hours in a reverse microemulsion of ϕ_w=0.12, recovered by filtration, and calcined at (a) 200°C, (b) 500°C, (c) 800°C, (d) 1100°C, and (e) 1300°C.

To illustrate the crystallization of BHA systems at elevated temperatures, we have conducted DTA studies in flowing air with a ramping rate of 20°C/min. Figure 3.13 showed that the samples derived by reverse microemulsion-mediated synthesis gave rise to exotherms at lower temperatures than the sample prepared by conventional sol-gel

processing. This is in good agreement with the XRD results that indicated lower temperatures of crystallization for the former.

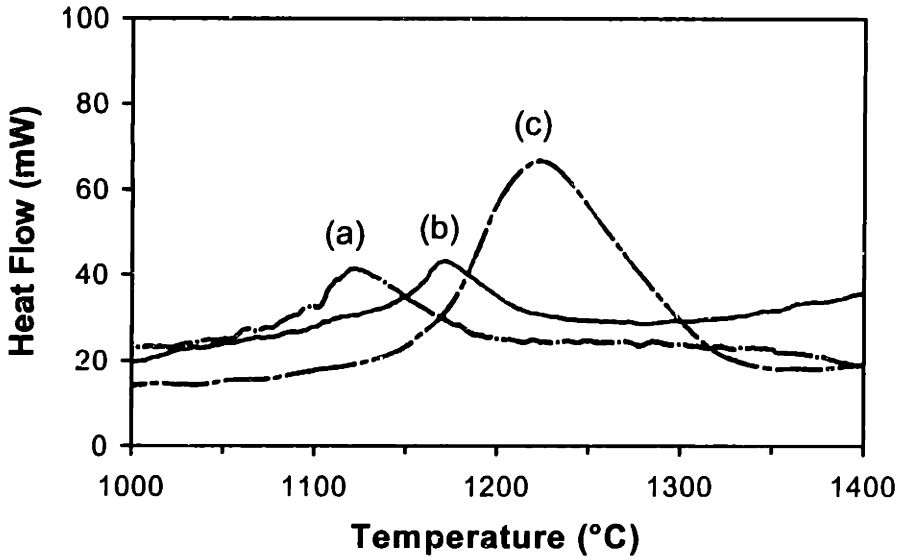

Figure 3.13. Differential thermal analysis (DTA) curves indicating the transformation from amorphous barium and aluminum oxides to BHA for samples synthesized in a reverse microemulsion of ϕ_w=0.12 at a water:alkoxide ratio 100 times the stoichiometric value, aged for (a) 48 hours or (b) 24 hours, recovered by filtration and oven dried. (c) DTA curve of sample prepared by conventional sol-gel processing, recovered by filtration and oven dried. Ramping rate: 20°C/min.

For a quantitative analysis of the energetic barrier in the phase transformation from amorphous barium and aluminum oxides to BHA, DTA studies were performed at various ramping rates (1-20 °C/min). The activation energy of the phase transformation (E_a) was then obtained with the Kissinger analysis [15], using the relationship between the ramping rate (φ) and the exothermic peak temperature (T_m or temperature of maximum deflection):

$$1/T_m = \ln(\varphi/A) - (E_a/R) \ln(\varphi/T_m^2), \qquad (3.3)$$

where A is an arbitrary frequency factor and R is the universal gas constant.

We determined the activation energy for crystallization to be as low as 544 kJ/mol for the reverse microemulsion derived sample that had been aged for 48 hours (Table 3.2). As discussed earlier, an aging period of 48 hours allowed for more complete condensation, so that the resulting material would undergo crystallization at a lower temperature than a sample that had been aged for 24 hours. The sample derived by

conventional sol-gel processing required a significantly higher activation energy for transformation to the desired BHA phase than the samples produced via reverse microemulsion-mediated sol-gel synthesis. The former did not undergo full crystallization to the BHA phase until a higher temperature of 1300°C, and possessed a coarsened grain size of > 100 nm upon such heat treatment. In contrast, by providing for improved chemical homogeneity and controlled microstructure, the reverse microemulsion-mediated synthesis allowed for facilitated crystallization and enhanced thermal stability to be achieved for the nanostructured BHA system.

Table 3.2. Activation energy of barium hexaaluminate crystallization for materials synthesized under different conditions.

Synthesis Approach	Aging Time (hour)	Activation Energy (kJ/mol)
Reverse Microemulsion‡	24	585
Reverse Microemulsion‡	48	544
Sol-Gel Processing*	24	620

‡Samples were synthesized in a reverse microemulsion of ϕ_w=0.12 at a water:alkoxide ratio 100 times the stoichiometric value, followed by aging for 24 or 48 hours. They were then recovered by filtration prior to calcination.
*Sol-gel derived sample was synthesized at a water:alkoxide ratio 100 times the stoichiometric value and recovered by filtration prior to calcination.

3.4 Summary

Nanometer-sized barium hexaaluminate particles have been prepared by reverse microemulsion-mediated sol-gel processing. The complex oxides obtained by this approach showed significant improvements in thermal stability and increased surface areas compared to conventional sol-gel derived materials.

Systematic studies of the synthesis parameters, such as water content in the reverse microemulsion and water:alkoxide ratio, enabled us to maintain a stable reaction mixture in the reverse microemulsion medium over extended aging periods. Aging was necessary for full condensation of the hydroxyl species, which was critical towards achieving a thermally stable, discrete particle morphology. However, extended aging (> 48 hours) would lead to the formation of an undesired barium carbonate phase.

Powder recovery and drying proved to be challenging in the processing of nanoparticles synthesized by the reverse microemulsion-mediated route. However, we have found that BHA nanoparticles could be effectively recovered by freeze drying and purified by supercritical drying without significant agglomeration. Consequently, a discrete particle morphology and a robust interparticle mesoporous structure could be maintained at temperatures as high as 1300°C.

The optimized synthesis parameters and processing conditions that have been established in this study allowed us to derive chemically homogeneous materials with the desired BHA crystalline phase at a relatively low crystallization temperature of 1050°C. The resulting nanoparticles were successfully suppressed in grain growth, yielding materials with exceptional surface areas and sintering resistance. BHA materials synthesized through this technique are highly attractive as catalysts and catalytic supports for high-temperature applications.

3.5 References

[1] M. Machida, K. Eguchi, H. Arai, *J. Catal.* **120**, 377 (1989).

[2] Y. Moriya, K. Nakagawa, K. Kawasaki, Y. Ozaki, *J. Ceram. Soc. Jpn.* **103**, 570 (1995).

[3] T. Narita, K. Nakagawa, K. Kawasaki, Y. Ozaki, *J. Ceram. Soc. Jpn.* **104**, 644 (1996).

[4] V. Chhabra, P. Ayyub, S. Chattopadhyay, A. N. Maitra, *Mater. Lett.* **26**, 21 (1996).

[5] Y. Khmelnitsky, A. Kabanov, N. Klyachko, A. Levashov, K. Martinek, "Structure and Reactivity in Reverse Micelles." Elsevier, Amsterdam, 1989.

[6] I. Lisieki, F. Billoudet, M. P. Pileni, *J. Molec. Liq.* **72**, 251 (1997).

[7] A. J. Zarur, H. H. Hwu, J. Y. Ying, *Langmuir,* in press.

[8] A. J. Zarur, H. H. Hwu, J. Y. Ying, submitted to *J. Catal.*.

[9] J. Y. Ying, A. J. Zarur, A. T. Heibel, T. Sun, U.S. Patent Pending, 1997.

[10] S. J. Gregg, K. S. W. Sing, "Adsorption, Surface Area and Porosity," 2nd ed. Academic Press, New York, 1982.

[11] J.-G. Park, A. N. Cormack, *J. Sol. St. Chem.* **121**, 278 (1996).

[12] J. D. Hopwood, S. Mann, *Chem. Mater.* **9**, 1819 (1997).

[13] J. B. Benziger, S. J. McGovern, B. S. H. Royce, *in* "Catalyst Characterization Science," (M. L. Deviney, J. L. Gland, Eds.), ACS Symposium Series No. 288. American Chemical Society, Washington, D.C., 1985.

[14] "The Sadtler Infrared Standard Spectra," Reports No. Y18, Y23, Y27, Y28, Y172, Y188, Y376. Sadtler Research Laboratories, Philadelphia, PA, 1974.

[15] H. E. Kissinger, *Anal. Chem.* **29**, 1702 (1957).

Chapter 4. Modified Barium Hexaaluminate Nanoparticles for Catalytic Combustion of Methane

4.1 Introduction

The reverse microemulsion-mediated sol-gel processing described in Chapter 3 yielded BHA materials with exceptional thermal stability [1,2]. This chapter focuses on the development of BHA-based systems for catalytic combustion. Mn and Ce were introduced in the form of structural dopants or surface oxide coatings during the hydrolysis and aging, respectively, of BHA in the reverse microemulsion medium. The active species were also impregnated as surface deposits onto the BHA supports after the nanoparticles have been recovered from the reverse microemulsion and crystallized via calcination. The enhancements in the methane combustion light-off behavior of the resulting modified BHA catalysts were related to the structural characteristics of these novel materials.

4.2 Experimental

Barium hexaaluminate nanoparticles were synthesized in a reverse microemulsion of ϕ_w=0.12 at a water:alkoxide ratio 100 times the stoichiometric value (Chapter 3) [1]. For the preparation of metal-doped BHA systems, manganese nitrate or cerium nitrate was added to the water to be used in the preparation of reverse microemulsion prior to hydrolysis of the barium and aluminum alkoxides. The amounts of manganese or cerium precursor were adjusted to accommodate the desired levels of dopants in the BHA samples. Systems with nanocrystalline coatings of MnO_2 or CeO_2 were prepared by adding the desired amount of manganese nitrate or cerium nitrate to the reverse microemulsion containing BHA nanoparticles during the aging process. The nitrate salts were introduced 12 h after the hydrolysis of Ba and Al alkoxides, and the system was then aged for another 12 h. For the purpose of comparison, MnO_2 and CeO_2 were deposited onto BHA nanoparticles via impregnation with nitrate salts, followed by air oxidation. This impregnation method has been applied by Machida *et al.* [3,4] to introduce Mn_3O_4 onto sol-gel derived BHA. In our study, the reverse microemulsion derived BHA nanoparticles were recovered and calcined at 1300°C, dispersed in de-

oxygenated H_2O, and sonicated for 5 min. The desired amounts of manganese nitrate or cerium nitrate were then added to the nanoparticulate dispersion with stirring. The impregnated system was heated to 70°C, with oxygen bubbling for 4 h to promote oxidation of the manganese or cerium salt on the BHA nanoparticles. The impregnated powders were recovered by filtration, air dried, and calcined at 800°C.

The microstructure of the resulting materials was investigated by high-resolution transmission electron microscopy (HR-TEM) using a JEOL 2010-FX microscope equipped with a high-performance X-ray detector for energy-dispersive X-ray (EDX) spectroscopy. The crystailine structure of the materials was characterized with powder X-ray diffraction (XRD) using a Siemens D5000 θ-θ diffractometer (45 kV, 40 mA, CuK_α), or a Rigaku rotating anode X-ray generator (18 kW, copper anode) coupled to a Rigaku 180-mm diffractometer with graphite diffracted beam monochromator. XRD grain sizes of $BaO{\cdot}6Al_2O_3$, MnO_2, and CeO_2 were determined from peak broadening analysis of their (114), (101), and (111) diffractions, respectively, using Scherrer's method, corrected for instrumental line broadening. Selected XRD patterns were refined by the Rietveld method using the LHPM computer algorithm [5]. The oxidation states of Mn and Ce dopants, surface coatings or deposits were examined with X-ray photoelectron spectroscopy (XPS) using a Physical Electronics 5200C spectrometer. The Brunauer-Emmett-Teller (BET) [6] surface area of various samples was determined through nitrogen adsorption with a Micromeritics ASAP 2010 analyzer; the pore size distribution of the materials was obtained from their N_2 desorption isotherm using the Barrett-Joyner-Halenda (BJH) method. Elemental analyses were attained by proton-induced X-ray emissions (PIXE) (Elemental Analysis Co., Lexington, KY), or inductively coupled plasma - atomic emissions spectroscopy (ICP-AES) using a Perkin-Elmer Plasma 40 analyzer.

The catalytic activity and kinetic behavior of the different materials were evaluated in a plug flow, packed bed reactor coupled to a Hewlett-Packard 6890 gas chromatograph with a Hewlett Packard 5972 mass selective detector (GC-MS). The reactor was kept under isothermal conditions using a three-zone tube furnace. Flow rates were controlled with MKS mass flow controllers. Light-off behavior of the catalysts was characterized under isothermal conditions for a stream of 1 vol% CH_4 in air. Kinetic

parameters were evaluated by mixing methane, oxygen and helium at methane:oxygen molar ratios varying from 1:100 to 1:2 (stoichiometric), and reacting them over the catalyst bed under isothermal conditions. Temperature-programmed desorption (TPD) studies were conducted under a He atmosphere at a ramp rate of 3°C/min in a flow reactor coupled to a GC-MS.

4.3 Results and Discussion

4.3.1 Structural Characterization

4.3.1.1 Mn- and Ce-Doped BHA Nanoparticles

The crystalline structure of Mn-doped BHA was examined by XRD, and the lattice parameters were obtained for samples with different Mn dopant concentrations via Rietveld refinement. Significant distortion of the BHA unit cell was observed at dopant levels of ≥ 1.88 at%. The lattice parameters *a* and *c* increased with increasing Mn dopant level up to 11.25 at% (Figure 4.1), as reflected by peak shifts to the lower 2θ angles (Figure 4.2). The expansion in the $BaO{\cdot}6Al_2O_3$ unit cell with Mn doping could be attributed to the substitution of Mn for Al in the BHA structure. For a sample with 11.25 at% Mn, a separate $MnAl_2O_4$ phase was observed in the XRD pattern after calcination to ≥ 800°C (Figure 4.2(d)). It was interesting to note that for BHA samples with ≤ 3.75 at% Mn, the XRD patterns consisted of strong peaks corresponding to $BaO{\cdot}6Al_2O_3$ and weaker peaks corresponding to $BaO{\cdot}6.6Al_2O_3$ (Figures 4.2(a)-(b)). The peaks corresponding to $BaO{\cdot}6.6Al_2O_3$ disappeared with increased Mn loading, as noted for the samples containing 7.50 and 11.25 at% Mn (Figures 4.2(c)-(d)). With increasing Mn loadings, the BET surface areas (Figure 4.3) decreased, and the BHA XRD grain sizes increased for the 1300°C-calcined samples (Table 4.1). The sample with 11.25 at% Mn lost most of its surface area and underwent significant grain coarsening to > 40 nm by 1300°C (Table 4.1), possibly due to the lower thermal stability of the $MnAl_2O_4$ phase present. For samples with < 11.25 at% Mn, TEM studies showed that the microstructure of BHA was not significantly affected by Mn doping, and EDX mapping illustrated a uniform dispersion of Mn within the BHA particles.

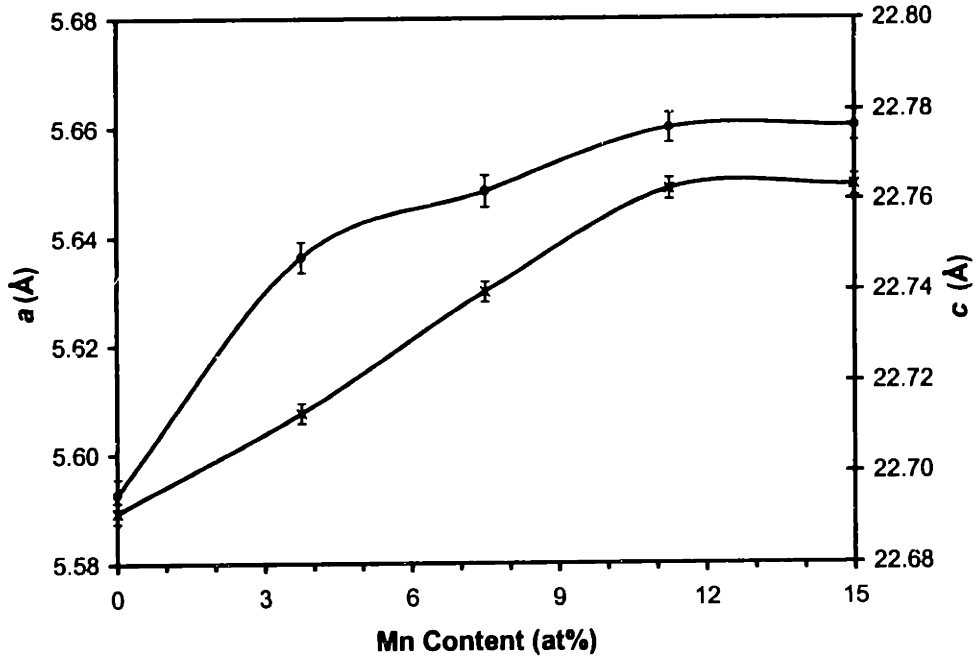

Figure 4.1. *a* and *c* lattice parameters in the $BaO{\cdot}6Al_2O_3$ unit cell of 1300°C-calcined doped BHA samples with different Mn loadings.

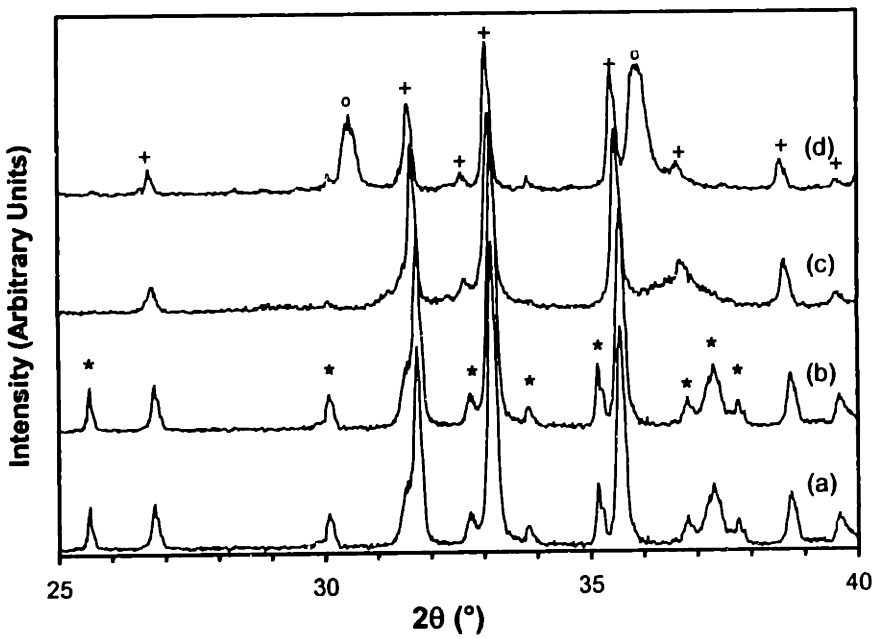

Figure 4.2. XRD patterns of 1300°C-calcined doped BHA samples with (a) 1.88 at% Mn, (b) 3.75 at% Mn, (c) 7.50 at% Mn, and (d) 11.25 at% Mn. $BaO{\cdot}6Al_2O_3$ peaks, $BaO{\cdot}6.6Al_2O_3$ peaks, and $MnAl_2O_4$ peaks are marked +, ★, and o, respectively.

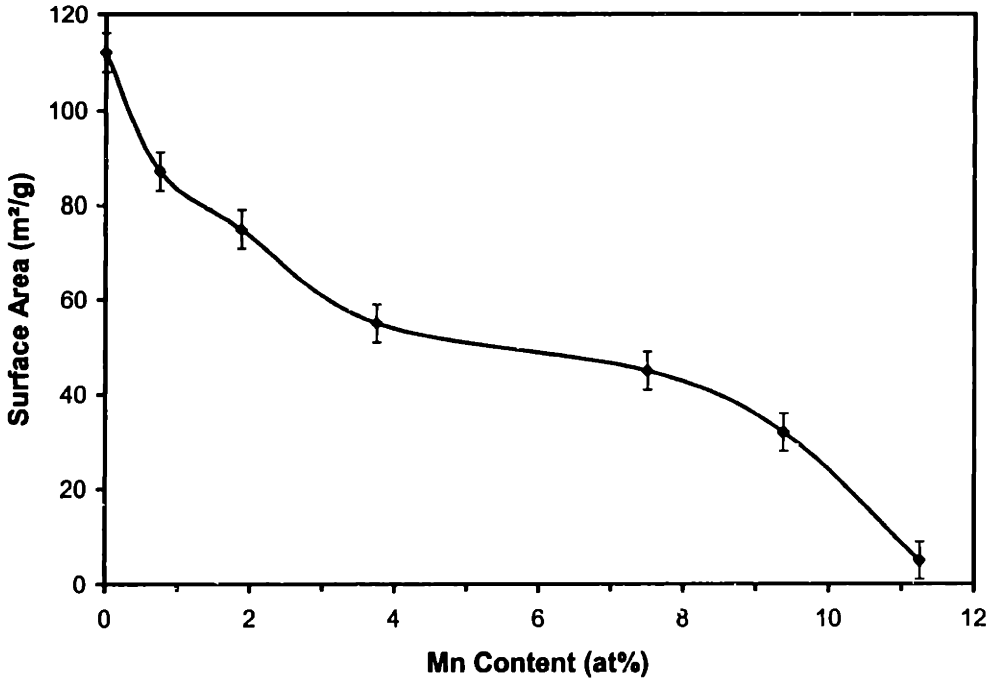

Figure 4.3. BET surface areas of 1300°C-calcined doped BHA samples with different Mn loadings.

Table 4.1. Characteristics of Mn-doped BHA nanoparticles.

at% Mn	Surface Area (m^2/g)		BHA Grain Size (nm)	XRD Crystalline Phase	Light-off Temperature
	800°C	1300°C	@ 1300°C	@ 1300°C	(°C)
1.88	250	78	18	$BaO{\cdot}6Al_2O_3 + BaO{\cdot}6.6Al_2O_3$	550
3.75	238	56	25	$BaO{\cdot}6Al_2O_3 + BaO{\cdot}6.6Al_2O_3$	500
7.50	219	45	> 30	$BaO{\cdot}6Al_2O_3$	500
11.25	189	5	> 40	$BaO{\cdot}6Al_2O_3 + MnAl_2O_4$	505

In addition to Mn dopants, we have attempted to introduce Ce dopants into the BHA structure by dissolving cerium nitrate in the aqueous domains of the reverse microemulsion used in the mediated hydrolysis of Ba and Al alkoxides. However, Ce could not be substituted into the BHA crystalline structure, as reflected by the unchanged BHA lattice parameters even at a high Ce loading of 2 at%. Additionally, a separate CeO_2 (cerianite) phase was noted in the Ce-containing samples after calcination at 400°C. CeO_2 peaks were observed along with $BaO{\cdot}6Al_2O_3$ peaks in the XRD patterns of 1300°C-calcined samples, even when the Ce dopant concentration was only 0.5 at%

(Figure 4.4(a)). The CeO_2 peaks became dominant in the XRD pattern of samples doped with ≥ 2 at% Ce. This study indicated that Ce was not substituting for Ba cations in the BHA structure, possibly due to the large difference in the ionic radii of Ce^{+4} (1.01 Å) and Ba^{+2} (1.49 Å), and the inability of Ce to adopt an oxidation state of +2. TEM showed that both pure and 2 at% Ce-doped BHA consisted of hexagonally-shaped particles (Figure 4.5). However, the latter consisted of amorphous particles except for the CeO_2 crystallites. Table 4.2 presents the thermal evolution of Ce-doped BHA samples, showing that substantial surface areas (> 230 m^2/g) were retained at 800°C even for systems with high Ce loadings. Figure 4.6 further illustrates that grain growth of CeO_2 was suppressed substantially when supported on BHA. Upon calcination at 1100°C, 2 at% Ce-doped BHA retained an ultrafine CeO_2 crystallite size of 25 nm. Major CeO_2 grain growth and loss of overall surface area occurred between 1100°C and 1300°C.

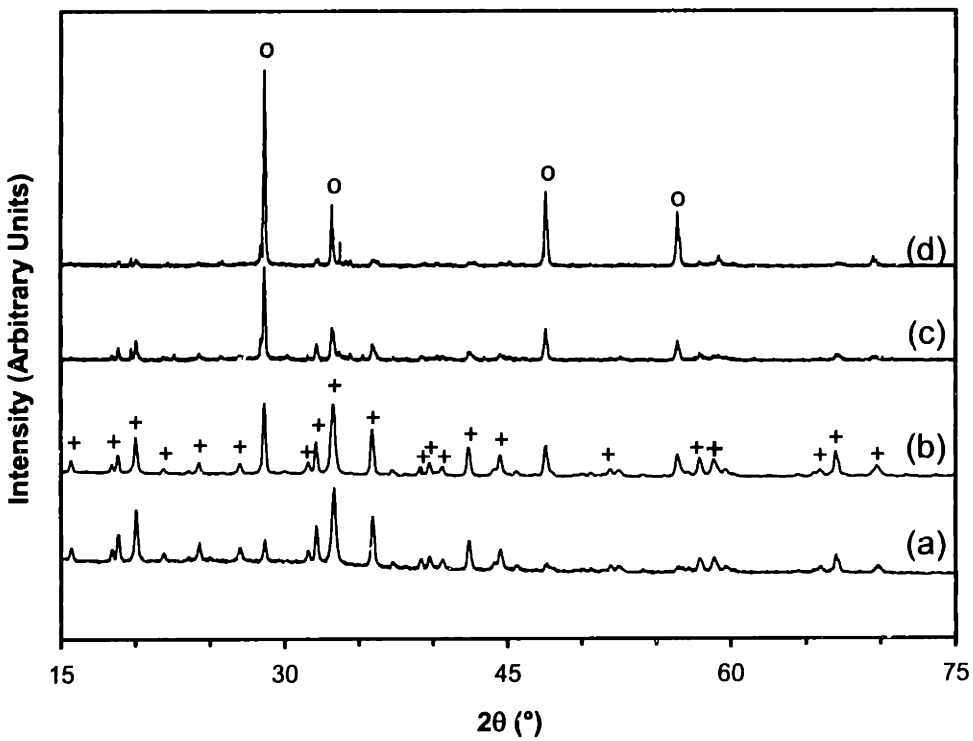

Figure 4.4. XRD patterns of 1300°C-calcined doped BHA samples with (a) 0.5 at% Ce, (b) 1.0 at% Ce, (c) 2.0 at% Ce, and (d) 3.0 at% Ce. $BaO{\cdot}6Al_2O_3$ peaks and CeO_2 peaks are marked **+** and **o**, respectively.

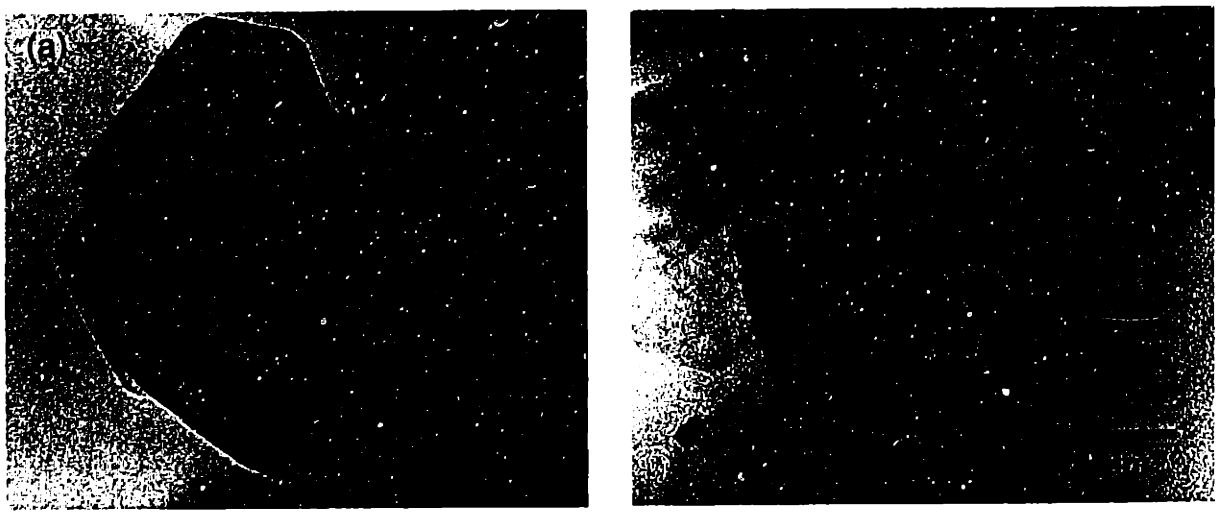

Figure 4.5. Transmission electron micrographs of (a) pure BHA and (b) 2 at% Ce-doped BHA, after calcination at 1300°C.

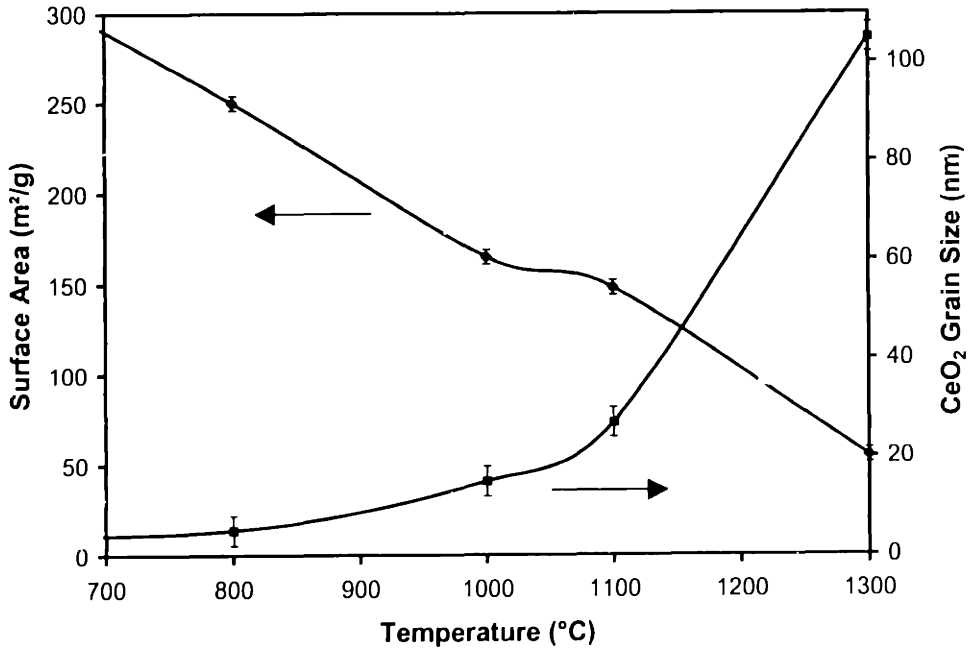

Figure 4.6. BET surface areas and CeO_2 XRD grain sizes as a function of calcination temperature for 2 at% Ce-doped BHA.

Table 4.2. Characteristics of Ce-doped BHA nanoparticles.

at% Ce	Surface Area (m^2/g)		BHA Grain Size (nm)	XRD Crystalline Phase	Light-off Temperature
	800°C	1300°C	@ 1300°C	@ 1300°C	(°C)
0.5	255	65	17	$BaO{\cdot}6Al_2O_3 + CeO_2$	550
1.0	241	49	> 40	$BaO{\cdot}6Al_2O_3 + CeO_2$	500
2.0	239	27	N/A	$BaO{\cdot}6Al_2O_3 + CeO_2$	465
3.0	253	20	N/A	$BaO{\cdot}6Al_2O_3 + CeO_2$	475

The oxidation states of Mn and Ce cations in the doped BHA samples were investigated by XPS. We found that Ce existed in the +4 oxidation state regardless of dopant level or calcination temperature. In contrast, Mn was found to assume mixed oxidation states of +3 and +4, depending on the dopant level. At a dopant concentration of 1.88 at%, Mn had a mixed valence averaging +3.4. The oxidation states of Mn were +3.6 and +3.7 for the samples with 3.75 and 7.50 at% Mn, respectively. An average oxidation state of +3.4 was assumed by Mn in the sample consisting of 11.25 at% Mn; the lower Mn valence in this material could be attributed to the presence of the $MnAl_2O_4$ phase (whereby Mn assumed a valence of +2), in addition to the doped $BaO{\cdot}6Al_2O_3$ phase.

4.3.1.2 MnO_2- and CeO_2-Coated BHA Nanoparticles

Active metal oxides could be introduced with ultrahigh dispersion onto the surface of BHA nanoparticles during their aging in the reverse microemulsion medium. Introduction of surface oxides did not affect the hexagonal morphology of BHA particles, which was preserved after powder recovery.

The samples coated with various levels of manganese oxides all showed XRD diffraction peaks corresponding to MnO_2 after heat treatment at 800°C. The presence of the MnO_2 coatings retarded the crystallization of BHA nanoparticles. $BaO{\cdot}6Al_2O_3$ peaks were noted in the XRD patterns of the samples with > 1.0 at% Mn only after heat treatment at > 1175°C; whereas pure BHA nanoparticles were crystallized by 1050°C.

Table 4.3 shows that the BHA sample coated with 2.5 at% Mn retained the highest surface area (49 m^2/g) and the finest MnO_2 crystallite size (25 nm) at 1300°C. The sample with 7.5 at% Mn had surface areas as high as 476 and 145 m^2/g at 800 and 1100°C, respectively, but retained only 35 m^2/g of surface area after calcination at 1300°C (Figure 4.7). The loss of surface area was accompanied by severe grain growth of the MnO_2 phase. The MnO_2 crystals grew from 14 nm at 800°C to 70 nm at 1300°C. Figure 4.8(b) shows a HR-TEM micrograph of 7.5 at% Mn-coated BHA particles after calcination at 800°C. The MnO_2-coated BHA samples all retained excellent surface areas (253-487 m^2/g) after calcination at 800°C (Table 4.3), making them particularly attractive for mid-temperature catalytic combustion applications. The oxidation state of Mn in coated samples was found to be +4 by XPS, regardless of loading.

For nanoparticles coated with CeO_2, crystallization of the $BaO{\cdot}6Al_2O_3$ phase was inhibited by the introduction of ≥ 2.0 at% Ce. No $BaO{\cdot}6Al_2O_3$ diffraction peaks were observed in the XRD patterns of these samples even after calcination at 1500°C. On the other hand, peaks corresponding to CeO_2 were found in all CeO_2-coated BHA samples after calcination at 400°C. CeO_2 XRD grain size was calculated to be < 7 nm after heat treatment at 500°C. For samples containing 3.0 at% Ce, CeO_2 crystallites of ~8 and 24 nm were obtained after calcination at 800 and 1300°C, respectively (Figure 4.9, Table 4.4). In contrast, unsupported nanocrystalline CeO_2 synthesized by controlled chemical precipitation would have undergone significant grain growth to > 100 nm by 800°C [7].

Table 4.3. Characteristics of MnO_2-coated BHA nanoparticles.

at% Mn	Surface Area (m^2/g)		MnO_2 Grain Size (nm)		XRD Crystalline Phase @ 1300°C	Light-off Temperature (°C)
	800°C	1300°C	800°C	1300°C		
2.5	487	49	12	25	$BaO{\cdot}6Al_2O_3 + MnO_2$	440
5.0	425	42	8	30	$BaO{\cdot}6Al_2O_3 + MnO_2$	405
7.5	476	35	14	70	$BaO{\cdot}6Al_2O_3 + MnO_2$	395
10.0	253	33	25	> 100	$BaO{\cdot}6Al_2O_3 + MnO_2$	415

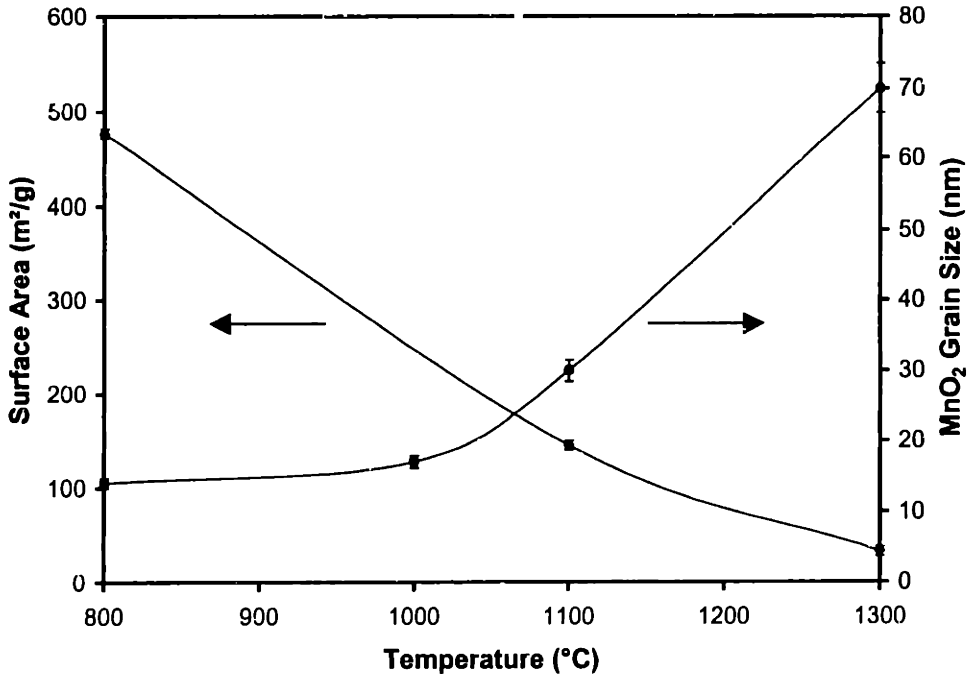

Figure 4.7. BET surface areas and MnO_2 XRD grain sizes as a function of calcination temperature for coated BHA nanoparticles with 7.5 at% Mn.

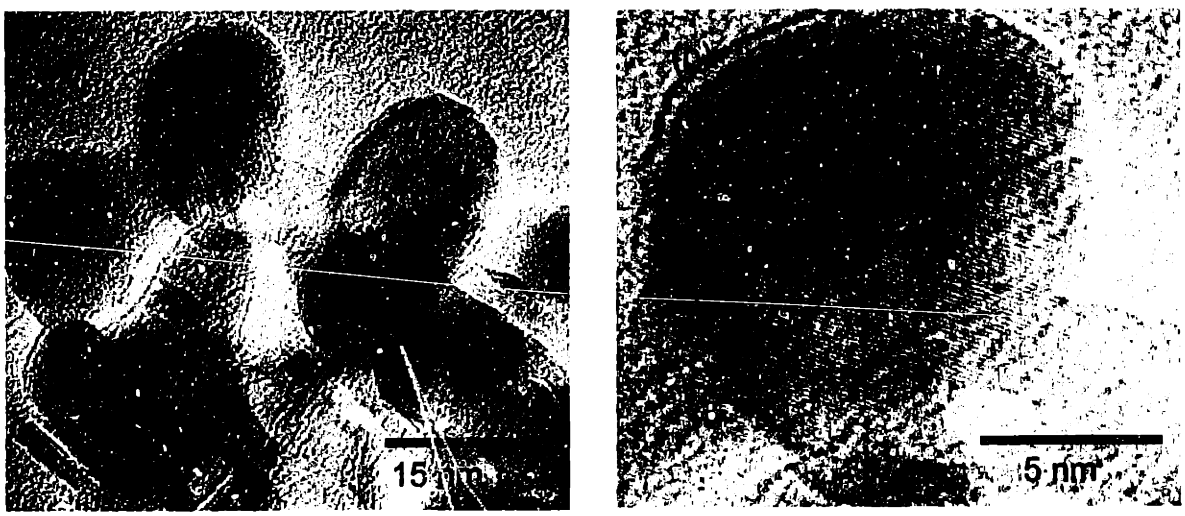

Figure 4.8. (a) Transmission electron micrograph and (b) high-resolution transmission electron micrograph of 800°C-calcined coated BHA particles with 7.5 at% Mn.

Excellent surface areas were preserved by samples with ≤ 4.0 at% Ce after calcination at 1300°C. The surface area of the coated BHA sample with 3.0 at% Ce decreased significantly between 500°C (~500 m^2/g) and 1100°C (90 m^2/g); reduction in surface area with heat treatment was gradual thereafter, and 60 m^2/g was retained at

1300°C (Figure 4.9). Unlike the MnO_2-coated BHA particles (Figure 4.8), the CeO_2-coated BHA particles retained a discrete, non-agglomerated particle morphology even at elevated temperatures (see Figure 4.10(a)). HR-TEM micrograph in Figure 4.10(b) illustrates the presence of highly dispersed CeO_2 nanocrystallites on the surface of spherical, amorphous BHA nanoparticles for the system containing 3.0 at% Ce.

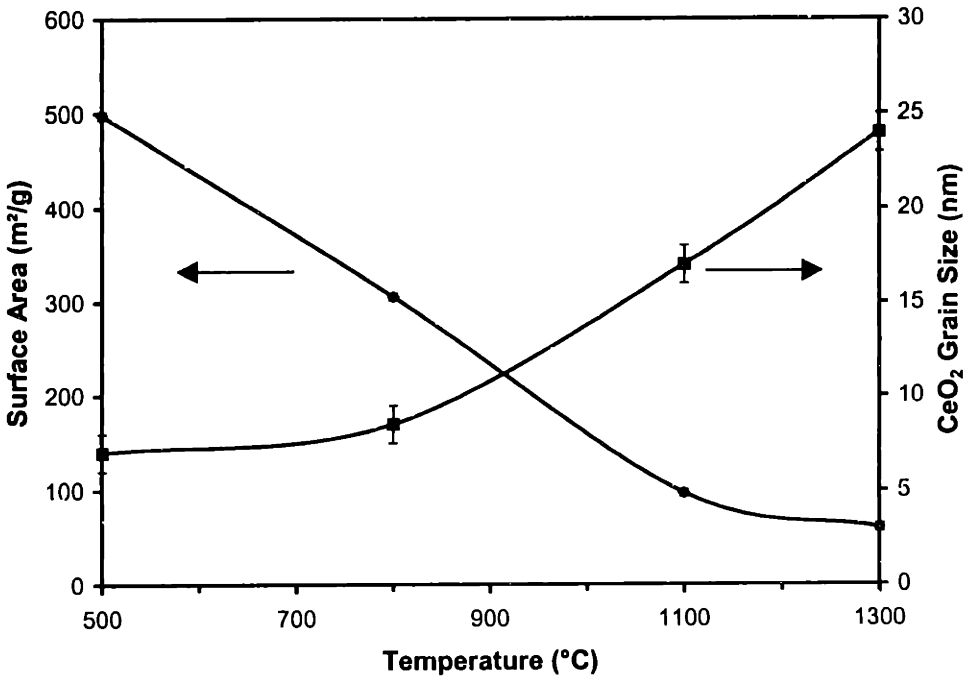

Figure 4.9. BET surface areas and CeO_2 XRD grain sizes as a function of calcination temperature for coated BHA nanoparticles with 3.0 at% Ce.

Table 4.4. Characteristics of CeO_2-coated BHA nanoparticles.

at% Ce	Surface Area (m^2/g)		CeO_2 Grain Size (nm)		XRD Crystalline Phase @ 1300°C	Light-off Temperature (°C)
	800°C	1300°C	800°C	1300°C		
1.0	320	79	5	24	$BaO{\cdot}6Al_2O_3 + CeO_2$	460
2.0	313	65	7	25	CeO_2	450
3.0	306	60	8	24	CeO_2	410
4.0	290	56	12	> 30	CeO_2	425

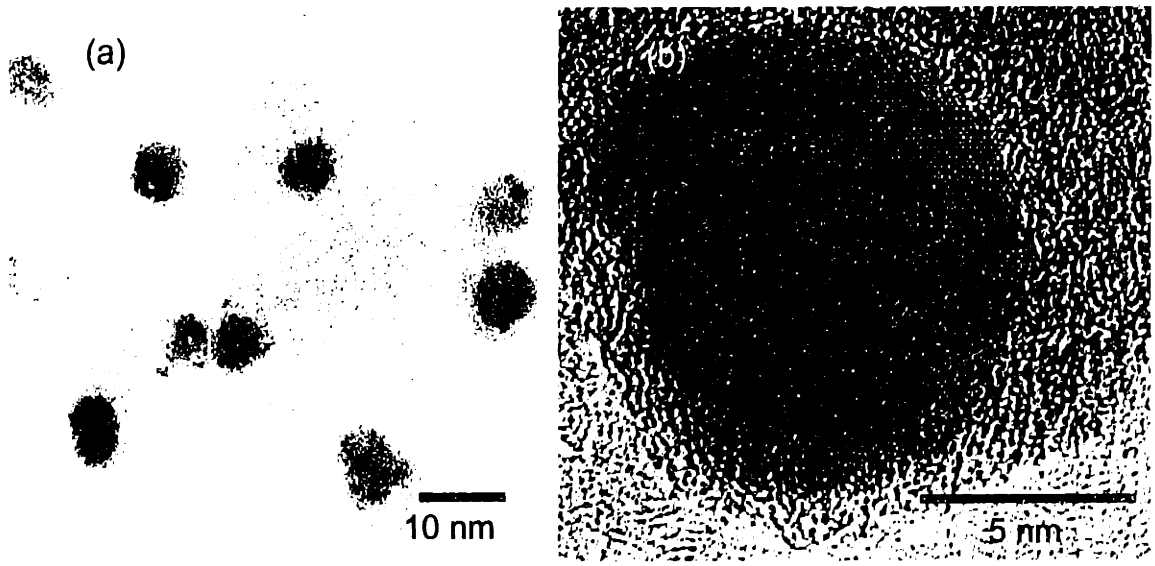

Figure 4.10. (a) Transmission electron micrograph and (b) high-resolution transmission electron micrograph of 800°C-calcined coated BHA particle(s) with 3.0 at% Ce.

The CeO_2-coated BHA showed enhanced thermal stability over the Ce-doped BHA samples. The coated sample with 3.0 at% Ce retained surface areas in excess of 300 m^2/g and ~60 m^2/g after calcination at 800°C and 1300°C, respectively. In contrast, 3.0 at% Ce-doped BHA retained 253 m^2/g and 20 m^2/g after the respective heat treatments. The CeO_2 grain size of the coated samples was also significantly smaller than that of Ce-doped samples. The coated sample with 3.0 at% Ce possessed CeO_2 grain sizes of 8 nm and 24 nm after calcination at 800°C and 1300°C, respectively. The 3.0 at% Ce-doped sample had CeO_2 grain sizes of 10 nm and > 100 nm after the respective heat treatments. The morphologies of the doped and coated BHA particles were also very different. The CeO_2-coated samples consisted of discrete or loosely agglomerated spherical particles of 5-15 nm after calcination at 800°C. The Ce-doped samples were composed of hexagonally-shaped particles with sizes ranging from 10 to 100 nm after calcination at 800°C; the hexagonal morphology of these particles was preserved upon calcination to 1300°C.

4.3.1.3 MnO_2- and CeO_2-Impregnated BHA Nanoparticles

Sol-gel derived BHA has been impregnated with MnO_x by Machida *et al.* [8]. Mn_3O_4 was found to be deposited with full coverage of the BHA surface at Mn

concentrations of > 2 at%. For BHA impregnated with < 10 at% Mn and calcined to 500°C, Machida *et al.* did not observe peaks corresponding to Mn_3O_4 or MnO_2 in the XRD patterns. In our studies, the BHA nanoparticles derived from the reverse microemulsion-mediated sol-gel processing were first calcined to 1300°C before they were impregnated with MnO_2, so these support materials possessed crystalline $BaO{\cdot}6Al_2O_3$ XRD peaks. EDX mapping showed uniform manganese dispersion on the surface of BHA nanoparticles after sample calcination at 500°C. Upon calcination to 800°C, our impregnated samples with > 5 at% Mn showed MnO_2 peaks in their XRD patterns. The MnO_2 XRD grain size was calculated to be > 30 nm. After heat treatment at 1100°C, MnO_2 diffraction peaks were noted for samples impregnated with > 2 at% Mn; the grain size for MnO_2 was > 100 nm. Along with severe grain growth, MnO_2 crystals were shown by HR-TEM to have become agglomerated and segregated from the BHA particles as a bulk phase. Distinct MnO_2 particles were observed in EDX imaging, and a much lower Mn concentration was detected on the surface of BHA particles due to phase separation. The overall surface area of these impregnated materials remained fairly high at elevated temperatures, especially for the samples with lower Mn contents. BHA samples impregnated with 5 and 10 at% Mn retained surface areas of 70 and 63 m^2/g, respectively, after calcination at 1100°C. Their surface areas decreased to ~30 m^2/g after heat treatment at 1300°C. BHA nanoparticles impregnated with MnO_2 by the conventional technique did not possess as high a thermal resistance as the BHA nanoparticles coated with MnO_2 during their aging in the reverse microemulsion medium. After calcination at 800°C, samples coated with up to 5 at% Mn retained surface areas in excess of 400 m^2/g and MnO_2 grain sizes of 8-12 nm. After calcination at 1300°C, the surface area of these coated BHA materials decreased to ~40 m^2/g and the MnO_2 grain size increased to ~30 nm. In contrast, impregnated samples had surface areas of ~150 m^2/g and ~30 m^2/g, and MnO_2 grain sizes of 17 nm and > 100 nm after calcination to 800°C and 1300°C, respectively. Figure 4.11(a) shows a TEM of BHA nanoparticles impregnated with 5 at% Mn and calcined to 800°C.

Figure 4.11. Transmission electron micrographs of BHA particles impregnated with (a) 5 at% Mn and (b) 2 at% Ce. The BHA nanoparticles were calcined at 1300°C prior to impregnation, and heat treated to 800°C after impregnation.

Impregnated samples with > 1 at% Ce showed crystalline CeO_2 peaks after calcination at 500°C. However, uniform CeO_2 coverage of BHA nanoparticles was not achieved by the impregnation technique. A mixture of CeO_2 and BHA particles, rather that CeO_2 deposits on BHA surface, was noted in the TEM studies of the impregnated materials. Grain growth of ceria occurred rapidly with heat treatment; for samples impregnated with > 1 at% Ce, CeO_2 grains became > 100 nm after calcination at 800°C. Unlike the CeO_2-coated BHA nanoparticles described earlier, the impregnated nanoparticles did not possess a high surface dispersion of CeO_2. Consequently, the CeO_2 component could not benefit from the excellent thermal resistance of the BHA support in the impregnated systems. Upon calcination at 1100°C, the materials impregnated with 2 and 4 at% Ce retained surface areas of 65 and 57 m^2/g, respectively. After heat treatment at 1300°C, the surface areas were reduced to < 30 m^2/g. Since the CeO_2 component had coarsened by 800°C, the surface areas of these systems after calcination at elevated temperatures were mainly associated with the thermally stable BHA particles. Figure 4.11(b) shows a TEM micrograph of BHA nanoparticles impregnated with 2 at% Ce and calcined to 800°C.

4.3.2 Catalytic Properties

4.3.2.1 Mn- and Ce-Doped BHA Nanoparticles

BHA samples doped with Mn or Ce were pre-treated to 1300°C prior to catalytic studies. Mn-doped BHA samples synthesized by reverse microemulsion-mediated processing (Table 4.1) showed enhanced catalytic activity over those synthesized by conventional sol-gel processing. BHA nanoparticles with 3.75 at% Mn dopants provided 10% methane conversion at 500°C for a stream of 1 vol% CH_4 in air flowing at 60,000 h^{-1}. In contrast, conventional sol-gel derived Mn-doped BHA would "light-off" at a higher temperature of 540-550°C [9]. These differences in catalytic activity could be attributed to the different surface areas of the two samples: the Mn-doped BHA nanoparticle retained 56 m^2/g after calcination at 1300°C, while the sol-gel derived sample possessed a surface area of only 15-20 m^2/g. Figure 4.12 illustrates the catalytic activity of various reverse microemulsion derived materials, showing that the introduction of Mn dopants substantially improved the catalytic activity of BHA, although the Mn-doped BHA nanoparticles have a lower overall surface area (56 m^2/g) than the pure BHA nanoparticles (> 100 m^2/g).

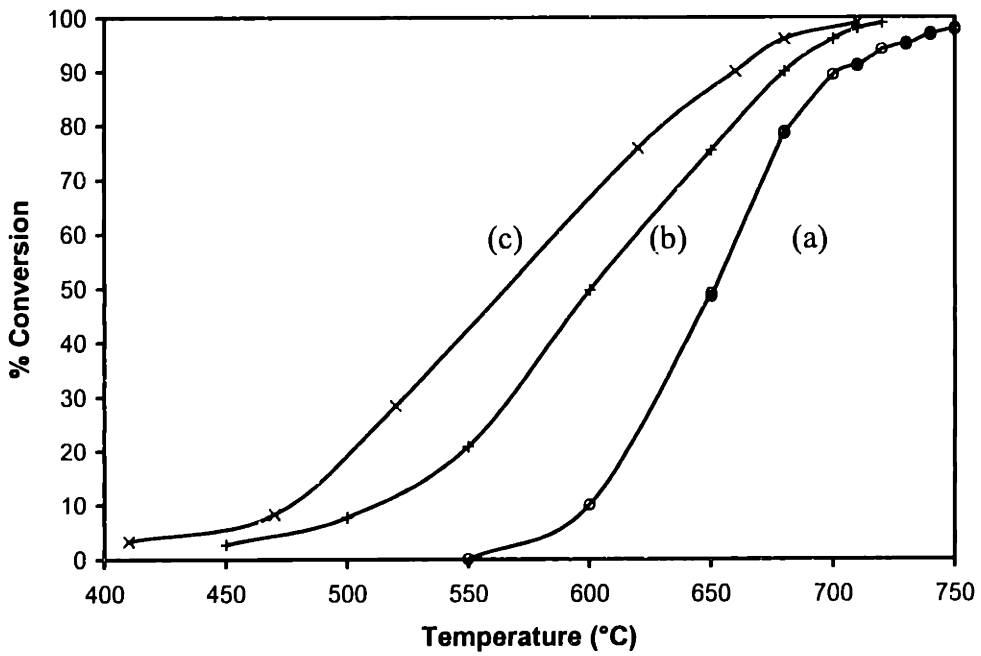

Figure 4.12. Methane oxidation over (a) pure BHA, (b) 3.75 at% Mn-doped BHA, and (c) 2.0 at% Ce-doped BHA. Feed: 1 vol% CH_4 in air, GSHV: 60,000 h^{-1}.

Introduction of Ce at a dopant level as low as 0.5 at% led to a significant enhancement in the catalytic properties of BHA (See Table 4.2). The sample with 2 at% Ce enabled CH_4 light-off at a low temperature of 465°C (Figure 4.12(c)). Higher Ce dopant levels (e.g. 3.0 at%) did not result in further improvement in the catalytic activity. This might be attributed to the lower surface dispersion of CeO_2 on BHA nanoparticles at the higher Ce loading levels.

4.3.2.2 MnO_2- and CeO_2-Coated BHA Nanoparticles

BHA samples coated with MnO_2 and CeO_2 were subjected to calcination at 800°C prior to catalytic studies. These materials had a superior low-temperature catalytic performance compared to the pure and doped BHA samples.

BHA coated with 7.5 at% Mn exhibited light-off at a remarkably low temperature of 395°C, achieving full conversion of a stream of 1 vol% CH_4 in air by ~600°C (Figure 4.13(b)). Catalytic activity of 800°C-calcined MnO_2-coated BHA nanoparticles was optimized with a Mn content of 5-7.5 at%, which corresponded to MnO_2 grain sizes < 15 nm and BET surface areas in excess of 400 m^2/g (See Table 4.3). Despite having comparable MnO_2 grain sizes and overall BET surface areas, materials with < 5 at% Mn required a higher light-off temperature, probably due to the lower concentration of MnO_2 surface sites. BHA samples with ≥ 10 at% Mn suffered slightly in catalytic activity as they possessed a lower surface area of < 260 m^2/g and coarser MnO_2 grains of ≥ 25 nm after calcination at 800°C.

BHA materials coated with nanocrystalline CeO_2 demonstrated a light-off temperature as low as 410°C, with full CH_4 conversion accomplished by ~600°C (Figure 4.13(c)). The microstructure of the CeO_2-coated materials had a significant influence on their catalytic activity. An ultrahigh dispersion of CeO_2 was found to be critical towards achieving low light-off temperatures. The optimal loading was found to be 3.0 at% Ce (see Table 4.4). At Ce loadings of < 3.0 at%, a higher light-off temperature was needed due to the lower concentration of surface active components. At loadings > 3.0 at%, catalytic activity was slightly reduced due to the lower CeO_2 dispersion (grain size > 10 nm).

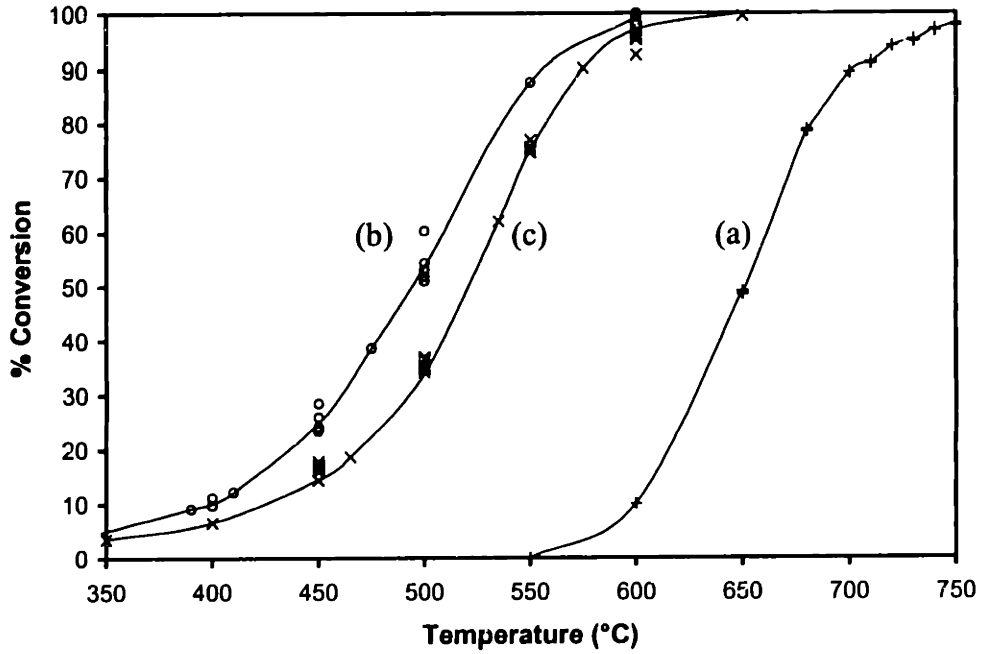

Figure 4.13. Methane oxidation over (a) pure BHA, and coated BHA containing (b) 7.5 at% Mn and (c) 3.0 at% Ce. Feed: 1 vol% CH_4 in air, GSHV: 60,000 h^{-1}.

The high-temperature catalytic stability of coated BHA nanoparticles was also investigated. The CeO_2-coated samples were active for methane combustion for extended periods in the presence of 10 vol% H_2O at temperatures ≤ 1100°C, without catalyst deactivation or hysteresis in catalytic behavior during heating-cooling-restarting cycles. The excellent catalytic stability could be attributed to the superb thermal resistance of the CeO_2-coated BHA samples, which retained impressive surface areas and ultrafine CeO_2 grain sizes even after calcination at 1300°C (see Table 4.4). Samples coated with MnO_2, on the other hand, deactivated after exposure to 1100°C in the presence of water vapor due to significant grain growth and loss of MnO_2. As high as 5% of the Mn loaded could be vaporized at 1100°C for a sample originally coated with 7.5 at% Mn. The light-off temperatures were ~395°C and 460°C for 7.5 at% Mn-coated BHA nanoparticles in the first heating cycle and in the cooling-restarting cycle, respectively. The hysteresis in catalytic performance could be attributed to the decrease in MnO_2 dispersion and loading under combustion reaction conditions at 1100°C. There was no hysteresis in catalytic behavior for BHA nanoparticles coated with 2.5-7.5 at% Mn subjected to ≤ 1000°C.

4.3.2.3 MnO_2- and CeO_2-Impregnated BHA Nanoparticles

The catalytic activity of MnO_2-impregnated BHA samples was found to vary significantly with the post-impregnation calcination temperature. After heated at 600°C, BHA impregnated with 5 at% Mn has a light-off temperature of 420-425°C for 1 vol% CH_4 in air. When heat treated to 800°C, the sample's light-off temperature was increased to 450-475°C. The catalytic activity of the material significantly decreased when calcined to 1100°C due to significant MnO_2 grain growth and loss of surface area; the sample required a light-off temperature higher than 550°C.

BHA catalysts impregnated with CeO_2 were much less active than those coated with CeO_2 nanocrystals. For 3 at% Ce-impregnated BHA sample that had been calcined to 600°C, light-off was observed at 500-510°C. Treatment at higher temperatures resulted in reduced catalytic activity for the impregnated materials due to bulk phase segregation and grain growth of CeO_2. Light-off was not observed until 560°C when the impregnated sample was subjected to treatment at 800°C. After calcination above 1100°C, the catalytic activity of the CeO_2-impregnated BHA sample became similar to that of the pure BHA nanoparticles. In contrast, 3.0 at% Ce-coated BHA that had been calcined to 1100°C retained a remarkably low light-off temperature of 410°C due to its stable, ultrahigh CeO_2 dispersion.

4.3.2.4 Kinetic Studies of Mn- and Ce-Containing BHA Catalysts

The apparent rate orders for methane and oxygen over modified BHA catalysts were investigated under differential reaction conditions by systematically varying the concentration of one of the reactants, while keeping the concentration of the other reactant constant. The doped and coated BHA samples were subjected to calcination at 1300°C and 800°C, respectively, prior to the kinetic studies.

The reaction mechanism over these catalysts was found to be a function of reaction temperature, methane concentration, and oxygen concentration. For ultralean fuel mixtures (corresponding to methane:oxygen molar ratios of 1:100 to 1:20), we found that the apparent reaction orders were 1 and ½ for methane and oxygen, respectively, over most catalysts regardless of the active phase, preparation technique or reaction temperature. This agreed well with an Eley-Rideal mechanism whereby excess oxygen

was adsorbed dissociatively on the catalytic sites with negligible methane surface coverage, and whereby the rate-limiting step was the surface reaction between an adsorbed oxygen atom and a methane molecule from the gas phase [10]. At low temperatures (i.e. 50-100°C higher than the observed light-off temperature), the apparent reaction order for methane would deviate significantly from 1 for methane:oxygen ratios of ≥ 1:10. Such deviation from the Eley-Rideal model at high methane:oxygen molar ratios has also been observed over other combustion catalysts, such as PdO/Al_2O_3 [10]. In most cases, a decrease in the reaction order with respect to methane to 0.4-0.6 was noted for the BHA-based systems. Figure 4.14 shows a plot of the apparent reaction rate under differential conditions as a function of inlet CH_4 concentration over 7.5 at% Mn-coated BHA. This plot clearly illustrates a shift in the apparent methane reaction order from ~1 to ~0.4 at CH_4 concentrations ≥ $4x10^{-5}$ mol/L (corresponding to CH_4:O_2 ratios ≥ 1:10). In contrast, the reaction rate with respect to oxygen remained essentially unchanged (~½). The shift in the apparent reaction order for methane might be caused by a deprivation of oxygen at the catalyst surface due to reaction. At low temperatures and relatively high methane concentrations, the rate at which oxygen was replenished on the catalyst surface might be lower than the rate at which surface oxygen reacted with methane. At higher temperatures (i.e. > 100°C above the light-off temperature), the deviation in the methane apparent reaction order was less pronounced, typically within experimental uncertainties.

In-situ DRIFT studies were performed on MnO_2- and CeO_2-coated BHA samples in attempt to verify the proposed mechanisms under fuel-lean conditions (methane:oxygen molar ratios of 1:100 to 1:5) at 400-600°C. Under these reaction conditions, we did not detect any surface methyl species (1350-1400 cm^{-1}) or physisorbed methane species (~2900 cm^{-1}). Only a band at ~3010 cm^{-1} (corresponding to the asymmetric stretch of gas-phase methane [11]) was noted in the DRIFT spectra. These results suggested that methane and methyl species were not present on the catalyst surface at concentrations detectable by the instrument under the ultralean reaction conditions examined, confirming the findings of the kinetics studies.

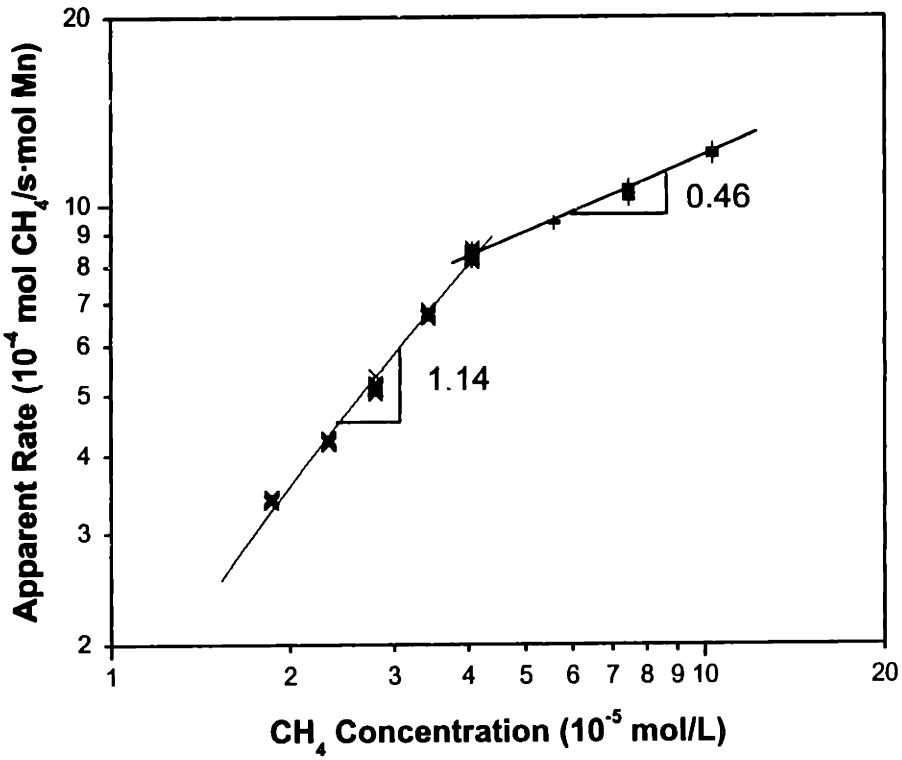

Figure 4.14. Apparent reaction rate at 450°C for 7.5 at% Mn-coated BHA as a function of CH_4 concentration in the inlet stream. O_2 concentration: $1x10^{-3}$ mol/L, GSHV: 60,000 h^{-1}.

Assuming an Arrhenius form for the rate constant, the apparent activation energy for methane combustion was calculated for various modified BHA catalysts. The systems varied in activation energy depending on the nature and loading of active components, method of catalyst preparation, component dispersion and overall surface area. The BHA nanoparticles coated with 7.5 at% Mn and 3.0 at% Ce were the most active nanocomposite catalysts, exhibiting activation energies comparable to those observed over noble metal-based catalysts, such as PdO/Al_2O_3 and Pt/Al_2O_3. Table 4.5 summarizes the apparent activation energy and pre-exponential factors of the Arrhenius rate constants of these selected catalysts for methane combustion. It is noteworthy that the coated BHA nanoparticles not only displayed excellent catalytic activity, but demonstrated superior thermal resistance, compared to conventional noble metal-based systems.

Table 4.5. Catalytic properties of coated BHA nanoparticles and conventional noble metal-based systems. Feed: 1 vol% CH_4 in air, GSHV: 60,000 h^{-1}.

Catalyst	Light-off Temperature (°C)	Activation Energy (kJ/mole)	Pre-exponential Factor ($cm^{5/2}\cdot mole^{1/2}/s$)
7.5 at% Mn-coated BHA	395-400	108 ± 10	$9.2x10^{10}$
3.0 at% Ce-coated BHA	410-415	143 ± 10	$1.0x10^{11}$
0.5 wt% PdO/Al_2O_3	320-325	85 ± 4	$8.1x10^{10}$
1.0 wt% Pt/Al_2O_3	375-380	134 ± 5	$1.3x10^{11}$

4.3.2.5 Temperature-Programmed Desorption Studies

Oxygen TPD studies were conducted over pure and modified BHA catalysts in attempt to correlate their catalytic activity to their O_2 uptake. Pure BHA showed negligible oxygen desorption below 1000°C. For 800°C-calcined 7.5 at% Mn-coated BHA and 7.5 at% Mn-impregnated BHA, a low-temperature desorption peak was observed at 100-300°C (Figures 4.15(b) and (c)). This peak could be attributed to physisorbed (or weakly chemisorbed) oxygen species, which were more abundant in the MnO_2-coated sample than in the MnO_2-impregnated sample, possible due to the higher MnO_2 dispersion in the former. The low-temperature peak was not observed in the Mn-doped BHA sample (Figure 4.15(a)), which did not have MnO_2 nanoclusters dispersed on the BHA surface. High-temperature oxygen evolution began at 500°C, 370°C and 420°C for the doped, coated, and impregnated BHA samples, respectively. These temperatures matched rather closely to the observed light-off temperatures of 500°C, 395°C and 420°C, for the respective catalysts. The total amounts of oxygen desorbed between 350°C and 1000°C corresponded to 175, 210 and 100 mmol O_2/mol Mn for the doped, coated and impregnated BHA samples, respectively (Figure 4.16). Oxygen evolution above 350°C could be attributed to removal of lattice oxygen associated with Mn species.

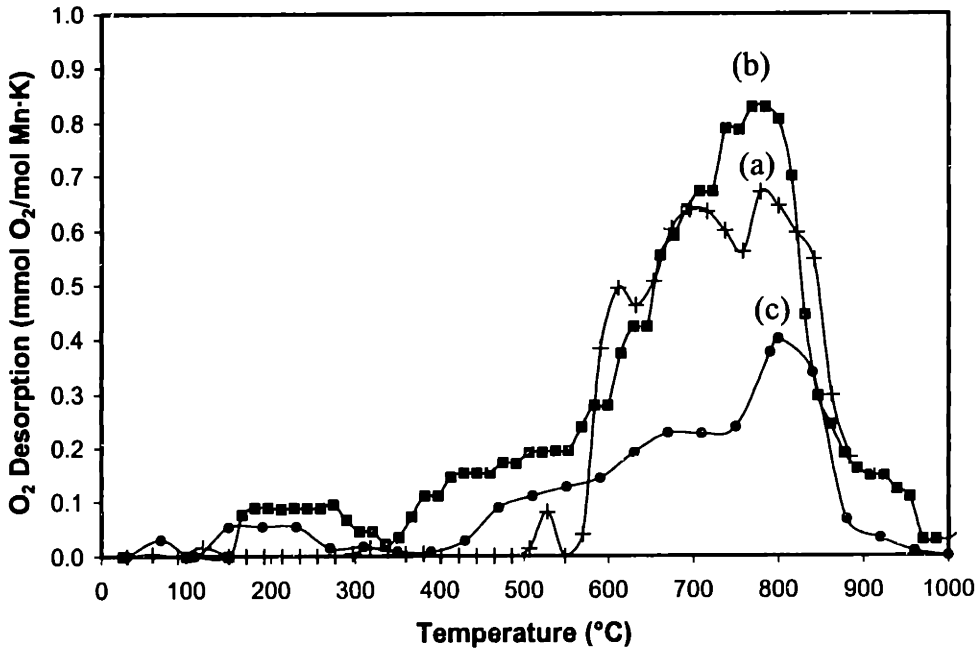

Figure 4.15. O_2 temperature-programmed desorption of 800°C-calcined BHA samples (a) doped, (b) coated, and (c) impregnated with 7.5 at% Mn.

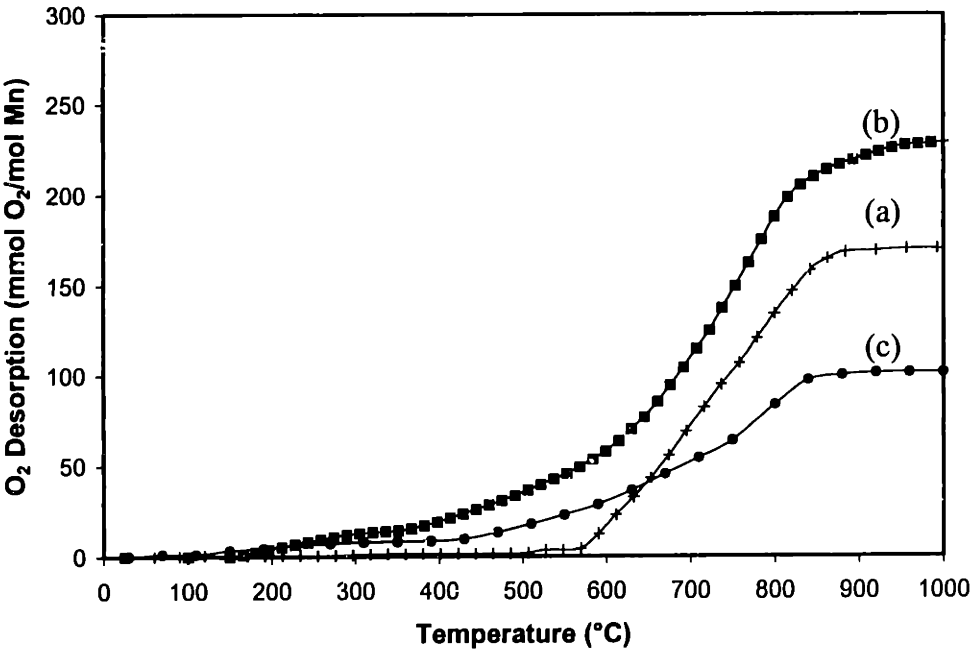

Figure 4.16. Integrated O_2 temperature-programmed desorption of 800°C-calcined BHA samples (a) doped, (b) coated, and (c) impregnated with 7.5 at% Mn.

For Ce-containing samples, no qualitative difference was observed in the TPD profiles of doped and coated BHA materials. Both materials consisted of CeO_2 clusters deposited on BHA nanoparticles, but the latter possessed a higher dispersion of CeO_2,

giving rise to a substantially greater amount of oxygen desorbed (see Figure 4.17). In contrast, impregnated samples showed little oxygen desorption below 1000°C, suggesting a poor dispersion of the CeO_2 phase in the 800°C-calcined sample. The CeO_2-coated samples have very different TPD profiles from Mn-containing samples. In addition to the low-temperature desorption peak (150-380°C) corresponding to physisorbed (or weakly chemisorbed) oxygen, two distinct peaks were noted at higher temperatures for the CeO_2-coated BHA systems (Figure 4.18). The peak at 380-550°C could be attributed to the desorption of chemisorbed oxygen, and the peak at 550-920°C might be associated with the removal of lattice oxygen species from CeO_2 coatings. As with MnO_2-coated samples, the temperature at which chemisorption was first observed in the CeO_2-coated materials corresponded quite closely with the light-off temperature for these systems (Table 4.4). A slightly higher amount of lattice oxygen (120 mmol O_2/mol Ce) was removed (550-920°C) from 3.0 at% Ce-coated BHA than from 4.0 at% Ce-coated BHA (100 mmol O_2/mol Ce), possibly due to the finer CeO_2 crystallite size in the former, which would facilitate lattice reduction (Figure 4.19). The amount of chemisorbed oxygen (380-550°C) was significantly higher for the sample containing 3.0 at% Ce (~70 mmol O_2/mol Ce) than for the sample containing 4.0 at% Ce (~30 mmol O_2/mol Ce). This could be attributed directly to the higher CeO_2 dispersion associated with the sample with a lower CeO_2 loading (Table 4.4).

For the coated BHA samples, the overall amount of oxygen desorbed per mole of active component was found to be essentially independent of loading for Mn contents of ≤ 7.5 at% and Ce contents of ≤ 3.0 at%. This suggested that the enhanced catalytic activity for the coated samples containing 7.5 at% Mn or 3.0 at% Ce over the coated BHA samples with a lower Mn or Ce loading, respectively, arose from the increased concentration of active components. On the other hand, the amount of oxygen desorbed per mole of active component was lower for the coated samples containing 10.0 at% Mn or 4.0 at% Ce, respectively. This could be attributed to the lower dispersion of MnO_2 or CeO_2 at these higher loadings, which gave rise to a higher light-off temperature compared to 7.5 at% Mn-coated or 3.0 at% Ce-coated BHA systems, respectively.

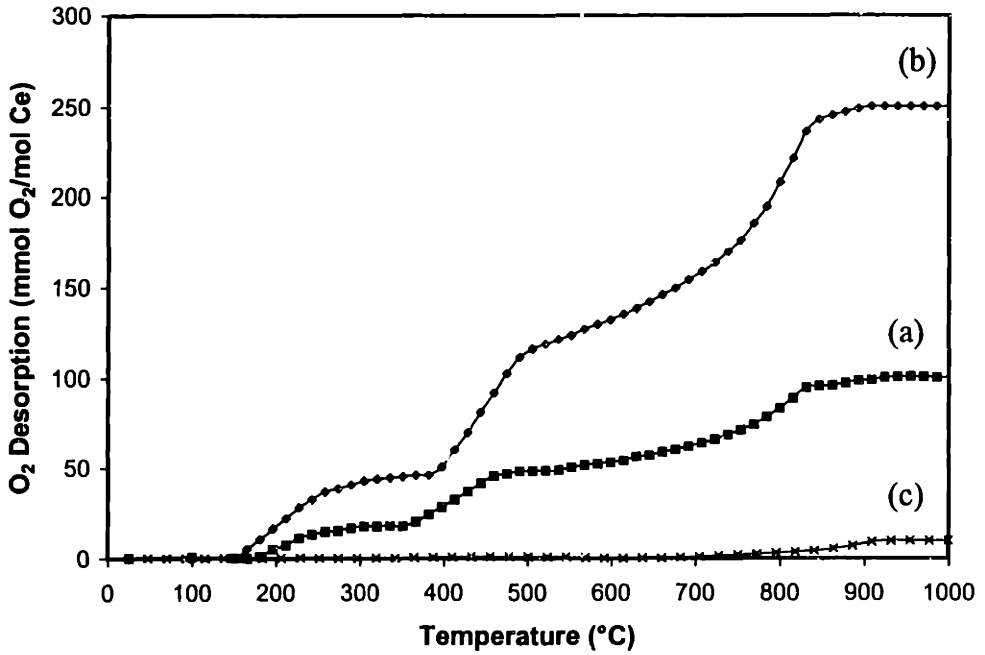

Figure 4.17. Integrated O_2 temperature-programmed desorption of 800°C-calcined BHA samples (a) doped, (b) coated, and (c) impregnated with 3.0 at% Ce.

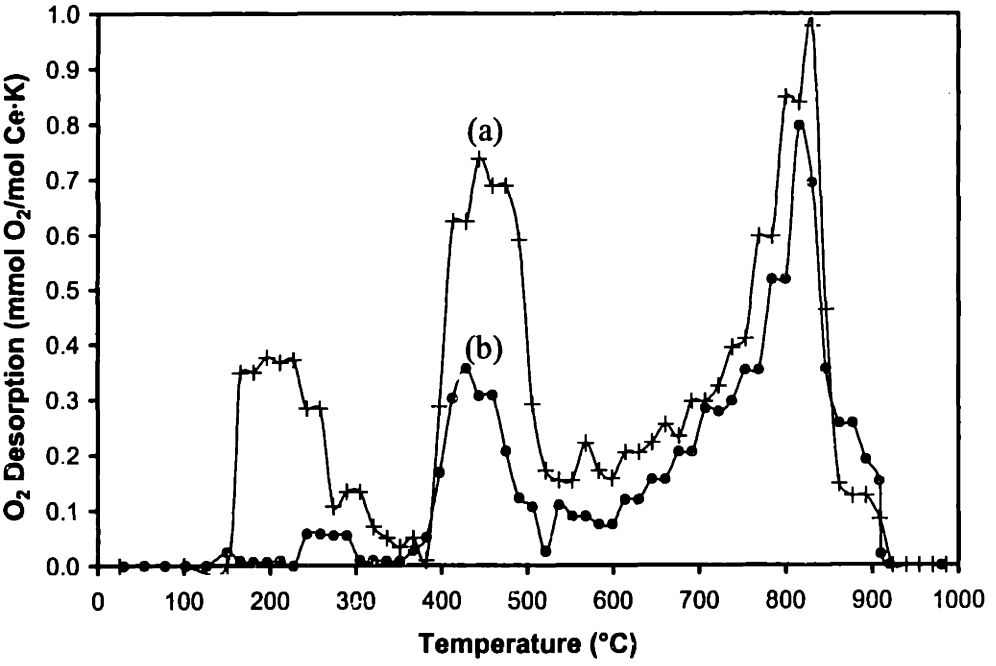

Figure 4.18. O_2 temperature-programmed desorption of 800°C-calcined CeO_2-coated BHA samples containing (a) 3.0 at% Ce and (b) 4.0 at% Ce.

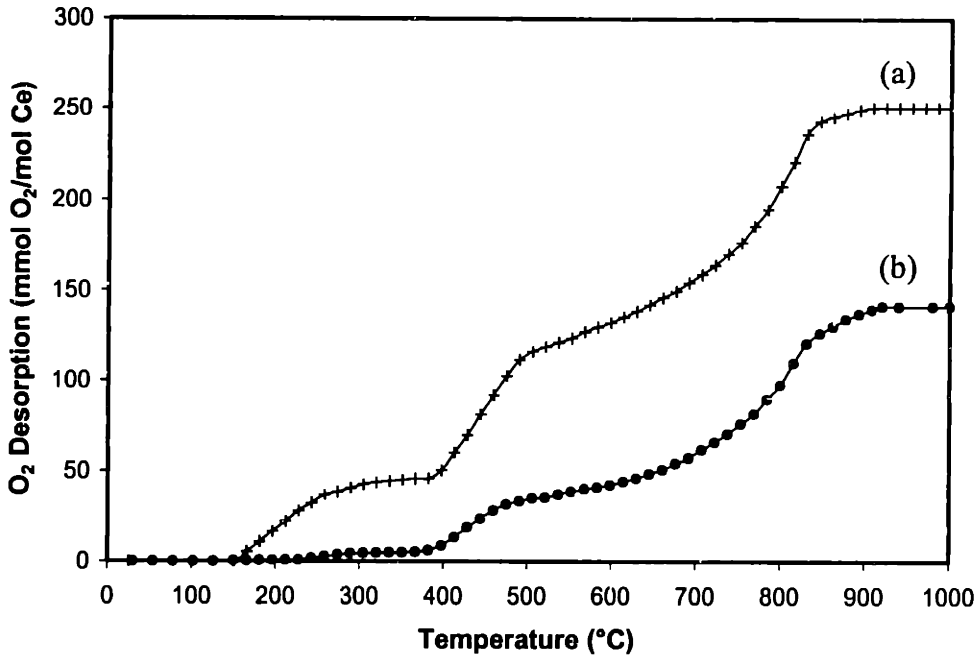

Figure 4.19. Integrated O_2 temperature-programmed desorption of 800°C-calcined CeO_2-coated BHA samples containing (a) 3.0 at% Ce and (b) 4.0 at% Ce.

4.4 Summary

Modified barium hexaaluminate nanoparticles have been prepared by reverse microemulsion-mediated sol-gel processing. Mn and Ce have been introduced to BHA as structural dopants, nanocrystalline oxide coatings, or impregnated surface oxides. Compared to BHA nanoparticles loaded with active species via the conventional impregnation technique, BHA nanoparticles doped or coated with active components in the reverse microemulsion medium exhibited superior thermal resistance and catalytic activity.

Up to 22.50 at% of Al could be substituted by Mn in the BHA structure, expanding the unit cell of BHA significantly. When ≥ 11.25 at% of Mn was introduced, a separate $MnAl_2O_4$ phase was produced; the low thermal stability of this phase led to significant loss of surface area when the sample was calcined at 1300°C. In contrast, 7.50 at% Mn-doped BHA nanoparticles retained substantial surface areas at elevated temperatures. They possessed a catalytic activity superior to pure BHA nanoparticles or Mn-doped sol-gel derived BHA, achieving light-off of a stream of 1 vol% CH_4 in air at 500°C. Unlike Mn, Ce could not be successfully introduced into the BHA structure; a

separate CeO_2 phase was produced even at low Ce loadings. Crystallization of BHA was inhibited in the presence of ≥ 2.0 at% Ce loading. Methane light-off over the Ce-doped material was successfully achieved at a lower temperature (~465°C) than over the Mn-doped BHA. The optimal dopant concentrations were found to be 3.75 at% and 2.0 at% for Mn- and Ce-doped BHA nanoparticles, respectively.

Thermal resistance of nanocrystalline MnO_2 and CeO_2 was greatly improved when these active materials were highly dispersed on the thermally stable BHA nanoparticles. This was achieved in the coated BHA systems, which displayed better catalytic activity than the doped BHA materials. Light-off was achieved at ~395°C and ~410°C for MnO_2- and CeO_2-coated samples, respectively. The optimal MnO_2-coated system (7.5 at% Mn) retained an ultrahigh surface area of 476 m^2/g after pre-treatment at 800°C, with MnO_2 grain size of 14 nm. The best CeO_2-coated BHA (3.0 at% Ce) retained surface areas of 306 m^2/g and 60 m^2/g at 800°C and 1300°C, respectively. The CeO_2 grain sizes were only 8 nm and 24 nm after these heat treatments.

The kinetic analysis of coated BHA nanoparticles indicated that methane oxidation over these catalysts under fuel-lean conditions followed a Eley-Rideal mechanism, whereby oxygen was adsorbed dissociatively on the catalyst surface with negligible methane surface coverage. The apparent activation energies for methane combustion over these novel materials were comparable to those over the supported noble metal catalysts. Compared to PdO/Al_2O_3 and Pt/Al_2O_3, the modified BHA materials demonstrated superior thermal stability. In particular, the CeO_2-coated BHA catalysts were successfully used for extended periods in catalytic methane combustion at temperatures exceeding 1100°C and in the presence of up to 10 vol% H_2O. They retained the ultrahigh CeO_2 dispersion, exhibiting no deactivation or hysteresis in their catalytic behavior during heating-cooling-restarting cycles.

4.5 References

[1] A. J. Zarur, H. H. Hwu, J. Y. Ying, *Langmuir,* in press.

[2] A. J. Zarur, J. Y. Ying, *Nature,* in press.

[3] M. Machida, A. Sato, T. Kijima, H. Inoue, K. Eguchi, H. Arai, *Catal. Today* **26**, 239 (1995).

[4] M. Machida, A. Sato, M. Murakami, T. Kijima, H. Arai, *J. Catal.* **157**, 713 (1995).

[5] D. B. Wiles, R. A. Young, *J. Appl. Crystall.* **14**, 149 (1981).

[6] S. J. Gregg, K. S. W. Sing, "Adsorption, Surface Area and Porosity," 2nd ed. Academic Press, New York, 1982.

[7] J. Y. Ying, A. Tschöpe, *Chem. Eng. J.* **64**, 225 (1996).

[8] M. Machida, K. Eguchi, H. Arai, *Bull. Chem. Soc. Jpn.* **61**, 3659 (1988).

[9] M. Machida, K. Eguchi, H. Arai, *J. Catal.* **120**, 377 (1989).

[10] P. Markatou, L. D. Pfefferle, M. D. Smooke, *Comb. Fl.* **93**, 185 (1993).

[11] L. H. Little, A. V. Kiselev, V. I. Lygin, "Infrared Spectra of Adsorbed Species." Academic Press, New York, 1966.

Chapter 5. Performance of Nanostructured BHA-based Materials in a Catalytically Stabilized Thermal Combustor

5.1 Introduction

The concept of a catalytically stabilized thermal combustor (CSTC) was first introduced by Pfefferle [1]. A catalyst system is used in CSTC to sustain a lean flame that would otherwise be unstable in homogeneous combustion. In general, an equivalent molar ratio (ϕ) of 0.53 or higher is required to maintain a stable homogeneous methane flame in the gas phase at atmospheric pressure [2]. The equivalent molar ratio is defined as:

$$\phi = \frac{\text{actual } CH_4 : O_2 \text{ ratio}}{\text{stoichiometric } CH_4 : O_2 \text{ ratio } (1:2)} \tag{5.1}$$

Conventional natural gas burners usually operate at $0.75 \leq \phi \leq 1.0$ to prevent instabilities due to small variations in the fuel feed. The adiabatic flame temperatures calculated at these equivalent ratios are 1520°C and 1920°C, respectively. Under these conditions, production of NO_x in the flame can be significant. The role of a catalyst in systems with $\phi < 0.5$ is to generate radical species that can stabilize the flame front [3].

It would be ideal to design a CSTC with a single catalyst stage that could light-off[‡] at low temperatures (350-450°C) and withstand the high temperatures present in the flame front (1100-1300°C). However, recent studies suggest that more than one catalyst stage would be necessary in a realistic CSTC design, since catalysts able to light-off at low temperatures, such as supported noble metals or transition metal oxides, would lose activity rapidly at the elevated temperatures close to the flame front [4]. A multi-stage design would involve a pre-combustion and pre-heating zone, a low-temperature ignition catalyst, a high-temperature flame-supporting catalyst, and a combustion chamber (Figure 5.1) [5]. In the pre-combustion chamber, small amounts of fuel are

[‡] The definition of "light-off" for a CSTC is different from that for an isothermal packed-bed flow reactor. In the latter, light-off describes the temperature at which 10% fuel conversion is achieved. In an adiabatic CSTC, 10% conversion of the fuel usually leads to an enormous temperature rise, which further increases the catalytic activity and often leads to flame ignition. Therefore, light-off for a CSTC is defined as the inlet temperature at which an adiabatic temperature rise of ≥10°C is observed.

homogeneously burned at ϕ=0.75-1.0 to preheat the air stream entering the combustor. The preheated air carries the fuel from the main inlet port through the low-temperature catalyst, which initiates the combustion. The partially converted stream then flows through the high-temperature catalyst stage, which supports the flame in the combustion chamber. The exhaust gases are then sent through the gas turbine.

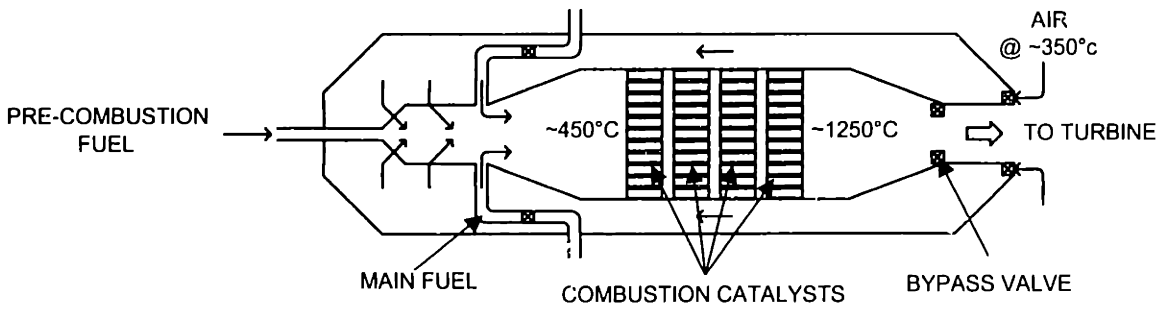

Figure 5.1. Schematic of a multi-stage catalytic combustor.

The inlet temperature of the feed stream to the first catalyst stage should be as low as possible to minimize pre-heating requirements. Pre-heating is provided by a flame that is burned at near-stoichiometric conditions and may lead to NO_x formation. Several recent designs propose an inlet temperature of 350-450°C [4-8].

The temperature on the surface of the flame-supporting catalyst would be similar to that of the adiabatic flame, which depends on the inlet temperature and ϕ. Figure 5.2 shows the calculated adiabatic flame temperature as a function of ϕ for different inlet temperatures. It would be desirable to operate a CSTC at temperatures between 1300°C and 1400°C. At these conditions, a negligible amount of NO_x is generated and a high Carnot efficiency (η~0.58) can be achieved in the turbine cycle [5]. In addition to high temperatures, the flame-supporting catalyst would be subjected to hydrothermal conditions from the steam generated during combustion, and to thermal shock during start-up or shut-down. The high-temperature catalyst should be able to sustain operation under these conditions for extended periods.

In this chapter, we discuss the applicability, performance and thermal resistance of several novel ignition and flame-supporting catalysts for an atmospheric CSTC. These catalysts consisted of different active species supported on nanostructured BHA-based

powders. They were washcoated or deposited onto monoliths or foams of various compositions and configurations.

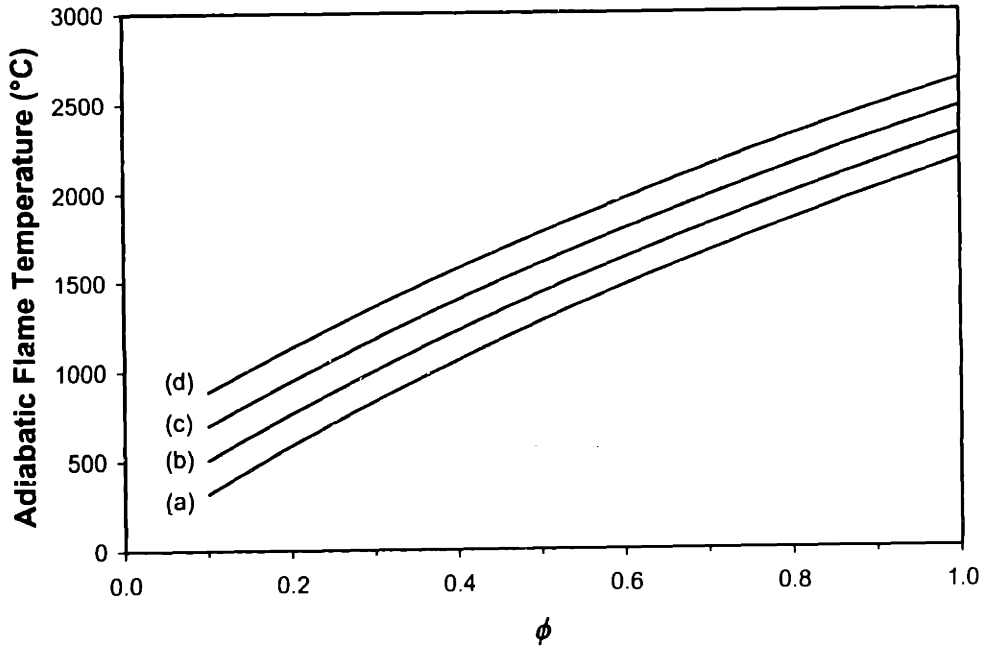

Figure 5.2. Adiabatic flame temperature calculated as a function of equivalent molar ratio for inlet temperatures of (a) 25°C, (b) 225°C, (c) 425°C, and (d) 625°C.

5.2 Experimental

5.2.1 Synthesis of Catalytic Washcoats

Noble metal and metal oxide systems supported on nanostructured BHA were investigated as low-temperature ignition catalysts. Pure and modified nanostructured BHA were used as the high-temperature flame-supporting catalyst.

The noble metal systems consisted of PdO supported on nanostructured BHA. The BHA powders were prepared by the reverse microemulsion-mediated synthesis described in Chapter 3 [9-11], and were calcined to 800°C prior to Pd loading. In addition to pure BHA, CeO_2-coated BHA powders were used as supports [10]. CeO_2 was introduced to promote oxygen spill-over to the PdO sites, and to prevent deactivation of PdO from reduction to Pd.

Two different synthesis techniques were used to introduce PdO onto BHA supports. The first technique involved vapor grafting of an organometallic precursor

[12,13]. Pd(η-C_5H_5)(η^3-C_3H_5) was sublimed under air-free conditions and allowed to condense on the surface of nanostructured BHA powders. The resulting materials were reduced in a flowing stream of 7 vol% H_2/He at 300°C for 2 h, followed by calcination in air at 600°C for 1 h. This approach produced highly dispersed PdO on BHA surface. The resulting materials consisted of 6-10 wt% Pd and were amorphous by XRD.

The second technique involved impregnation of nanostructured BHA powders. Typically, 4 g of $PdCl_2$ were dissolved in 100 ml of an aqueous HCl solution (10 M). 10 g of pure or CeO_2-coated BHA powders, previously calcined to 800°C, were then added to the $PdCl_2$ solution. The mixture was aged overnight at 50°C with stirring to ensure uniform impregnation, and the resulting powders were then dried in air. The samples were further oven-dried at 120°C for 2 h, and calcined in air at 600°C for 1 h. The final Pd loading on the BHA-based materials was ~20 wt%.

The low-temperature metal oxide systems consisted of nanocrystalline MnO_2 and/or CeO_2 coated onto BHA nanoparticles during their aging in the reverse microemulsion medium (see Chapter 4 [14]). Samples loaded with 7.5 at% Mn, 3.0 at% Ce, and 5.5 at% Mn-2.5 at% Ce were prepared using the respective metal nitrate salt(s). The BHA nanoparticles coated with active metal oxides were recovered from the reverse microemulsion by filtration and calcined to 800°C.

CeO_2-coated and pure BHA nanoparticles calcined at 1100°C and 1300°C, respectively, were used as the flame-supporting catalysts.

5.2.2 Support of Active Materials on Reticulated Ceramics

Reticulated ceramics have recently received significant attention as high-temperature catalyst supports [15-19]. These materials are highly porous (80-90% void volume), three-dimensional foam-like structures. Compared to conventional straight-channel honeycombs, they possess greater pore tortuosity, which enhances reactant mixing and radial distribution across the monolith [16]. Foams of thermally resistant ceramics, such as alumina, cordierite, mullite and yttria-stabilized zirconia (YSZ), are commercially available.

α-Al_2O_3 and YSZ foams with pore densities ranging from 30 to 65 ppi were obtained from High-Tech Ceramics (Alfred, NY). Ceramic foams were also synthesized

[16,17] in-house from ultrafine Al_2O_3 and BHA powders, in attempt to improve on adherence of washcoats and thermal shock resistance of monoliths. BHA powders were obtained from reverse microemulsion-mediated synthesis [9], and α-Al_2O_3 powders were synthesized by sol-gel processing of aluminum isopropoxide. These powders were calcined at 1300°C for 2 h, and then milled in ethanol with ZrO_2 balls for 24 h. The milled powders were mixed with water to form a fixotropic slurry of ~50 vol% solid. A wetting agent (Surfynol, Air Products), a dispersant (Darvan C, R. T. Vanderbilt), and a binder (polyethylene oxide, MW~50000, Aldrich) were added to the suspension in concentrations of ~1 vol% each. The suspension was sonicated for 15 minutes to break up loose aggregates. Reticulated polyurethane foams with pore densities ranging from 15 to 60 ppi were obtained from Specialty Products (Tacoma, WA). The foams were washed with ethanol, and coated by immersion in the slurry. The coated foams were then compressed to about 85% of their original size by pressing them between two porous quartz discs to remove excess coating material. The resulting structures were allowed to dry at room temperature for 24 h and at 120°C for 6 h. They were calcined in a box furnace at 1000°C for 4 h for removal of binders and additives, and to provide some mechanical stability prior to sintering. The monoliths were then heated to 1450°C for 4 h, yielding mechanical and thermal stabilities similar to those of the commercially available reticulated ceramics.

Active washcoats were introduced onto the reticulated ceramics following a dip-coating procedure [16]. The catalyst powders (10-20 wt%) were suspended in an aqueous solution containing ~1 vol% each of the wetting agent, dispersant and binder described earlier. The suspension was sonicated for 15 minutes to break up loose agglomerates. The monoliths were dip-coated in the suspension (~100-200 cP) and allowed to dry in air; this procedure was repeated until a loading of ~20 wt% washcoat was achieved on the reticulated ceramics. The coated monoliths were dried in air at room temperature for 24 h and at 120°C for 3 h. They were then calcined at 600°C for the Pd-containing monoliths, 800°C for the CeO_2- and MnO_2-containing monoliths, and 1300°C for the pure BHA-coated monoliths.

5.2.3 Support of Active Materials on Fiber-Reinforced Honeycombs

In the normal operation of a co-generation plant, a gas turbine may be started up and shut off several times during a day. The temperature of the catalyst stages in a CSTC may decrease from ~1300°C to 300°C within seconds during shut-off [20]. This rapid and non-uniform change in temperature may result in fracturing of the monolith due to uneven contraction. Fracturing due to thermal shock is more common in rigid, dense structures than in ductile, porous systems [21,22].

Fiber-reinforced honeycombs are glass-ceramic composites with greater flexibility and shock resistance than conventional ceramic monoliths [22,23]. They are fabricated with a variety of compositions and pore densities (30-500 channels/in^2). The channel walls are composed of interwoven glass fibers coated with ceramic particles. Their high porosity and surface roughness provide for enhanced adhesion of catalyst powders compared to the smooth surfaces of reticulated ceramics. Fiber-reinforced honeycombs are prepared from preforms of glass fibers, which are arranged in layers. The fibers in each layer are woven in parallel to each other, and perpendicular to fibers in adjacent layers. The preforms are dip-coated in a dispersion of 10-20 wt% ceramic particles (e.g. alumina and magnesia) (100-300 cP). The coated preforms are dried, and calcined at 1400°C to melt the silica fibers and promote their reaction with the magnesia and alumina ceramic particles to form cordierite and mullite. After heat treatment, the silica fibers are no longer continuous but the walls of the straight channels remain intact, providing mechanical stability and thermal shock resistance. Typical final compositions are 10-20 wt% SiO_2, 60-70 wt% Al_2O_3, 5-10 wt% MgO [20].

Fiber-reinforced honeycombs with 64 and 100 channels/in^2 were obtained from Allied-Signal Industries (Willmington, DE). These monoliths were dip-coated with Pd/BHA, Pd/CeO_2-BHA, CeO_2-BHA, MnO_2-BHA, CeO_2-MnO_2-BHA, and pure BHA nanoparticles following the procedure outlined in Section 5.2.2.

5.2.4 Support of Active Materials on Nickel Foams

In addition to fiber-reinforced honeycombs, metallic foams were investigated as monoliths. These materials have a structure similar to that of reticulated ceramics, but the high ductility of the nickel provides greater resistance to thermal shock. Nickel

foams were also chosen for their high melting point (1453°C) and oxidation resistance. However, the cell size of commercially available metallic foams (~0.3 mm) is significantly smaller than that of reticulated ceramics (~1 mm). This may cause significant pressure drop at the space velocities and high temperatures present in catalytic combustors. Also, the nanoparticulate oxide washcoats may not adhere as strongly onto metallic foam surfaces as onto reticulated ceramics.

Catalyst washcoats were introduced onto the nickel foams through electrophoretic deposition [24]. Nickel foams (99.0% purity) with a nominal porosity of 96.5% and a pore density of 31.5 pores/cm were obtained from Goodfellow (Berwyn, PA). The desired pre-calcined ceramic powders were added to a solution of ethanol, water and nitric acid with a pH of ~4.0. The suspension was sonicated for 1 h to break up loose aggregates. A field of ~30 V/cm^2 was applied between a platinum anode and the metallic foam (which acted as the cathode) in a bath containing the suspended powder. Coatings of 6-20 wt% Pd-BHA, MnO_2-coated BHA (7.5 at% Mn), CeO_2-coated BHA (3.0 at% Ce), and CeO_2-MnO_2-coated BHA (5.5 at% Mn, 2.5 at% Ce) were deposited onto nickel foams at a rate of ~25 μm/minute. The catalyst loadings on the nickel foams were ~20 wt% after 5-10 minutes of deposition. The resulting materials were dried and compacted in a cold isostatic press at ~1000 psi at room temperature for 5 minutes.

5.2.5 Characterization and Catalytic Studies

The different catalyst systems were evaluated for catalytic activity, stability, deactivation behavior, and thermal shock resistance. An atmospheric catalytic burner was built to investigate the light-off behavior and high-temperature activity of catalysts (see Figure 5.3).

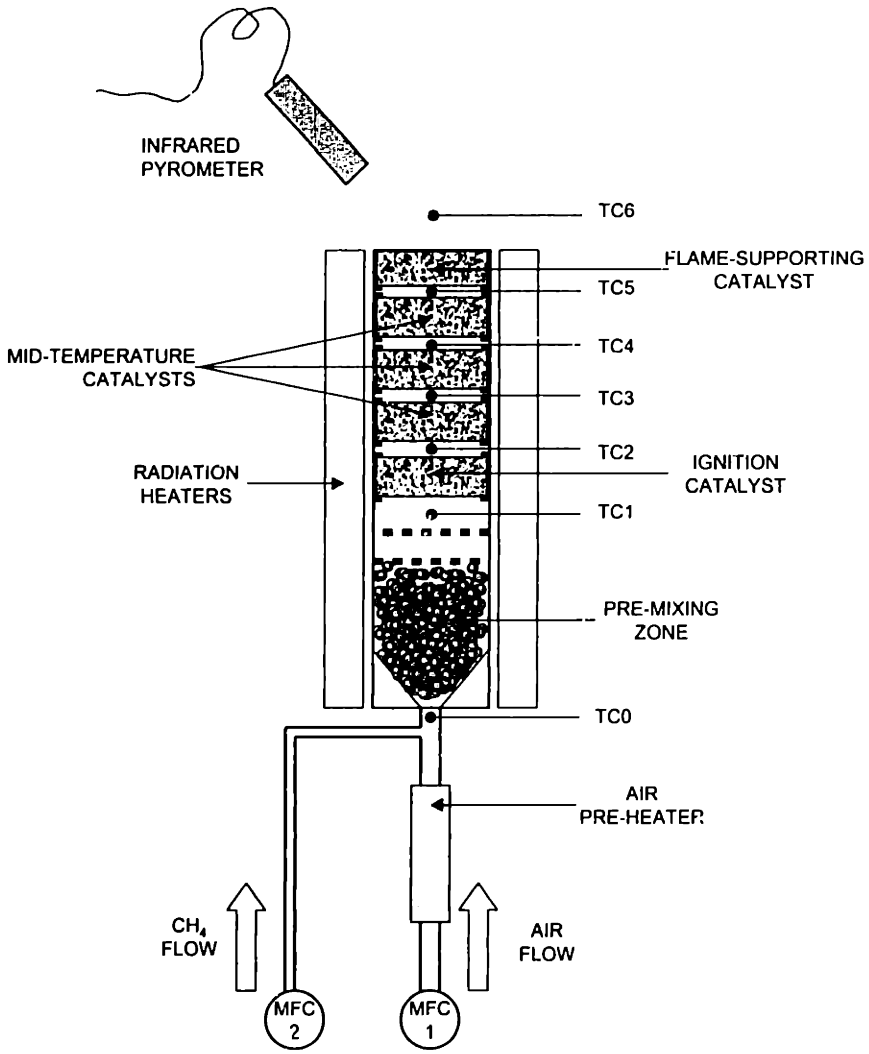

Figure 5.3. Schematic of the atmospheric CSTC reactor.

The catalytic burner consisted of a pre-heating zone, a pre-mixing zone, different catalyst stages, and a flame zone. Air and methane flows were controlled through independent MKS mass flow controllers. Air was pre-heated using an Omega electric air process heater with a maximum duty of 750 W and a maximum outlet temperature of 500°C. The pre-heated air was then mixed with methane through a nozzle, and directed to the pre-mixing zone. The pre-mixing zone consisted of 15 cm of ceramic packings and quartz discs within a stainless steel tube with an inner diameter of 4.5 cm. Up to five different catalyst stages with a total length of 30 cm could be accommodated above the pre-mixing zone in the stainless steel tube. K-type (Cr/Al) thermocouples were located

after the air pre-heater, after the pre-mixing zone, and after each of the catalyst stages. In addition, B-type (13% Pt-Rh/6% Pt-Rh) thermocouples coated with a high-temperature ceramic coating (Alcoa, Buffalo, NY) with low emissivity were used to measure the flame temperature. An infrared pyrometer was used to measure the surface temperature of the flame-supporting catalyst. Three ports were available to sample the reacting stream between the catalyst stages. The stainless steel tube containing the pre-mixing zone and the catalyst stages could be heated using two independently controlled radiation heaters. This allowed us to perform studies at higher inlet temperatures and at near-adiabatic conditions. The exhaust gases and reaction streams from the burner were analyzed using a HP 6890 gas chromatograph with a 5972 mass selective detector. NO_x in the exhaust stream was measured using a Thermo Electron Series 10 chemiluminescent NO_x analyzer. A range of space velocities, $5.0x10^5$-$2.5x10^6$ h^{-1}, could be selected by varying the gas flow or catalyst volume.

Deactivation of selected catalysts was examined by temperature-programmed desorption (TPD) and temperature-programmed reaction (TPR) studies in a Perkin-Elmer TGA7 thermogravimetric analyzer. Grain growth, phase transformation and oxidation/reduction of the catalysts were monitored with X-ray diffraction (XRD) using a Siemens D5000 θ-θ diffractometer ($Cu_{K\alpha}$, λ=1.5405 Å). Elemental analysis of different samples was performed with inductively coupled plasma - atomic emission spectroscopy (ICP-AES) in a Perkin-Elmer Plasma 40 analyzer. High-resolution transmission electron microscopy (HR-TEM) was performed on a JEM 2010 microscope (200 kV).

5.3 Results and Discussion

5.3.1 PdO-based Materials as Ignition Catalysts

Previous researchers have found PdO-based materials to be among the most active catalysts for methane oxidation at low temperatures [25-28]. The catalytic reaction appears to be sensitive to the dispersion and grain size of the supported PdO clusters [29]. PdO-based catalysts suffer from deactivation at temperatures above 650-800°C due to reduction to Pd metal (which is inactive for this reaction), and sintering and vaporization of the active PdO phase [29-31].

Our goal here was to synthesize ignition catalysts that would provide light-off at 300°C or lower, and retain activity at outlet temperatures of 600-700°C. At these outlet temperatures, other materials with superior thermal resistance (such as CeO_2- or MnO_2-coated BHA) would be fully active, and could be used as the second-stage catalyst. Table 5.1 summarizes the catalytic activity and stability of different PdO-based materials investigated as ignition catalysts.

Table 5.1. Ignition of various supported PdO systems. Reactions were run at ϕ=0.2 with SPV=500,000 h^{-1}.

Catalyst System	Pd Loading (wt%) on support	Light-off Temperature (°C)	Maximum Operating Temperature (°C)
VG PdO-BHA on RC	1.2	320	<500
IMP PdO/BHA on RC	1.2	320	<500
VG PdO-BHA on NF	1.2	320	<500
VG PdO-BHA on FRH	1.2	400	<500
IMP PdO/CeO_2-BHA on FRH	1.4	250	~700

VG = Vapor-grafted PdO
IMP = Impregnated PdO
RC = Reticulated ceramic
NF = Nickel foam
FRH = Fiber-reinforced honeycomb

5.3.1.i Effect of Palladium Deposition Technique

PdO clusters introduced onto BHA supports via vapor grafting showed higher metal dispersion than those impregnated onto BHA. Figure 5.4(a) illustrates that the vapor-grafted samples did not display any XRD peaks corresponding to PdO. The grain size of the PdO clusters was determined by HR-TEM to be 3-5 nm. In contrast, the impregnated sample showed well-defined PdO peaks (Figure 5.4(b)). The grain size of the PdO clusters, obtained by Scherrer's analysis of the (101) reflection with correction for instrumental broadening, was ~10 nm.

We found that both the vapor-grafted and impregnated materials had to be activated prior to their use as catalysts. Calcined materials were essentially inactive for methane oxidation up to 350-400°C. However, after pre-treatment for ~30 minutes at 400°C in air, most materials showed significant activity at temperatures as low as 200°C.

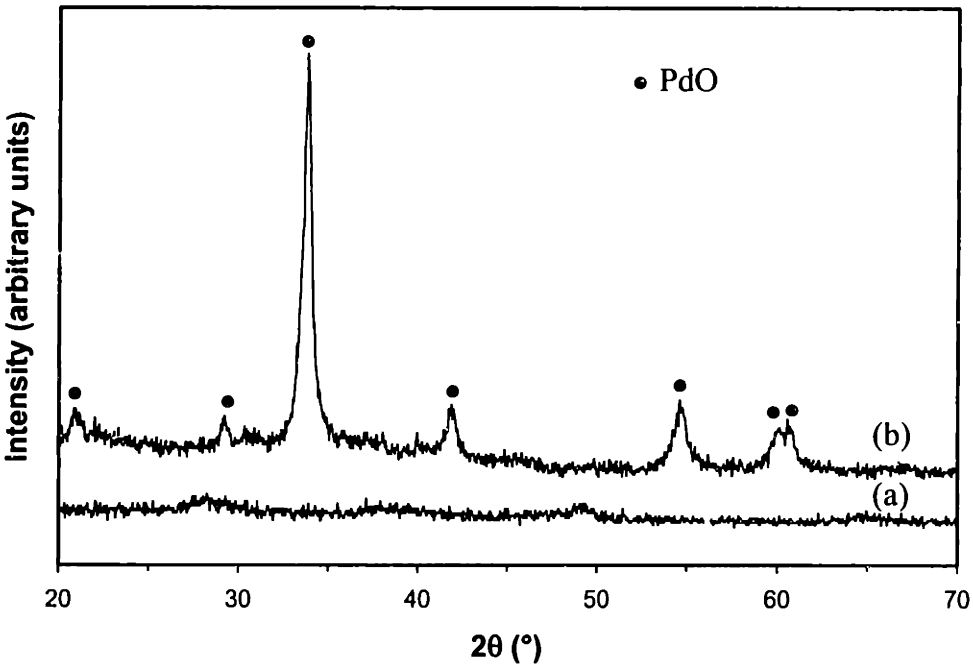

Figure 5.4. XRD patterns of (a) vapor-grafted PdO-BHA (6 wt% Pd) and (b) impregnated PdO/BHA (6 wt% Pd).

BHA samples vapor grafted or impregnated with PdO were washcoated onto a reticulated alumina monolith. For the vapor-grafted and impregnated systems, the Pd loading on BHA was ~6 wt% and the washcoat loading on the reticulated alumina was ~20 wt%, which corresponded to an overall Pd loading of 1.2 wt% on the monoliths. These coated monoliths were tested as the ignition catalysts in the burner at a space velocity of 500,000 h^{-1}. A fiber-reinforced honeycomb coated with pure BHA was used as the flame-supporting catalyst; it was also used to shield the Pd-containing ignition catalyst from high temperatures that could arise from an ignited flame.

Figure 5.5 shows the methane conversion over the ignition catalyst stage as a function of inlet temperature. The activation behavior was shown to be similar for the vapor-grafted PdO-BHA and the impregnated PdO/BHA catalysts under near-adiabatic conditions for ϕ=0.2 (Table 5.1). The methane conversion obtained experimentally from GC/MS analysis agreed well with the theoretical conversion calculated from the adiabatic temperature rise. XRD analysis of the vapor-grafted material indicated that severe agglomeration of the PdO clusters had occurred within 10 minutes in the reaction stream (Figure 5.6). The resulting PdO grain size (~11 nm), calculated by Scherrer's analysis of the (101) reflection, was similar to that observed for as-prepared impregnated materials

(~10 nm) (Figure 5.4(b)). This would explain the similar behavior exhibited by the two catalysts, despite the differences in their PdO dispersion in the as-prepared state.

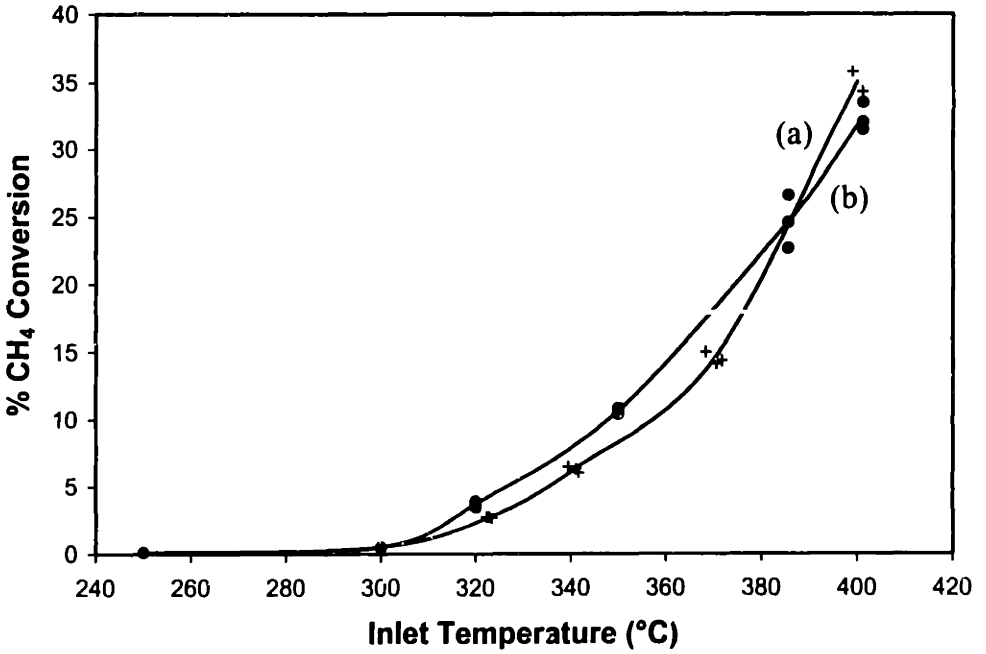

Figure 5.5. Catalytic activity of (a) vapor-grafted PdO-BHA and (b) impregnated PdO/BHA. The reactions were run at ϕ=0.2 with SPV=500,000 h^{-1}.

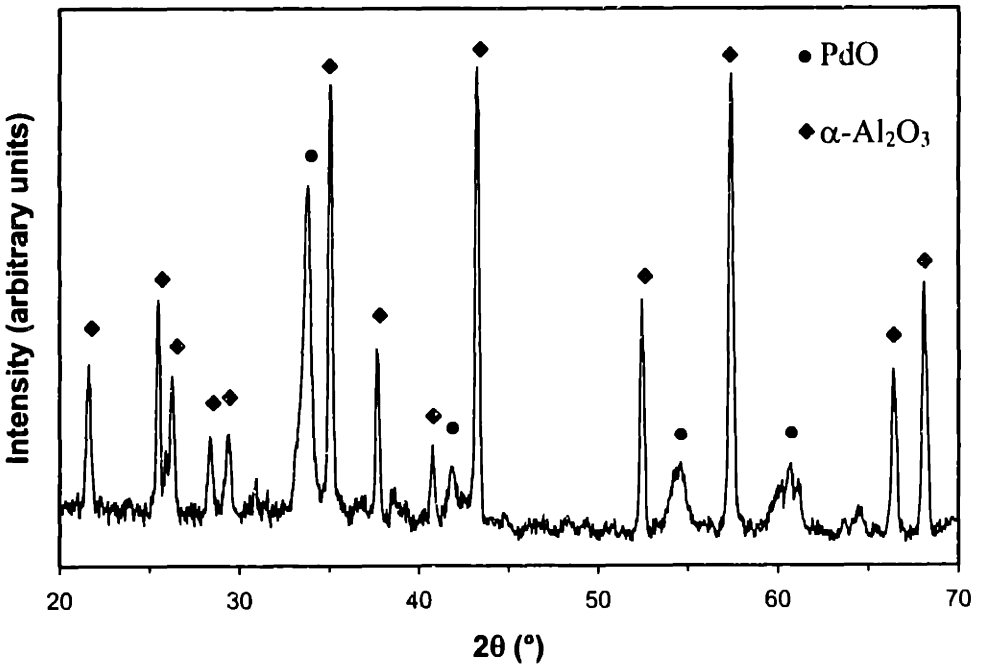

Figure 5.6. XRD pattern of vapor-grafted PdO-BHA coated onto a reticulated α-Al_2O_3, after exposure to reaction stream for 10 minutes.

5.3.1.2 Effect of Monolith Structure

The light-off behavior of different monoliths with a 20 wt% washcoat of vapor-grafted PdO-BHA (6 wt% Pd) was examined. We found that catalysts supported on metallic or ceramic reticulated structures (with ~0.3 mm and ~0.8 mm pores, respectively) required significantly lower temperatures for activation than those supported on a straight-channel honeycomb (with ~3 mm pores) (Figure 5.7, Table 5.1). Previous researchers have suggested that catalytic oxidation of methane is mass transfer limited at bulk gas temperatures above 300°C and at low Reynold's numbers [32]. The mass transfer limitations are caused by the steep temperature gradient between the catalyst surface and the bulk gas phase, which results in the formation of a relatively thick boundary layer. Our observations were consistent with this postulate. Compared to straight channels, the interconnected pore structure of the reticulated monoliths required the gases to flow at higher surface velocities. This resulted in a thinner boundary layer and an increased apparent reaction rate.

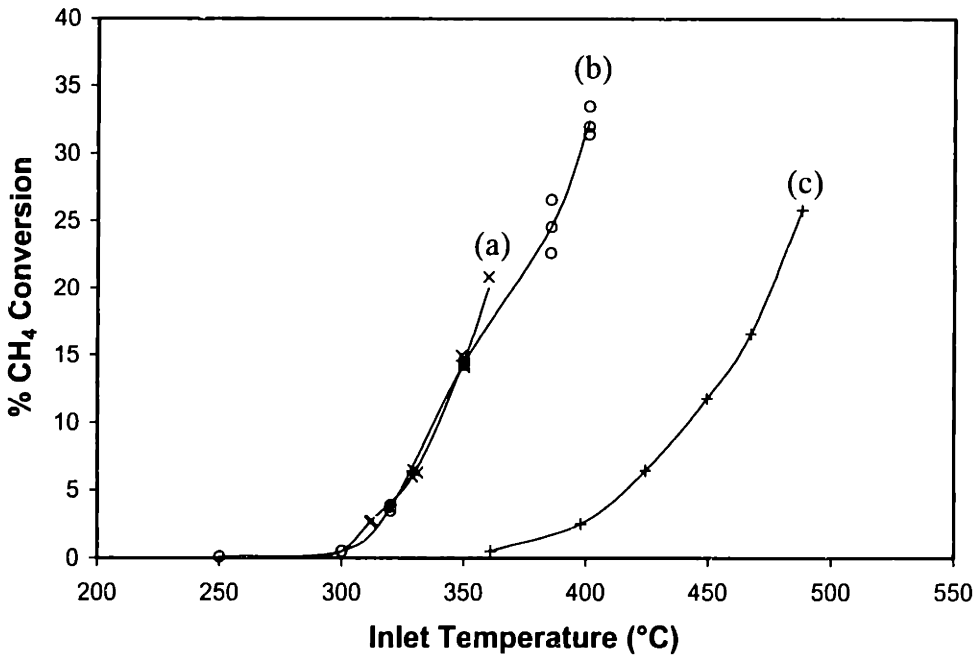

Figure 5.7. Catalytic activity of vapor-grafted PdO-BHA supported on (a) nickel foam, (b) reticulated alumina, and (c) fiber-reinforced honeycomb. The reactions were run at ϕ=0.2 with SPV=500,000 h^{-1}.

Although reticulated structures provide for superior mass transfer between the bulk gas and the catalyst surface, pressure drop becomes a significant problem for these monoliths as the gas stream temperature increases beyond 500°C. The pressure drops of an air stream flowing at 2.5×10^6 h^{-1} through a nickel foam, a reticulated alumina support, and a fiber-reinforced honeycomb were measured at 25°C, 500°C and 800°C. We found that the pressure drop over the honeycomb structure was negligible (< 0.1 psi/cm) at the three different temperatures. In contrast, the reticulated alumina gave rise to a pressure drop of 0.4 psi/cm, 1.0 psi/cm, and 1.5 psi/cm at 25°C, 500°C, and 800°C, respectively. The pressure drop through the nickel foam was even higher: 2.0 psi/cm at 25°C, 5.1 psi/cm at 500°C, and 7.4 psi/cm at 800°C. To avoid pressure drop problems, honeycomb structures were preferred over reticulated structures at high temperatures.

5.3.1.3 Deactivation of Supported PdO-based Catalysts

PdO catalysts would deactivate not only from grain growth and loss of active phase (Section 5.3.1.1), but also from reduction to metallic Pd at temperatures ≥ 550°C. Deactivation was significantly accelerated in the presence of ≥ 3 vol% methane in the reaction stream. Figure 5.8 illustrates the deactivation of PdO-containing catalysts supported on reticulated alumina at 550°C and ϕ=0.36, which corresponded to a methane concentration of 3.6 vol%. The vapor-grafted and impregnated PdO catalysts showed similar deactivation behaviors, again suggesting the similarity in their structures under the reaction conditions.

Temperature-programmed oxygen desorption and methane reduction studies were conducted on PdO/BHA to elucidate the deactivation mechanism under reaction conditions. Figure 5.9 shows the weight loss as a function of temperature for a PdO/BHA sample containing 20 wt% Pd. The degree of reduction above 400°C was significantly higher for the sample treated in 3 vol% CH_4 in air; the final weight loss corresponded to ~80% reduction of PdO to metallic Pd. In contrast, the samples reduced under flowing air and He underwent ~50% and ~60% reduction of PdO to Pd, respectively. XRD confirmed that the three heat-treated samples consisted of both PdO and Pd phases.

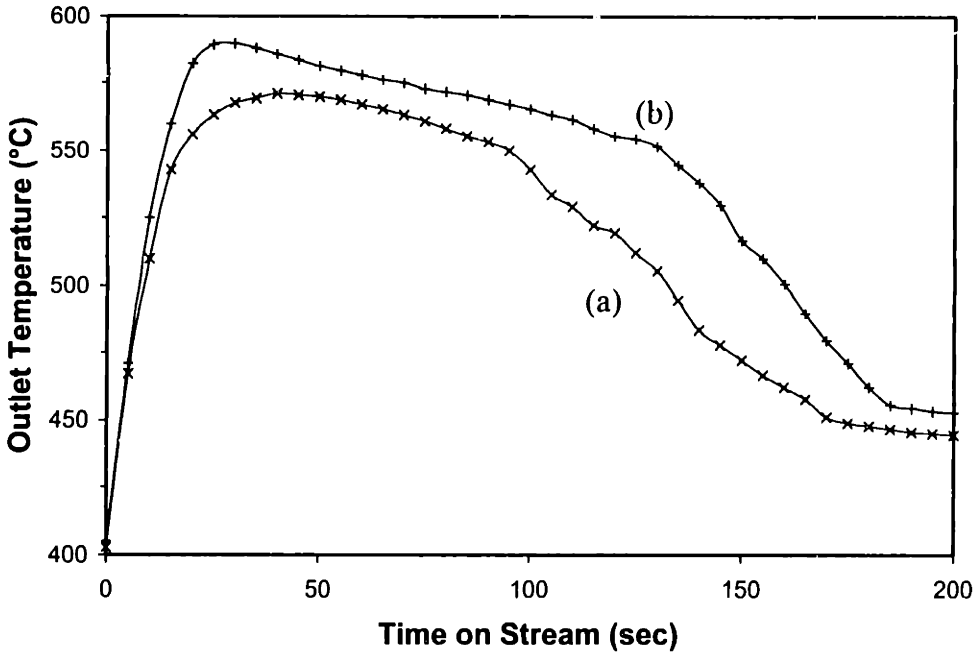

Figure 5.8. Deactivation of (a) vapor-grafted PdO-BHA and (b) impregnated PdO/BHA, both supported on reticulated alumina. The reactions were run at ϕ=0.36 with SPV=500,000 h^{-1}.

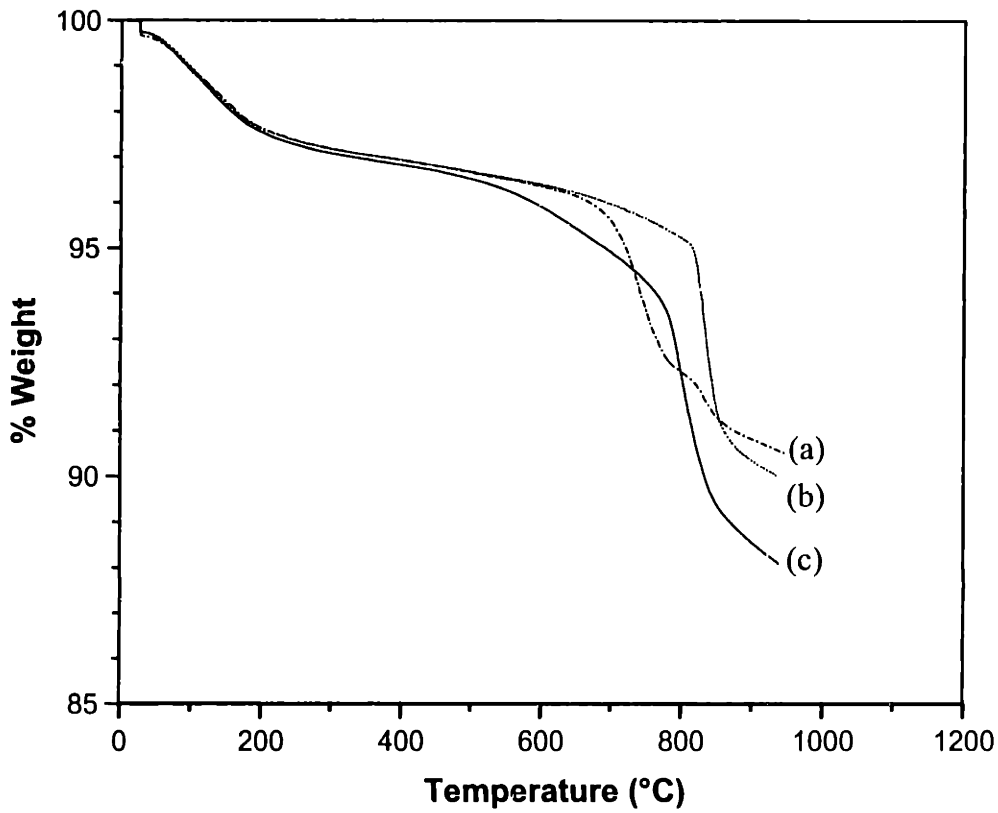

Figure 5.9. Weight loss of impregnated PdO/BHA with heat treatment in (a) air, (b) helium, and (c) 3 vol% CH_4 in air.

Introduction of methane affected not only the degree but also the rate of PdO reduction. Figure 5.10 shows the weight loss at 700°C for a PdO/BHA sample with 20 wt% Pd. The catalyst was heated in air and maintained at 700°C for 30 min, after which 3 vol% methane was introduced. Under isothermal condition, the rate of weight loss of PdO/BHA from PdO reduction was increased when methane was added to the air stream. Metallic Pd samples reduced ≤ 700°C could be fully re-oxidized to regain their catalytic activity by heat treating at 300-400°C for ~6 h in flowing air. In contrast, samples that were subjected to temperatures above 700°C could not be fully re-oxidized. This was due to severe grain growth of Pd clusters above 700°C, as evident in the XRD analysis of the Pd peaks (> 100 nm grain size). Re-oxidation was thus limited only to the surface layers of the coarsened Pd grains.

To alleviate catalyst deactivation from PdO reduction, an oxygen promoter was introduced onto the catalyst support. Cerium oxide was selected as the oxygen promoter for PdO-based combustion catalysts since it has been extensively studied as an "oxygen buffer" for automotive catalytic converter applications [33-36] and as a promoter for partial oxidation or redox reactions [37-40].

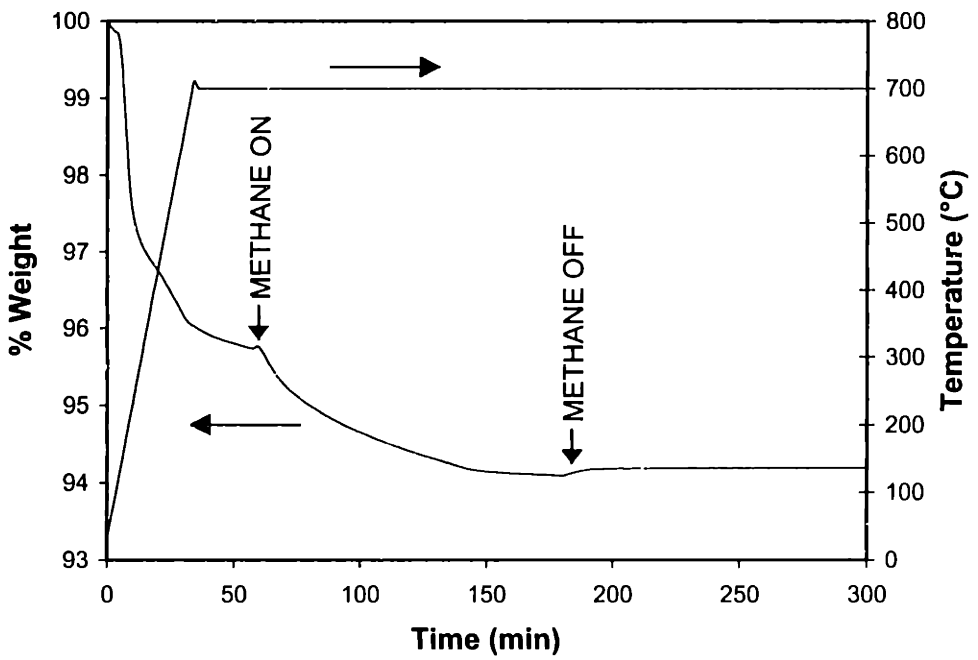

Figure 5.10. Reduction of PdO/BHA under flowing air with or without 3 vol% CH_4 addition.

5.3.1.4 Cerium Oxide as Oxygen Promoter for PdO-based Catalysts

We found that CeO_2 was able to increase the low-temperature catalytic activity and limit the reduction of PdO-based catalysts at 500-700°C. PdO/CeO_2-BHA materials were prepared by impregnating 20 wt% Pd onto CeO_2-coated BHA powders with 4 at% Ce content. These active nanocomposite catalysts were then coated onto a fiber-reinforced honeycomb to give an overall Pd content of 1.2-4 wt%. Figure 5.11 shows that the PdO/CeO_2-BHA supported on fiber-reinforced honeycombs exhibited activity at a remarkably low temperature of 220°C. It maintained high conversions at an outlet temperature of ~700°C and at ϕ values as high as 0.5. Figure 5.12(a) shows the PdO catalyst supported on CeO_2-BHA has some initial deactivation in the presence of $\geq$ 3 vol% methane; its activity became stable after ~1 minute on stream. In contrast, PdO supported on pure BHA continued to deactivate with time on stream until the temperature of the catalyst dropped below 500°C (Table 5.1).

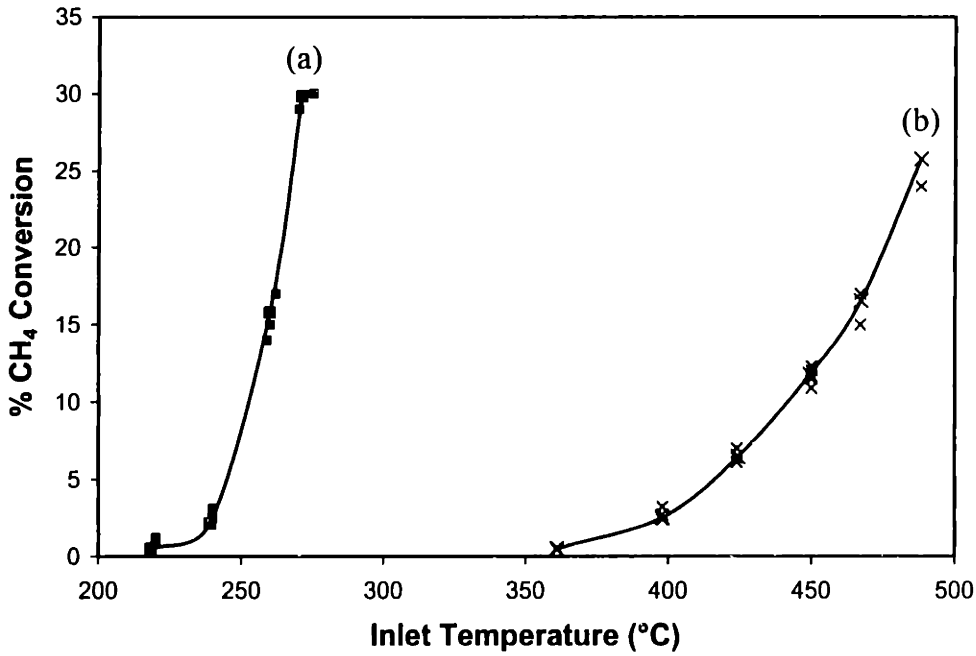

Figure 5.11. Methane conversion as a function of inlet temperature for (a) PdO/CeO_2-BHA and (b) PdO/BHA both supported on fiber-reinforced honeycombs (Pd loading = 1.2 wt% for both samples). The reaction was run at ϕ=0.3 with SPV=500,000 h^{-1}.

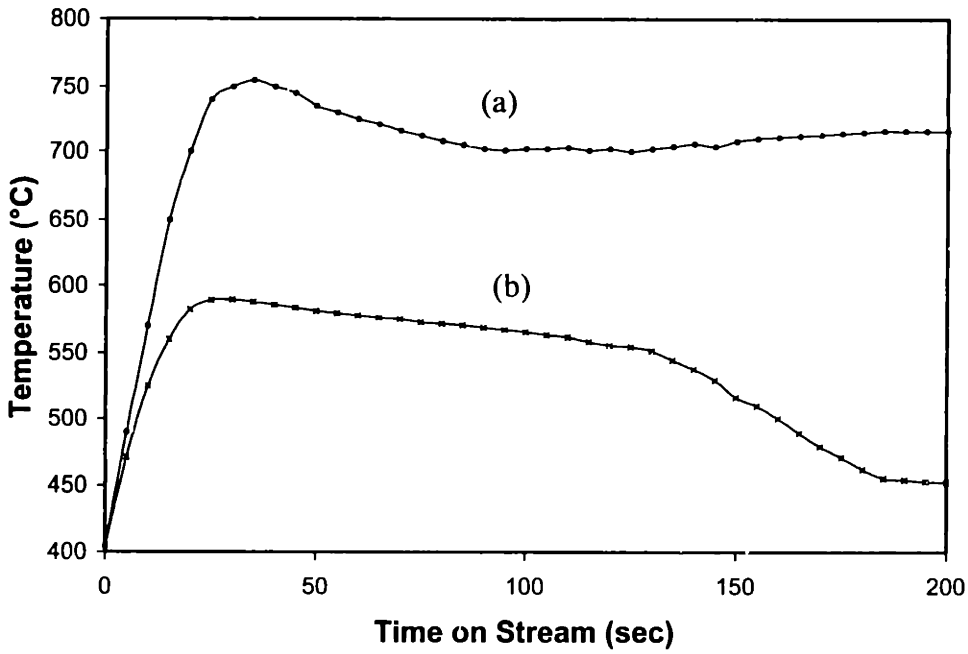

Figure 5.12. Deactivation of (a) PdO/CeO_2-BHA and (b) PdO/BHA, both supported on fiber-reinforced honeycombs (Pd loading = 1.2 wt% for both samples). Reactions were run at ϕ=0.3 with SPV=500,000 h^{-1}.

The increase in catalytic activity and resistance to deactivation exhibited by the PdO/CeO_2-BHA catalyst may be attributed to the ability of CeO_2 to spill over oxygen species to supported PdO clusters over a wide range of temperatures and oxygen partial pressures. This synergism between CeO_2 and PdO has been explored by previous researchers [36], who found that oxygen species could be transferred reversibly between PdO and CeO_2 under a variety of reaction conditions for the combustion of methane.

5.3.2 Catalyst Systems for Mid- and High-Temperature Combustion

Although the PdO-based materials exhibit activity for methane oxidation at remarkably low temperatures, their operation is limited to an outlet temperature of 700°C. It would be ideal to design a catalyst system capable of fully converting the stream exiting the ignition catalyst stage to generate a stable lean flame. This system should provide full conversion of methane by 700°C, and be able to withstand the elevated temperatures present in the flame front without deactivation. Most common designs for such a system involve two different catalysts: a mid-temperature range catalyst (500-900°C) (e.g. supported manganese or cobalt oxides), and a high-temperature flame

catalyst (900-1300°C) (e.g. monolith-supported BHA or silicon carbide) [4]. This section describes the thermal resistance and catalytic properties of the different supports and active materials under actual burner conditions.

5.3.2.1 Support Materials for High-Temperature Combustion

In addition to the active species, the catalyst supports for the mid- and high-temperature zones must be carefully chosen. Thermal shock resistance and low pressure drops are the most important selection criteria. The different supports described previously were tested for thermal shock resistance by rapid heating to 1300°C followed by cooling to ambient temperature. Heating was achieved by igniting a methane flame of ϕ=0.7 over the catalyst support surface. When the temperature on the support surface had reached 1300°C, the methane flow was cut off, and the support was rapidly cooled by a flowing stream of air. Pressure and torque were manually applied to the different support structures to evaluate their mechanical integrity after heat treatment.

The reticulated ceramics underwent significant degradation after just one or two heating-cooling cycles. Manual compression of the ceramic structures resulted in their collapse. We observed no significant difference in the thermal shock behavior of reticulated ceramics purchased commercially and those prepared in our laboratory from sol-gel derived ultrafine powders. The commercial reticulated yttria-stabilized zirconia appeared to be the most fragile, while the reticulated alumina prepared in our laboratory showed the best mechanical stability after heat treatment.

Nickel foams did not suffer from thermal shock deterioration even after repeated thermal cycling. However, significant oxidation of the nickel structure was observed after extended exposure to temperatures above 1000°C, which led to gradual degradation and weight loss. Fiber-reinforced honeycombs were found to retain mechanical integrity, without any appreciable loss of materials, after repeated thermal cycling. Based on these observations, fiber-reinforced honeycombs or nickel foams were selected as supports for mid-temperature catalysts, and fiber-reinforced honeycombs were used to support high-temperature systems.

5.3.2.2 Light-Off Behavior of Supported Metal Oxides

Activity and stability tests were conducted on MnO_2-BHA, CeO_2-BHA, MnO_2-CeO_2-BHA, and pure BHA. These active materials were introduced onto fiber-reinforced honeycombs and nickel foams through the procedures outlined previously (see Sections 5.2.3 and 5.2.4).

Light-off of a stream with ϕ=0.2 was observed at ~480°C and ~495°C for MnO_2-BHA (with 7.5 at% Mn) supported on nickel foams and fiber-reinforced honeycombs, respectively (see Table 5.2). The MnO_2-BHA loading on the different supports was ~20 wt% and the space velocity was 500,000 h^{-1}. MnO_2-BHA showed catalytic activity at a lower temperature of ~380°C under isothermal conditions in a packed bed reactor for a stream of 2 vol% CH_4 in air flowing at a space velocity of 60,000 h^{-1}. Kinetic analysis under differential conversion indicated that the reaction was first order with respect to methane concentration for $0.1 \leq \phi \leq 0.5$. At CH_4 concentrations > 5 vol% (corresponding to $\phi > 0.5$), the reaction became self-propagating due to the adiabatic temperature rise, eventually leading to flame ignition. Under such conditions, the assumption of differential conversion was no longer valid. Figure 5.13 shows a plot of the reaction rate for methane oxidation as a function of inlet methane concentration over MnO_2-BHA supported on a fiber-reinforced honeycomb.

For CeO_2-BHA coated on Ni foams and fiber-reinforced honeycombs, a stream with ϕ=0.2 was able to light off at ~500°C and ~505-510°C, respectively (Table 5.2). CeO_2-BHA first showed activity at ~400°C under isothermal conditions in a packed bed reactor at a space velocity of 60,000 h^{-1}. The reaction order with respect to methane over supported CeO_2-BHA was also found to be first order for $0.1 \leq \phi \leq 0.5$.

Table 5.2. Catalytic activity and stability of various mid- and high-temperature catalyst systems. Reactions were run at ϕ=0.2 with SPV=500,000 h^{-1}.

Catalyst System	Active Species Loading on Support	Light-off Temperature (°C)	Max. Operating Temperature (°C)
MnO_2-BHA on NF	1.5 at% Mn	480	1000
MnO_2-BHA on FRH	1.5 at% Mn	495	1000
CeO_2-BHA on NF	1.0 at% Ce	500	1100
CeO_2-BHA on FRH	1.0 at% Ce	510	1100
MnO_2-CeO_2-BHA on FRH	5.5 at% Mn + 2.5 at% Ce	440	1000
BHA on FRH	20 wt% BHA	560	> 1300

NF = Nickel foam
FRH = Fiber-reinforced honeycomb

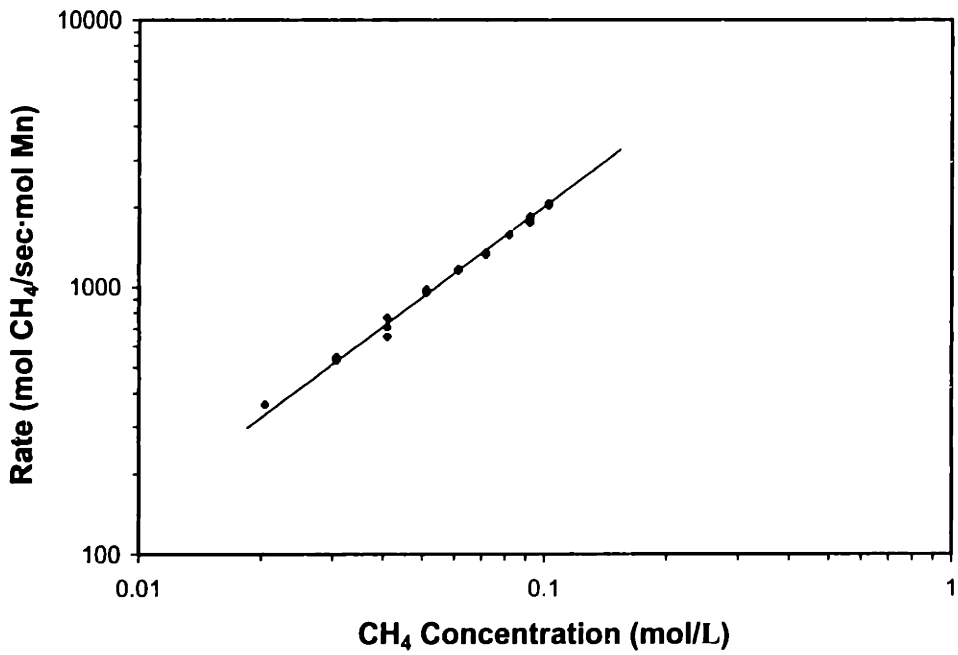

Figure 5.13. Reaction rate over MnO_2-BHA supported on a fiber-reinforced honeycomb as a function of inlet CH_4 concentration. Reactions were run at an inlet temperature of 460°C with SPV=500,000 h^{-1}.

A mixture of MnO_2 and CeO_2 was coated onto BHA to study the oxygen promotion effect of CeO_2 on MnO_2. The catalyst contained 5.5 at% Mn and 2.5 at% Ce. The introduction of CeO_2 dramatically improved the low-temperature catalytic activity of MnO_2. Light-off of MnO_2-CeO_2-BHA supported on a fiber-reinforced honeycomb was

observed at a low temperature of 440°C for ϕ=0.2 (Table 5.2). Kinetic studies could only be performed at $\phi \leq 0.36$, since higher methane concentration led to the ignition of a flame, even at a low inlet temperature of 440°C and a high space velocity of 2.5×10^6 h^{-1}. The reaction was first order with respect to methane at $0.1 \leq \phi \leq 0.36$. Figure 5.14 shows the conversion curves as a function of inlet temperature for this system operated under different ϕ values. CeO_2 might have enhanced oxygen transfer to the MnO_2 catalyst, as it did to the PdO system, to yield improved low-temperature activity and promote ultra-lean flames.

Monoliths and foams coated with pure BHA underwent light-off at ~560°C. BHA supported on a fiber-reinforced honeycomb could be operated at temperatures > 1300°C over extended periods.

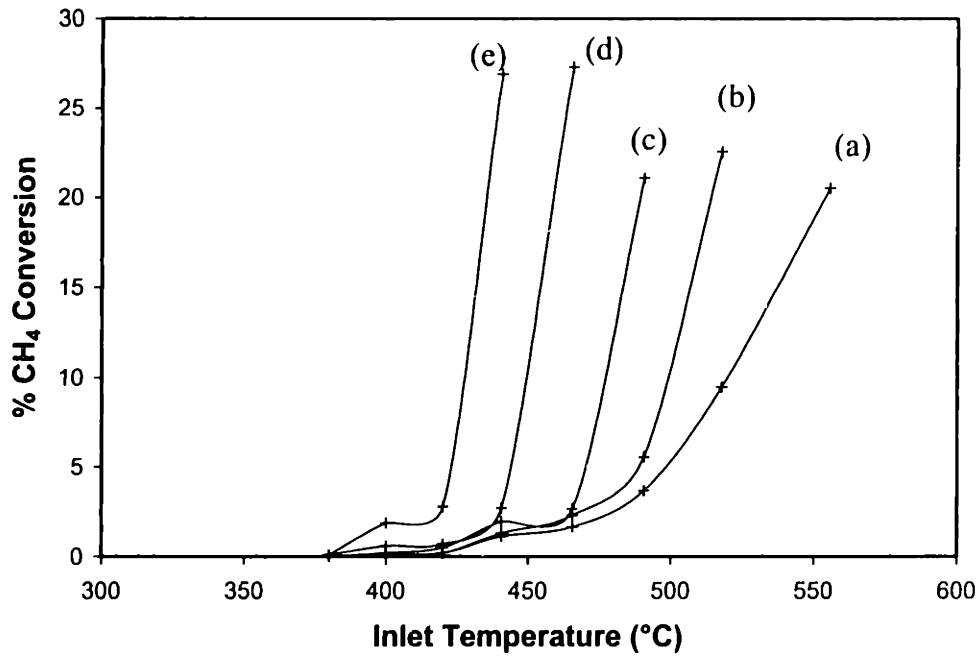

Figure 5.14. Methane conversion over MnO_2-CeO_2-BHA supported on a fiber-reinforced honeycomb as a function of inlet temperature for (a) ϕ=0.20, (b) ϕ=0.24. (c) ϕ=0.30, (d) ϕ=0.36, and (e) ϕ=0.40 with SPV=500,000 h^{-1}.

5.3.2.3 Activity and Stability of Supported Metal Oxide Catalysts under Flame Conditions

A catalytically stabilized flame will be ignited above the surface of a system when the rate of OH· emissions from the catalyst surface is higher than the rate of OH·

quenching from radicals propagation or termination steps in the gas phase [32]. The ignition of a homogeneous flame promotes radiative heat transfer from the flame front to the catalyst surface, which can increase the catalytic activity, but may also lead to catalyst sintering or vaporization. Most catalysts described in the previous sections will promote flame ignition when the catalyst surface reaches a temperature of 700-1000°C. The temperature of a typical catalytically stabilized lean flame ranges from 1000°C to 1500°C. The surface temperature of the flame-supporting catalyst under these conditions may vary between 900°C and 1400°C.

In our experimental procedure, a flame was ignited over different catalysts at various inlet temperatures by gradually increasing the air:fuel ratio. Once the flame was ignited, we investigated the catalyst deactivation by monitoring the surface and flame temperatures. After the flame has extinguished (either due to gradual deactivation over unstable catalysts or by manual shut-off of the methane flow over stable catalysts), the materials were allowed to cool down under flowing air. The mechanical stability of the support and the loss of the active phase were then evaluated. In general, ϕ~0.36 was required to promote a flame at low inlet temperatures ($\leq$ 550°C) over MnO_2-BHA and CeO_2-BHA. Promotion of a flame over pure BHA required the use of a low-temperature catalyst that could activate the reaction to heat up the BHA monolith to temperatures above 600°C. The measured flame temperatures under lean conditions and inlet temperatures of 450-600°C varied between 1000°C and 1500°C. Table 5.3 summarizes these results.

To promote a flame with ϕ=0.36 over MnO_2-BHA, an inlet temperature of ~550°C was required (Table 5.3). The flame temperature under this condition was measured at 1340°C, and corresponded to a theoretical adiabatic flame temperature of 1360°C. The surface temperature of the catalyst exceeded 1100°C within a few seconds after flame ignition. Under this condition, the MnO_2-BHA catalyst deactivated rapidly, and flame extinction would occur ~30 seconds after ignition. The activity of the catalyst could not be regained upon cooling and restarting. The deactivated catalyst showed significant decoloration from a deep brown color to a light pink color, suggesting a reduction in Mn oxidation state from +4 to +3. Additionally, there was a weight loss of

~5% in the catalyst-support system. We noted that a lower inlet temperature was required for flame promotion at a higher ϕ value (Table 5.3).

Table 5.3. Inlet temperature requirements for flame promotion, and flame temperature, catalyst surface temperature and deactivation time under flame conditions over different BHA-based catalysts supported on fiber-reinforced honeycombs. The reactions were run at various equivalent ratios (ϕ) and at SPV=500,000 h^{-1}.

Catalyst System	ϕ	Inlet Temperature* (°C)	Flame Temperature† (°C)	Surface Temperature‡ (°C)	Deactivation Time
MnO_2-BHA	0.36	550	1340	1150	< 30 sec
MnO_2-BHA	0.50	510	1650	1500	< 30 sec
CeO_2-BHA	0.36	570	1360	1100	> 1 h
CeO_2-BHA	0.50	530	1650	1500	< 120 sec
MnO_2-CeO_2-BHA	0.36	465	1200	1100	< 120 sec
MnO_2-CeO_2-BHA	0.40	440	1250	1150	< 30 sec
BHA	0.40	650	1350	1300	> 1 h

* Uncertainty in inlet temperatures: ±10°C
† Uncertainty in flame temperatures: ±100°C
‡ Uncertainty in catalyst surface temperatures: ±50°C

The thermal stability of CeO_2-BHA was considerably better than that of MnO_2-BHA. A flame was promoted over CeO_2-BHA at an inlet temperature of 570°C at ϕ=0.36 (Table 5.3). The measured flame temperature and calculated adiabatic flame temperature were 1360°C and 1380°C, respectively. The temperature of the catalyst surface rose to ~1100°C after a few minutes of exposure to the flame front. The catalyst remained stable under this condition and the flame was sustained for ~1 hour, after which the methane flow was purposely cut off. Analysis of the exhaust stream indicated no NO_x detected above the instrument's detection limit of ~1 ppm. There was no weight loss in the catalyst system after reaction. However, slight deactivation of the catalyst was observed after one heating cycle, possibly due to grain growth and loss of surface area. After its exposure to ~1100°C, the aged CeO_2-BHA catalyst underwent light-off at a higher temperature of 580-600°C, versus 570°C for a fresh catalyst. However, a stable flame could still be achieved and sustained over the aged CeO_2-BHA catalyst by

preheating the inlet stream of ϕ=0.36 to ~600°C. These characteristics made the CeO_2-BHA system an ideal catalyst for supporting lean flames.

The MnO_2-CeO_2-BHA catalyst showed the lowest inlet temperature requirements for promoting a stable lean flame. Figure 5.15 shows the ignition behavior of flames at $0.20 \leq \phi \leq 0.40$ as a function of inlet temperature. At a low inlet temperature of 440°C, a flame of ϕ=0.40 could be promoted over the catalyst (Table 5.3). Leaner flames of ϕ=0.36 and ϕ=0.30 could be achieved at inlet temperatures of 465°C and 490°C, respectively. Despite its superior low-temperature activity, the MnO_2-CeO_2-BHA system showed a deactivation behavior similar to MnO_2-BHA. The two systems underwent irreversible deactivation rapidly after exposure to temperatures above 900°C. However, the MnO_2-CeO_2-BHA catalyst could still be used for the mid-temperature stage to promote combustion after light-off over a PdO-based material, and to provide sufficient heat to activate the high-temperature stage.

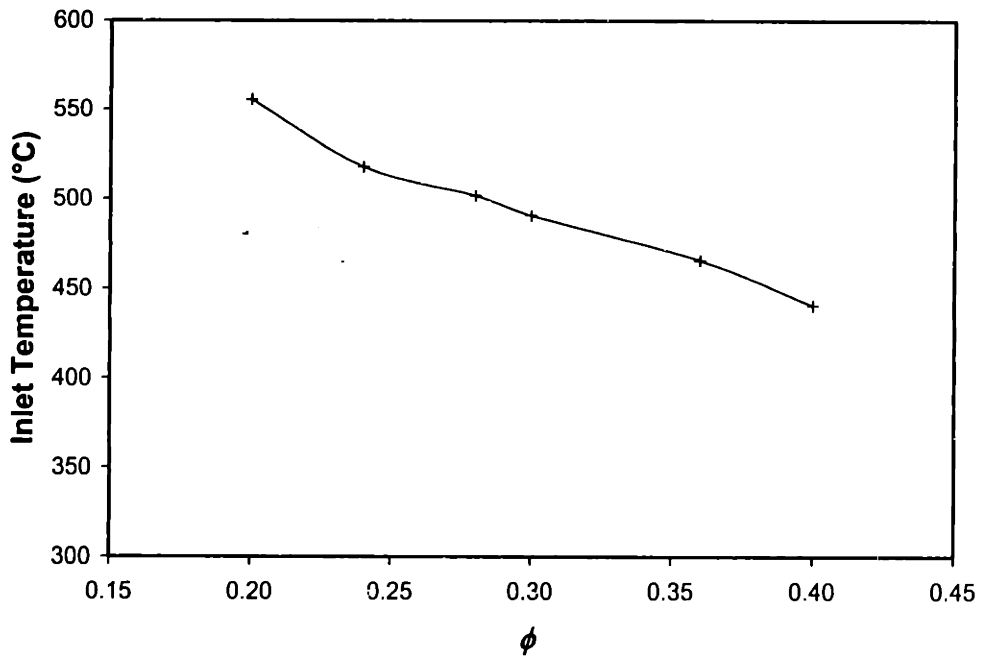

Figure 5.15. Inlet temperature required for flame ignition as a function of ϕ over MnO_2-CeO_2-BHA supported on a fiber-reinforced honeycomb. The reactions were run at SPV=500,000 h^{-1}.

For pure BHA coated on a fiber-reinforced honeycomb, an inlet temperature of 650°C was required to promote a flame at ϕ=0.40 (Table 5.3). The temperature at the

base of the flame was measured to be 1350°C, while the theoretical adiabatic flame temperature was calculated to be 1380°C. The surface temperature of BHA was stabilized at ~1300°C. The flame was shown to be stable for ~1 h, after which the methane flow was purposely shut off. The BHA-coated fiber-reinforced honeycomb showed no weight loss after reaction, and no cracking from thermal shock during the rapid cooling.

5.3.3 BHA-based Materials for CSTC Operations

As previously mentioned, a combination of ignition and flame-supporting catalysts would be required to achieve the stable promotion of a lean flame in a CSTC. Additionally, a mid-temperature catalyst could be used to increase the inlet temperature to the flame-supporting catalyst, and to reduce the outlet temperature requirements on the ignition catalyst. In this section, we propose two different systems that can be employed for stable catalytic combustion of lean fuel mixtures. The first system consisted of PdO/CeO_2-BHA supported on a fiber-reinforced honeycomb as the ignition catalyst, and a CeO_2-BHA-coated honeycomb as the flame-supporting catalyst. The second system included a PdO/CeO_2-BHA (with a low Pd loading) coated on nickel foam as the ignition catalyst, MnO_2-CeO_2-BHA coated on fiber-reinforced honeycomb as the mid-temperature catalyst, and a pure BHA-coated fiber-reinforced honeycomb as the flame-supporting catalyst.

5.3.3.1 Performance of the PdO/CeO_2-BHA + CeO_2-BHA System

This system was designed for operation under lean conditions, which would limit the temperature of the flame-supporting catalyst to ~1100°C. The ignition catalyst (7.5 g) consisted of 20 wt% Pd on CeO_2-BHA (3 at% Ce) washcoated (with a 17-wt% loading) on a fiber-reinforced honeycomb. The high-temperature catalyst (8.4 g) consisted of CeO_2-BHA (3 at% Ce) washcoated (with a 20-wt% loading) on a fiber-reinforced honeycomb.

A pre-mixed air-methane stream was flowed at 5.2 L/min through the catalyst stages at $0.2 \leq \phi \leq 0.5$ (see Table 5.4). A flame could be produced at an inlet temperature as low as 230°C for ϕ=0.5. Under this condition, the temperature past the low-temperature stage was stabilized at ~660°C, and the temperature at the surface of the CeO_2-BHA-

coated monolith was ~1200°C. The flame temperature was measured to be 1250°C, while the theoretical adiabatic flame temperature was calculated to be 1320°C. No NO_x was detected in the exhaust stream.

For a leaner fuel:air mixture of ϕ=0.38, the inlet temperature has to be increased to 340°C in order to obtain a flame. In this case, the temperature past the low-temperature stage was 685°C (see Table 5.4). The flame temperature was measured to be 1070°C, which corresponded to a theoretical adiabatic flame temperature of 1190°C. The flame under this condition could not be seen in an illuminated room and was barely visible to the naked eye in darkness. The NO_x level in the exhaust stream was well below the detection limit of the instrument.

After the temperatures of the different catalyst stages had stabilized, the air pre-heater was turned off to investigate the possibility of sustaining a flame with gases flowing into the first catalyst stage at ambient temperature. Within 10 minutes, the inlet temperature to the PdO/CeO_2-BHA stage dropped to ~35°C, while the flame supported on the CeO_2-BHA-coated monolith remained stable. For ϕ=0.38, the temperature after the first stage was maintained at 670°C, while the flame temperature was measured to be 985°C (see Table 5.4); the corresponding adiabatic flame temperature was calculated to be 1020°C. Operation was sustained for ~2 h with this set-up until the methane flow was purposely turned off. This catalyst system showed no deactivation or hysteresis in the heating-cooling-restarting cycles. Although it exhibited excellent light-off behavior and thermal stability, the corresponding flame temperature has to be limited to ~1200°C to prevent deactivation of the CeO_2-BHA flame-supporting stage. This relatively low flame temperature limit would have a negative effect on the overall efficiency of the turbine cycle.

Table 5.4. Flame stabilization profiles as a function of ϕ for the PdO/CeO_2-BHA/fiber-reinforced honeycomb + CeO_2-BHA/fiber-reinforced honeycomb system.[‡]

	ϕ=0.30	ϕ=0.38	ϕ=0.38*	ϕ=0.50
Pre-heater Duty (W)	750	650	0	530
Inlet Temperature (°C)	385	340	35	230
Ignition Catalyst Temperature (°C)	603	685	670	660
Flame-Supporting Catalyst Temperature (°C)	1130	1000	950	1200
Flame Temperature (°C)	1160	1070	985	1250

*Catalyst was pre-treated at ~300°C
[‡]Reactions were run at SPV=500,000 h^{-1}

5.3.3.2 Performance of the PdO/CeO_2-BHA + MnO_2-CeO_2-BHA + BHA System

The purpose of this system was to (i) minimize the palladium loading on the first stage by introducing a highly active mid-temperature catalyst stage, and (ii) to allow for flame operation at higher temperatures by introducing a flame-supporting catalyst with thermal stability superior to oxide-coated BHA. In this system, PdO/CeO_2-BHA (with 6 wt% Pd) was coated onto a nickel foam (17 wt% washcoat) for the ignition stage. The total weight of the stage was 4.2 g, with an overall Pd loading of 1 wt%. MnO_2-CeO_2-BHA was employed as the mid-temperature stage. This stage (8.2 g) comprised of a fiber-reinforced honeycomb coated with ~19 wt% of a BHA powder containing 5.5 at% Mn and 2.5 at% Ce. A pure BHA-coated fiber-reinforced honeycomb was used as the flame-supporting stage. The total weight of this stage was 5.9 g and the BHA loading was ~22 wt%. The pre-mixed gases were flowed at 5.0 L/min over the three-stage catalyst system.

Light-off over the low-temperature stage was observed at ~300°C, and a flame could be obtained over the BHA-coated honeycomb at ϕ=0.39 (see Table 5.5). The temperature above the first stage was stabilized at ~600°C, corresponding to a CH_4 conversion of ~25%. The temperatures above the MnO_2-CeO_2-BHA stage and the BHA-coated honeycomb were 790°C and 1190°C, respectively. The flame temperature was measured to be ~1230°C, while the corresponding adiabatic flame temperature was calculated to be ~1300°C. The flame was stable over a period of ~1 h before the methane flow was purposely turned off.

In order to increase the measured flame temperature beyond 1300°C, the methane concentration was increased to ϕ=0.50. A stable flame was obtained at an inlet temperature as low as 285°C. The temperatures above the first, second and third stages were 650°C, 800°C and ~1300°C, respectively. The flame temperature was measured to be 1345°C, and the corresponding adiabatic flame temperature was calculated to be 1400°C. The flame was stable under these conditions for > 2 h before the methane flow was purposely turned off. The catalyst system did not undergo deactivation, and no hysteresis was noted during heating-cooling-restarting cycles.

Table 5.5. Flame stabilization profiles as a function of ϕ for the PdO/CeO_2-BHA/nickel foam + MnO_2-CeO_2-BHA/fiber-reinforced honeycomb + BHA/fiber-reinforced honeycomb system.[‡]

Temperature (°C)	ϕ=0.36	ϕ=0.39	ϕ=0.50
Inlet	325	300	285
Ignition Catalyst	585	600	650
Mid-Temperature Catalyst	750	790	800
Flame-Supporting Catalyst	1050	1190	1300
Flame	1165	1230	1345

[‡]Reactions were run at SPV=500,000 h^{-1}

5.4 Summary

Various active BHA-based materials supported on different monoliths have been examined for methane oxidation in a catalytically stabilized thermal combustor operating under industrial conditions. PdO/BHA was found to be the most active material for low-temperature oxidation, achieving light-off at a temperature as low as 200°C. PdO clusters deposited on BHA via vapor grafting and impregnation techniques demonstrated similar characteristics under the reaction conditions. PdO was found to deactivate significantly by 700°C due to reduction to metallic Pd, even at low methane concentrations. Introduction of CeO_2 onto BHA was found to promote oxygen transfer to PdO clusters, preventing PdO deactivation during CH_4 combustion.

Among the non-noble metal catalysts, MnO_2-BHA-based materials were found to be the most active for low-temperature oxidation, achieving light-off at ~400°C. CeO_2 was also found to promote the activity of these materials. Deactivation at elevated temperatures (> 1000°C) was an issue for Mn-containing systems.

The performance of different monolithic supports was evaluated. Reticulated structures were found to promote better fuel-air mixing and to reduce mass transfer resistance at low temperatures. However, pressure drop at elevated temperatures became prohibitively high for these systems. Reticulated ceramics were found to have good compatibility with BHA-based active washcoats, but suffered from cracking due to thermal shock after exposure to flame temperatures. Stable coatings could be applied onto metallic foams using electrophoretic deposition; the nickel foams showed better thermal shock resistance than reticulated ceramics, but gave rise to greater pressure drop. Stable coatings of BHA-based materials could also be deposited onto fiber-reinforced honeycombs; these monoliths with straight channels had excellent thermal shock resistance and negligible pressure drop, and were therefore preferred as catalyst support for high-temperature operations.

Finally, flame promotion and stability were investigated over a variety of catalyst systems. We found that a combination of low-temperature noble metal-based catalyst and high-temperature metal oxide-based catalysts was effective at stabilizing lean flames over a wide range of equivalent ratios and flame temperatures. A combination of PdO/CeO_2-BHA supported on a fiber-reinforced honeycomb as ignition catalyst and CeO_2-BHA on a fiber-reinforced honeycomb as flame-supporting catalyst was found to enable light-off at temperatures as low as 230°C. This catalyst combination could be used to stabilize lean flames at temperatures of 985-1250°C with $0.30 \leq \phi \leq 0.50$. A system consisting of PdO/CeO_2-BHA (with a low Pd loading) supported on nickel foam as ignition catalyst, MnO_2-CeO_2-BHA supported on fiber-reinforced honeycomb as mid-temperature catalyst and pure BHA supported on fiber-reinforced honeycomb as flame-supporting catalyst was investigated for operation at higher flame temperatures. This system would enable light-off at 285-325°C for $0.36 \leq \phi \leq 0.50$. Stable operation could be achieved with flame temperatures of 1165-1345°C.

5.5 References

[1] W. C. Pfefferle, *J. Energ.* **3**, 142 (1978).

[2] J. A. Barnard, J. N. Bradley, "Flame and Combustion." 2nd ed. Chapman and Hall, New York, 1985.

[3] J. H. Lunsford, *Langmuir* **5**, 12 (1989).

[4] L. M. Quick, S. Kamitomai, *Catal. Today* **26**, 303 (1995).

[5] H. Sadamori, T. Tanioka, T. Matsuhisa, *Catal. Today* **26**, 337 (1995).

[6] F. Cunill, L. v. d. Beld, K. R. Westerterp, *Ind. Eng. Chem. Res.* **36**, 4198 (1997).

[7] S. M. Correa, *Comb. and Flame* **102**, 205 (1995).

[8] U. Nieken, G. Kolios, G. Eigenberger, *Chem. Eng. Sci.* **49**, 5437 (1994).

[9] A. J. Zarur, H. H. Hwu, J. Y. Ying, *Langmuir,* in press.

[10] A. J. Zarur, J. Y. Ying, *Nature*, in press.

[11] A. J. Zarur, N. Z. Mehenti, A. T. Heibel, J. Y. Ying, submitted to *Langmuir.*

[12] C. P. Mehnert, J. Y. Ying, *Chem. Comm.,* 2215 (1997).

[13] C. P. Mehnert, D. W. Weaver, J. Y. Ying, *J. Am. Chem. Soc.* **120**, 12289 (1998).

[14] A. J. Zarur, H. H. Hwu, J. Y. Ying, submitted to *J. Catal.*

[15] J. R. Howell, M. J. Hall, J. L. Ellzey, *Progr. Energ. Comb. Sci.* **22**, 121 (1996).

[16] W. M. Carty, P. W. Lednor, *Curr. Opin. Solid State Mater. Sci.* **1**, 88 (1996).

[17] M. V. Twigg, J. T. Richardson, *Prep. Catal. VI* **91**, 345 (1995).

[18] K. Jiratova, L. Morakova, J. Malecha, B. Koutsky, *Coll. Czech. Chem. Comm.* **60**, 473 (1994).

[19] K. Jiratova, L. Morakova, J. Malecha, B. Koutsky, *Coll. Czech. Chem. Comm.* **62**, 875 (1997).

[20] G. D. Forsythe, U.S. Patent No. 5,079,064. E. I. Du Pont de Nemours and Company, 1992.

[21] Y. Kagawa, N. Kurosawa, T. Kishi, *J. Mater. Sci.* **23**, 735 (1993).

[22] R. D. Rawlings, *Composites* **25**, 372 (1994).

[23] H. Y. Wang, R. N. Singh, R. A. Lowden, *J. Am. Ceram. Soc.* **79**, 1783 (1996).

[24] P. Sarkar, P. S. Nicholson, *J. Am. Ceram. Soc.* **79**, 1987 (1996).

[25] A. B. Anderson, K. C. Stein, J. J. Feenan, L. E. J. Hofer, *Ind. Eng. Chem.* **53**, 809 (1961).

[26] C. F. Cullis, B. M. Willatt, *J. Catal.* **83**, 267 (1983).

[27] N. Takahashi, M. Sato, M. Nagumo, A. Mijin, *Zeolites* **6**, 420 (1986).

[28] T. R. Baldwin, R. Burch, *Appl. Catal.* **66**, 359 (1990).

[29] R. J. Farrauto, M. C. Hobson, T. Kennelly, E. M. Waterman, *Appl. Catal. A: Gen.* **81**, 227 (1992).

[30] J. E. Turner, M. B. Maple, *Surf. Sci.* **147**, 647 (1984).

[31] H. Lieske, J. Volter, *J. Phys. Chem.* **89**, 1841 (1985).

[32] L. D. Pfefferle, W. C. Pfefferle, *Catal. Rev.-Sci. Eng.* **29**, 219 (1987).

[33] X. Y. Wang, G. Z. Lu, S. L. Wu, *J. Rare Earths* **13**, 99 (1995).

[34] A. Trovarelly, *Catal. Rev.-Sci. Eng.* **38**, 439 (1996).

[35] J. R. Gonzalez-Velasco, J. Entrena, J. A. Gonzalez-Marcos, J. I. Gutierrez-Ortiz, M. A. Gutierrez-Ortiz, *Appl. Catal. B: Env.* **3**, 191 (1994).

[36] M. Haneda, T. Mizushima, N. Kakuta, *J. Phys. Chem. B* **102**, 6579 (1998).

[37] J. Y. Ying, A. Tschöpe, *Chem. Eng. J.* **64**, 225 (1996).

[38] K. Otsuka, T. Ushiyama, I. Yamanaka, *Chem. Lett.* **9**, 1517 (1993).

[39] K. Otsuka, Y. Wang, E. Sunada, I. Yamanaka, *J. Catal.* **175**, 152 (1998).

[40] Q. G. Yan, W. Chu, L. Z. Gao, Z. L. Yu, S. Y. Yuan, *Natural Gas Conv. V* **119**, 855 (1998).

Chapter 6. Recommendations for Future Work

In this thesis, the applicability of nanostructured complex oxides for catalytic combustion was studied. A reverse microemulsion-mediated sol-gel processing was employed to obtain non-agglomerated particles with sizes in the nanometer range, exceptional chemical homogeneity and thermal resistance, and well-controlled surface chemistry. These materials have been evaluated for low-temperature methane oxidation and high-temperature catalytic combustion. Further testing of these materials for long-term thermal and hydrothermal stability would be useful to ascertain their applicability in industrial gas turbine systems.

The reverse microemulsion-mediated synthesis may prove useful in the processing of various inorganic and organic materials. Other complex oxides, including aluminates and perovskites, may benefit from the enhanced chemical homogeneity and microstructure control achievable through this method. Organic materials, including dyes, fertilizers and drug carriers, may be synthesized with a controlled particle size in the nanometer range and specific surface chemistry for advanced applications.

Chapter 7. Conclusions

In this thesis, nanostructured complex oxides were examined for application in high-temperature catalytic combustion of methane. Barium hexaaluminate (BHA) was chosen for its crystalline structure, which allows grain growth suppression at elevated temperatures and provides a support for the dispersion of various active materials.

A reverse microemulsion-mediated synthesis technique was developed to achieve BHA materials with enhanced chemical homogeneity, so that crystallization to the desired phase could occur at lower temperatures. This minimized grain growth and allowed the materials to preserve ultrahigh surface areas (>100 m^2/g) after calcination at 1300°C.

The reverse microemulsion systems were stabilized by non-ionic surfactants. They were characterized by small-angle neutron scattering (SANS) and quasi-elastic light scattering (QELS) for phase structure and morphology as a function of water content. The reverse microemulsions were found to be stable under conditions observed during sol-gel processing; they were successfully used to synthesize BHA nanoparticles with excellent combustion activity and stability.

The nanoparticulate BHA materials were further modified through the introduction of metal oxide surface deposits and structural dopants to increase their catalytic activity for methane combustion. The reverse microemulsion provided a unique medium to achieve ultrahigh dispersion of the active components. Noble metals were also introduced onto BHA nanoparticles using vapor grafting and impregnation techniques.

The modified BHA materials were coated onto ceramic and metallic monoliths and tested in a catalytically stabilized thermal combustor operating under industrial conditions. The modified BHA-based catalysts achieved light-off at temperatures as low as 230°C, and sustained activity at flame temperatures in excess of 1300°C. The NO_x levels in the exhaust streams were found to be well below the instrumental detection limit (~1 ppm).